Observations of Feedback Between Protostars and Their Natal Clouds

by

Joel D. Green

Submitted in Partial Fulfillment
of the Requirements for the Degree

Doctor of Philosophy

Supervised by
Professor Dan M. Watson

Department of Physics and Astronomy
Arts, Sciences, and Engineering
School of Arts and Sciences

University of Rochester
Rochester, New York

2009

Curriculum Vitae

The author was born in New York on May 2, 1978, to Mark and Leah Green. He attended Cornell University from 1996 to 2000, and graduated with a Bachelor of Arts in Astrophysics in 2000, working as a Java/C programmer for the FORCAST camera on SOFIA, under Professor Terry Herter.

He came to the University of Rochester in the Fall of 2000 and began graduate studies in astrophysics. Upon successful completion of the preliminary examination in 2002, he was awarded a Master of Arts in Astrophysics, and began writing IDL-based data analysis software that would become part of the core of the *Spitzer* Space Telescope reduction package. He began research in the field of space-based infrared astronomy under the direction of Professor Dan Watson in 2002.

In 2005 he passed the Qualifying Examination and began to study FU Orionis variables with *Spitzer*. In 2007 he began to study, with Professor David Neufeld of Johns Hopkins University, the momentum injection rates of Herbig Haro flows in molecular clouds, which provides the core of this disseration.

PUBLICATIONS

Refereed journals

- "Spitzer mapping of molecular hydrogen pure rotational lines in NGC 1333: A detailed study of feedback in star formation," 2009arXiv0904.0603M Maret, S., et al. 2009, arXiv:0904.0603

- "Spitzer Infrared Spectrograph Observations of Class I/II Objects in Taurus: Composition and Thermal History of the Circumstellar Ices," 2009ApJ...694..459Z Zasowski, G., Kemper, F., Watson, D. M., Furlan, E., Bohac, C. J., Hull, C., & Green, J. D. 2009, ApJ, 694, 459

- "Crystalline Silicates and Dust Processing in the Protoplanetary Disks of the Taurus Young Cluster," 2009ApJS..180...84W Watson, D. M., et al. 2009, ApJS, 180, 84

- "Silica in Protoplanetary Disks," 2009ApJ...690.1193S Sargent, B. A., et al. 2009, ApJ, 690, 1193

- "Dust Processing and Grain Growth in Protoplanetary Disks in the Taurus-Auriga Star-Forming Region," 2008arXiv0811.3622S Sargent, B. A., et al. 2008,ArXiv e-prints, 0811.3622

- "Spitzer Space Telescope Infrared Spectrograph mapping of the central kpc of Centaurus A," Quillen, A. C., et al. 2008, MNRAS,384, 1469

- "Spitzer IRS Spectra and Envelope Models of Class I Protostars in Taurus," Furlan, E., et al. 2008,ApJS,176,184

- "The development of a protoplanetary disk from its natal envelope," 2007Natur.448.1026W Watson, D. M., et al. 2007, Nature, 448, 1026

- "HD 98800: A 10 Myr Old Transition Disk," Furlan, E., et al. 2007, ApJ, 664, 1176

- "Spitzer Observations of HH 54 and HH 7-11: Mapping the H2 Ortho-to-Para Ratio in Shocked Molecular Gas," Neufeld, D. A., et al. 2006, ApJ, 649, 816

- "Spitzer IRS Observations of FU Orionis Objects," **Green, J. D.**, Hartmann, L., Calvet, N., Watson, D. M., Ibrahimov, M., Furlan, E., Sargent, B., & Forrest, W. J. 2006, ApJ, 648, 1099

- "A Survey and Analysis of Spitzer Infrared Spectrograph Spectra of T Tauri Stars in Taurus," Furlan, E., et al. 2006, ApJS, 165, 568

- "Spitzer Observations of Hydrogen Deuteride," Neufeld, D. A., et al. 2006, ApJL, 647, L33

- "Dust Processing in Disks around T Tauri Stars," Sargent, B., et al. 2006, ApJ, 645, 395

- "Polycyclic Aromatic Hydrocarbons Orbiting HD 233517, an Evolved Oxygen-rich Red Giant," Jura, M., et al. 2006, ApJL, 637, L45

- "Mid-Infrared Spectra of Polycyclic Aromatic Hydrocarbon Emission in Herbig Ae/Be stars," Sloan, G. C., et al. 2005, ApJ, 632, 956

- "Disks in Transition in the Taurus Population: Spitzer IRS Spectra of GM Aurigae and DM Tauri," Calvet, N., et al. 2005, ApJL, 630, L185

- "The Accretion Disk of the Lithium-depleted Young Binary St 34," Hartmann, L., et al. 2005, ApJL, 628, L147

- "Colors of Classical T Tauri Stars in Taurus Derived from Spitzer Infrared Spectrograph Spectra: Indication of Dust Settling," Furlan, E., et al. 2005, ApJL, 628, L65

- "Spitzer IRS Spectra of Young Stars Near the Hydrogen-burning Mass Limit," Furlan, E., et al. 2005, ApJL, 621, L129

- "The Truncated Disk of CoKu Tau/4," D'Alessio, P., et al. 2005, ApJ, 621, 461

- "The SMART Data Analysis Package for the Infrared Spectrograph on the Spitzer Space Telescope," Higdon, S. J. U., et al. 2004, PASP, 116, 975

- "Mid-Infrared Spectra of Dust Debris around Main-Sequence Stars," Jura, M., et al. 2004, ApJS, 154, 453

- "Mid-infrared Spectroscopy of Disks around Classical T Tauri Stars," Forrest, W. J., et al. 2004, ApJS, 154, 443

- "The State of Protoplanetary Material 10 Million years after Stellar Formation: Circumstellar Disks in the TW Hydrae Association," Uchida, K. I., et al. 2004, ApJS, 154, 439

- "Mid-infrared Spectra of Class I Protostars in Taurus," Watson, D. M., et al. 2004, ApJS, 154, 391

Acknowledgments

It has been a long and fulfilling road culminating in this work, and I could not have reached this point without considerable assistance. My thanks go out particularly to my extremely patient and supportive Ph D. advisor Dan Watson, who has guided my growth into a mature academic and scientist, challenging me on all subjects, willing to discuss any topic from astrophysics to the Yankees to the Byzantine Empire. In addition I want to thank David Neufeld, Ted Bergin, Sebastien Maret, Neal Evans, John Bally, Alice Quillen, Alex Hubbard, Eric Blackman, Bill Forrest, Ben Sargent, Kyoung Hee Kim, Melissa McClure, Judy Pipher, Alice Quillen, Paule Sonnentrucker, Eric Mamajek, Manoj Puravankara, Adam Frank, Nicholas Raines, Jenny Greene, Rachel Dudik, Rob Gutermuth, Terry Herter, Randi Worhatch, and Gordon Orris for their generous help on or relating to this project. I would be nowhere without the wonderful staff and computer expertise of the Physics and Astronomy department, including Rich Sarkis, Dave Munson, Barb Warren, Dollie Aiken, Nikki Hatler, Steffin Spears, Sondra Anderson, Janet Fogg, and Shirl Brignall. I would be remiss if I did not thank Mike Thomas for teaching me the basics of good labwork in the summers of 2000 and 2001.

In addition I would like to thank my parents; without their unwavering support I would not have gained the self-confidence I have today; my brother Adam, whose critical eye kept me on track and inspired me; my grandparents, cousin Jeff Fenster, and "cousin" Al Cohen who kept me motivated. I must also include my Rochester family, Oscar, Helen, Cheryl, and Marty Karch, who took me in as a long-lost grandson at every holiday. My friends and support network in Rochester has been rich beyond my wildest dreams and I have forged connections here that will last a lifetime. I would like to thank David Harman for allowing me to shrug

off my world cares in orchestra every week, and Sarah Creel for introducing me both to great music and great friends. I would like thank Aaron Schweinsberg for providing me with a home in my waning months in Rochester, and both Alex Hubbard and Aaron Schweinsberg for 12 years of steadfast friendship since I was a freshman at Cornell. I would like to thank the members of Maxwell's Demons, the Uncivil Engineers, the Quantum Fielders, and Freud's Mom for many wonderful summers of softball. I would like to thank the members of Aeolia Physica, in particular Bob Knox, for including me in their woodwind quintet. I owe a debt of gratitude to Kyle MacLea for his consistent steady advice and encouragement, and to Edwin and Katherine Anderson for keeping me grounded. I also would briefly acknowledge by nickname all those who helped me with my work, and my monthly barbecuing resolution:

Neil Reserve, The New Neil, Wall-E-World, Katamari Carbary, The Blonde, Unlisted, Snow Mexican, Cookie Monster, Restorer of Worlds, SoCo SubLime, Pete At The Green, The Moose Wrangler, Lasermonkey, GenLab Alpha, Optical Delusion, The Dog Walkerer, The Peerage, The Great Lakes Viking, The East Coaster, The Whalewatcher, The Pianist, Frat Girl, Mikey's Cleaning Service, Southern Breakfast, The Midwesterner, Petey's Towing Service, One Chip Amy, Team of Rivals, Femtolasermonkey, The Physicist, Pizza Snob, Mad Barber of East Ave, Dying Duck, Classified, Unlimited Pong, The New Ashley, Bermuda Research Triangle, Mikey's Other Cleaning Service, The Desk Master, The New Me, Schoolmistress, and The Graduate Rag.

Abstract

In this thesis we explore the relationship between the formation of protostars, and the influence of protostellar outflows on their environment using Infrared Spectrograph onboard the Spitzer Space Telescope. First we introduce the modern understanding of protostellar development advanced by the IRS_Disks guaranteed time program. Next we explore the FU Orionis phenomenon, an IRS_Disks dataset of flaring stars undergoing a burst accretion event. Finally we present a suite of data on Herbig Haro flows in Cepheus A to determine whether protostellar outflows can dissociate a wide angle cavity in their natal cloud.

We present 5-35 μm spectra, taken with the Infrared Spectrograph (IRS) on the Spitzer Space Telescope, of five FU Orionis objects: FU Ori, V1515 Cyg, V1057 Cyg, BBW 76, and V346 Nor. All but V346 Nor reveal amorphous silicate grains in emission at 10 μm and 20 μm, and show water-vapor absorption bands at 5.8 and 6.8 μm and SiO or possibly methane absorption at 8 μm. These absorption features closely match these bands in model stellar photospheres — signs of the gaseous photospheres of the inner regions of these objects' accretion disks. The continuum emission at 5-8 μm is also consistent with such disks, and, for FU Orionis and BBW 76, longer-wavelength emission may be fit by a model which includes moderate disk flaring. V1057 Cyg and V1515 Cyg have much more emission at longer wavelengths than the others, perhaps evidence of substantial remnant of their natal, infalling envelopes. This indicates that FU Orionis events can briefly raise outflow rates sufficiently high to dispel their surrounding envelopes and open swaths of the ambient medium via compression waves.

Herbig Haro objects are small emission nebulae that signify the interaction between both broad and collimated outflows from young stellar objects and the

ambient molecular cloud material. GGD37 is suspected to be an amalgamation of at least two superposed flows (including HH 168) traveling in different directions on the sky. Weaker shocks (less than $\sim$ 10000 K) excite the molecular hydrogen into various rotational states detectable at IRS wavelengths, while strong shocks completely destroy the molecules and illuminate the ions. The Infrared Spectrograph on board *Spitzer* has enabled us to gather spatial information on a number of higher excitation species, and place greater constraints on the flows, allowing us to separate them chemically. How does the instability of driving sources of Herbig Haro jets affect their surrounding medium? By studying the pre-and post-shock gas, we can determine whether outflows from young stars have greater clumping or dispersive effects on their environment. Do outflows trigger or suppress star formation in the neighborhood? We present evidence that powerful flows such as HH 168 can unbind a protostar in its early stages of development, opening a $\sim$ 10000 AU cavity of ionized material. And finally, new observations from the IRS open the question: precisely where is the protostar that is driving HH 168? We provide evidence that the source of the HH 168 flow is at the radio source W2, rather than the more distant HW3c.

Table of Contents

List of Tables

List of Figures

LIST OF FIGURES xiii

1   Introduction

1.1   Understanding of the Development of Protostars from Natal Clouds at the Turn of the Millenium

The field of astronomy evokes our sense of wonder; it contextualizes our place in the universe. This is its greatest contribution both to science and society. First we learned how to describe the motions of the Earth about the sun, and then our interaction with the other planetary bodies that have formed alongside us in our solar system. The next step was to characterize the place of our solar system amongst the billions in the Milky Way. Now that we have essentially completed the census of our own solar system, a curious person will ask: how typical is our neighborhood? Are all stellar systems organized like our own? Is the inner region dominated by smaller rocky planets with few moons, surrounded by a remnant asteroid debris belt, then the much larger hydrogen-gas giants with great miniature planetary systems amongst their rings, ice giant planets, and finally, cometary material? Were the planets always in the same place as they are now? Do stars change during their lifetimes? Are stellar systems formed in isolation, or in connected groups? Are they formed at the same time by a single cataclysmic event, or by gradual processes?

It has only become possible in the last decade or so to examine extra-solar planets ("exoplanets") directly. The list of exoplanets is expanding rapidly –according to the Extrasolar Planets Catalog [1] there are currently 344 confirmed detections as

---

[1]http://exoplanet.eu/catalog.php

of April 16, 2009. Although exoplanet detection provides considerable insight, it is an extremely incomplete sample, afflicted by heavy selection bias– only planets with notably large mass, large orbital eccentricity, small orbit, large brightness, or those with fortunate inclinations to our line-of-sight can be detected, and only in nearby stellar systems. Although we now know that stellar systems can develop quite differently from our own, it is difficult to draw statistical conclusions about typical planetary systems.

The difficulty of detecting planets results from their extremely low brightness to surface area ratio. The light emitted from planets is overwhelmed by the surrounding star. It is much easier to detect material around a star before planets have formed, when the dust and gas are still surrounding the young star. Understanding the origins of the typical stellar system leads to a better understanding of the final product. Furthermore we have observations of meteorites, comets, and asteroids in our own solar system that we attribute to the earliest periods of its development, and it is much simpler to observe similiar objects in protostellar systems than it is to detect exoplanets around such objects.

The luminosity of a star is related to the surface temperature, if it radiates approximately as a blackbody:

$$L_{star} = 4\pi R_{star}^2 \sigma T_{eff}^4 \tag{1.1}$$

where T_{eff} is the effective temperature of the star at its surface R_{star} and σ is the Stefan-Boltzmann constant (5.67×10^{-8} W m$^{-2}/K^{-4}$).

The discovery that most stars lie along a single line in the Hertzsprung-Russell (H-R) diagram (Russell, 1913) began a revolution in stellar classification. These main sequence stars represented the vast majority of stellar lifespans, but optical spectra of stars in dark clouds such as the nearby Taurus cloud (Joy, 1945, 1949; Herbig, 1952) revealed objects several magnitudes brighter than their color-temperatures would indicate. Additionally these objects exhibited high ultraviolet (UV) emission (Varsavsky, 1960; Smak, 1964, and many others) and strong Hα and Hβ line (Rydgren et al., 1976). The key idea linking these observations was the self-similar isothermal spherical collapse model (Larson, 1969, 1972; Shu, 1977; Terebey et al., 1984; Adams & Shu, 1986; Adams et al., 1987, 1988), which was most easily applied to comparatively isolated, sparser, and nearby ($\sim$ 140 pc)

Taurus-Auriga region. Cohen & Kuhi (1979) characterized a large sample of stars from the Taurus molecular cloud and linked considerable excess emission in the infrared (IR) to the early development process of a star via the inside-out collapse model, showing that a young star will first appear – out of its optically extinguishing veil – above the main sequence and drift down along Hayashi tracks (that is, to settle on the main sequence by contracting while maintaining its surface temperature). The excess UV/IR emission was thereby linked to the process of star formation.

Kenyon & Hartmann (1987) showed how the UV/IR excess could be explained in many cases with the presence of a geometrically thin, circumstellar disk of dust and gas (to explain the IR emission) accreting onto the central star (to explain the UV emission). The disk height above the midplane was given by hydrostatic equilibrium, although in some cases the disk model required an outward flaring in order to account for the colder (longer wavelength) infrared excess. The accretion rate can be calculated from the H_α emission and is generally found to be $\sim 10^{-7}$ $M_\odot \, yr^{-1}$ or less although in a small fraction of Taurus objects it ranged up to 10^{-6} $M_\odot \, yr^{-1}$, particularly among those dominated by far-IR excess (at wavelengths greater than $\sim 10 \; \mu$m) (Kenyon & Hartmann, 1995, and numerous references therein). The Taurus cloud was observed extensively from the ground and the findings were compiled in Kenyon & Hartmann (1995), and parallel studies were performed for other nearby star forming regions.

Thus by the end of the 20th century, the standard picture of star formation was established. The nearby molecular cloud complexes are active regions of star formation; they are churned up clouds of molecular hydrogen, helium, "metals" (heavier elements produced mostly as bi-products of multiple past epochs of star death and core collapse, dispersing their components into the interstellar medium) and dust particles, traced by jets and outflows from young stars or dying stars. If some small part of that cloud is compressed, it may begin an inside-out collapse. The majority of the affected material quickly ($\sim 10,000$ yr) collapses to form a protostar – although the star formation process is quite inefficient in terms of converting the mass of the molecular cloud into gas, utilizing only about 1-10% (e.g. Rownd & Young, 1999, and references therein) – surrounded by an envelope of colder gas; the surrounding material is also mixed and pulled in. If the infalling dust particles – in the form of unprocessed silicate (SiO_x) mixtures

such as pyroxenes ($[Mg/Fe]SiO_3$) or olivines ($[Mg/Fe]SiO_4$) commonly found in the interstellar medium (ISM) – have any intrinsic spin along a particular axis, they will rotate even more quickly as they fall, conserving angular momentum and orbiting the star in a plane around it, forming a relatively flat disk that is increasingly flared at larger radii from the star. [2]

If the protostellar mass is insufficient to trigger hydrogen burning, the result is a brown dwarf star. The formation of brown dwarfs was generally thought to occur in one of two ways: first, the initial mass supplied to the protostar is insufficient to produce a main sequence object, or second, the brown dwarf is a protostar with a truncated development that was ejected from a multiple system before it could accrete enough mass to trigger hydrogen burning (e.g. McDonald & Clarke, 1993, and discussions therein). In the second case it would be difficult to imagine a brown dwarf maintaining its circumstellar disk, which would be stripped away due to tidal effects. But do substellar objects follow a similar development pattern to their higher-mass young stellar object counterparts? Disks were detected even around high-mass brown dwarfs (Comeron et al., 1998; Comerón et al., 2000; Luhman, 1999) with the Infrared Astonomical Satellite (IRAS) and the Infrared Space Observatory (ISO) as well as from the ground, but in general these systems were faint and difficult to categorize.

A simple classification scheme coalesced, describing young stellar objects with infrared excess emission (Adams et al., 1987), based primarily on the strength of the excess and the slope of the continuum emission. This was connected to an evolutionary sequence which I describe briefly here (although it was also proposed that the initial density and composition could also play a role). Note that this classification scheme applies only to low mass stars (those less than 2 $M_\odot$, as discussed in Ch. 2 and 3). High mass protostars (discussed in Ch. 4) have a much messier development, as they proceed through these stages with much greater speed than the (relatively) calm low mass star [3]. At best this scheme may work as a general guide to high mass stars; the details of disk and evolution may

---

[2]It is important to note that the Hα equivalent width is an indicator not simply of accretion onto the central protostar, but the presence of an inner disk that is required for the accretion to take place; a disk with a minimum radius far from the central star would not show evidence of accretion.

[3]In particular, hydrogen burning may ignite in the core of the protostar before the gravitational collapse of the circumstellar envelope is complete.

differ greatly.

The youngest protostars, referred to as Class 0 (although intitially grouped along with Class I sources) are undetected at wavelengths shorter than 20 μm, predominantly emitting at far-IR and sub-mm wavelengths. Thus it is extremely difficult to observe anything contained within the veiling molecular cloud in such systems – the central protostar and any circumstellar disk in such systems will not contribute significantly to the flux even in infrared, which is dominated by the cold gas and dust continuum.

After sufficient accretion and envelope depletion the system becomes detectable at shorter wavelengths, and is referred to as Class I; much of the mass is in the protostar and a considerable amount is in the circumstellar disk, but the depleted envelope remains optically thick and veils the system. Many of the youngest sources exhibit signs of bipolar outflow. These outflow emission lines appear less frequently as infrared luminosity decreases, but appear to be a standard presence among young protostars, which is most likely a direct result of higher accretion rates, as a means of removing angular momentum from the protostar, which would otherwise spin furiously as a result of accretion. This indicates that molecular clouds are likely threaded with jet and shock-like structures that will stir up the medium. As we will see in Chapter 4, outflows – particularly those from higher mass protostars – significantly affect the density, temperature, and composition of the cloud; protostars are responsible for a considerable amount of recycling.

Eventually the envelope clears from around the star and the disk dust grains collide and stick together in spots to form larger grains and crystalline structures, slowly building into planetessimals. After the envelope is gone, the central protostar has neared its final mass, and the disk remains optically thick, the system is referred to as Class II. There are several subclasses– flat spectrum sources, in which the spectral energy distribution (SED) is flat (ie. the power radiated is relatively constant as a function of wavelength) are notably different than the typical Class II source, for which power typically decreases as a function of wavelength, albeit remaining well in excess of the stellar photospheric emission.

Finally, when the disk has dissipated sufficiently to become optically thin and the molecular gas has dispersed (whether by accretion onto the central star or by planet formation), leaving only dust grains, the star is referred to as Class

III. Class III sources and the older debris disk systems represent the endstate of protostellar development– until the central star ignites hydrogen burning in the core and enters the main sequence. During this final extended phase the infrared excess disappears completely from wavelengths short of $\sim 15~\mu$m and frequently is undetected even at longer wavelengths. The lifetime of such systems is constrained by a combination of two factors: either particle-particle collisions are the primary grain destruction mechanism, or if the collisional rate is too low – as measured by very small mid-IR ($\geq 30~\mu$m) fluxes when compared to the luminosity of the central star, now unobscured by surrounding material at shorter wavelengths – then the particles eventually spiral in via Poynting-Robertson drag.

1.2   Difficulties in Observing YSOs

We have seen that a number of questions remained unanswered by the observations available at the turn of the millenium. Is the Adams et al. (1987) classification scheme a good picture of the lifetime of a young star? What fraction of stars fall into each classification in nearby star forming regions? What are the differences amongst nearby regions, and are they indicative of cluster age, or of different conditions within the clusters? Are Class 0 sources simply Class I sources that formed in denser regions, or do they represent an earlier phase of stellar development? What is the disk fraction around Class II sources, and can we find evidence of planet formation? What is the relative contribution of disks and envelopes to the infrared flux of young stars? Can we better characterize the visual extinction in molecular clouds? What are disks and circumstellar envelopes composed of, and how do they differ from the interstellar medium? Is there evidence of disk accretion shocks? Do young stars accrete material in sudden cascades of material? How is this connected to bipolar outflows? If the classification/development idea is essentially correct, is the transition from one class to another gradual?

It is apparent that if planet formation plays a large role in the dispersion of these disks and the transition between Class II/III or possibly Class I/II, then infrared spectroscopy provides a unique method for inferring the existence of planets. If the circumstellar dust grains emit approximately as blackbodies (B_ν), then in the mid-infrared we are sensitive to grains heated to temperatures of under

100 K to a few hundred K; given either direct heating by the central star (in the case of an optically thin disk) or indirect heating via starlight re-radiated from the disk surface down to the disk midplane, we would expect a radial temperature dependence. Therefore the continuum slope would be a direct indicator of the mass density as a function of radius in the circumstellar disk. If planet formation causes central clearings, then we would detect gaps or holes in the disk (in a manner similar to the gaps in the rings of Saturn). Unlike most planet detection methods, this technique would be *more* sensitive to planets at larger radii from the central star, as the gap or hole created might be larger.

We have seen that young stars are embedded in giant molecular clouds, composed primarily of hydrogen and helium gas and silicate dust. This material is much colder than the protostar itself, which would dominate the emission at optical wavelengths; the cloud material emits strongly at infrared (IR) and sub-millimeter (sub-mm) wavelengths. Moreover since the protostar is at early stages deeply embedded, it suffers from considerable extinction– the material absorbs most of the starlight and re-emits at longer wavelengths. Thus optical telescopes are unable to penetrate the veil surrounding the star, and longer wavelength telescopes can probe the scattered starlight and the dust and gas emission much more easily.

Observations utilizing only ground-based telescopes are greatly hampered by the atmospheric water absorption bands throughout the IR – although there are several transmission windows in which the absorption is manageable, the sensitivity of an equivalently-sized telescope outside of the atmosphere is several orders of magnitude better. In 1946, Lyman Spitzer, Jr. proposed that a space-based IR observatory would avoid these problems. IRAS surveyed the sky in 1983 at mid and far-IR wavelengths and showed that many young stars have infrared excesses, but due to large beam sizes (low spatial resolution) it was still difficult to disentangle the excess of the system itself from the background cirrus emission. ISO provided IR imaging and spectroscopy during the mid-1990s and formed the basis for many of the programs that utilized the *Spitzer Space Telescope* (Werner et al., 2004).

1.3   The Spitzer Space Telescope

The Spitzer Space Telescope, originally proposed as the Space Infrared Telescope Facility (SIRTF), was launched to great fanfare on August 25, 2003, at 1:35 AM. The operational goal was a 2.5 year mission. Although the launch fell during the solar minimum, and thereby in theory avoiding large coronal mass ejection events, the telescope was immediately bombarded during the in-orbit checkout and science verification phase with the fourth largest coronal mass ejection event ever recorded, followed shortly thereafter by the *largest* single coronal mass ejection event. After three months, the telescope had already received bombardment expected after the mission lifetime had ended.

It was an inauspicious beginning to one of the most successful NASA missions. The mission lifetime will reach roughly six years before the last of the liquid helium that cools the infrared detector arrays to 4.2 K boils off into the solar system– the internal temperature will rise to 30 K, leaving the two shortest wavelength bands of the IRAC camera still operable– and the legacy of Spitzer will live on in the Warm Mission for several years to come. Amazingly, despite being bombarded by much greater amounts of solar radiation than expected, and despite five years of decay in space, *the detectors of Spitzer are still more sensitive than the projections from lab measurements made before launch.* The wealth of science that has resulted from this feat of engineering will form the core of research projects for years to come. There is currently no planned replacement for the Spitzer Space Telescope at its longest observed wavelengths (30-42 μm); the archival research value of *Spitzer* is great.

Spitzer has provided astronomers with unprecedented sensitivity at infrared wavelengths, allowing us the tools to understand the star and planet formation process. *Spitzer* has a payload of three instruments particularly well suited to the study of protostellar systems in the mid-infrared – the Infrared Array Camera (IRAC) (Fazio et al., 2004) with imaging bands at 3.6, 4.5, 5.8, and 8.0 μm; the Multiband Imaging Photometer for Spitzer (MIPS) (Rieke et al., 2004) with bands at 24, 70, and 160 μm as well as spectroscopic capabilities at low resolution from 50-100 μm; and the Infrared Spectrograph (IRS) (Houck et al., 2004) with spectroscopic capabilities from 5.3-42 μm. *Spitzer* has a f/12 primary mirror 85 cm in diameter. The blind pointing accuracy of *Spitzer* is an impressive 0.36

arcseconds (radial rms), and it is frequently no longer necessary to use the peak-up cameras to guarantee that point source targets land in the nominal nod positions (the pair of positions on the slit where staring mode observations are centered by default).

The IRS includes four separate 128x128 arrays, referred to as modules: Short-Low (SL; 5.2-14 μm, λ / $\Delta\lambda \sim 90$), Long-Low (LL; 15-40 μm, λ / $\Delta\lambda \sim 90$), Short-High (SH; 10-20 μm, λ / $\Delta\lambda \sim 600$) and Long-High (LH; 20-40 μm, λ / $\Delta\lambda \sim 600$); additionally it has peakup imaging cameras at 15 and 20 μm. The modules use advanced blocked impurity band (BIB) detector arrays, optimized for medium resolution spectroscopy and imaging; in Ch. 4 we explore another method of creating images that utilizes the underlying spatial information contained within the spectrograph data, rather than the camera.

Spitzer projects take advantage of this sensitivity in two ways: they select objects obscured from the ground by atmospheric absorption, and they complete broad sampling of brighter objects in manageable timeframes. Both these types of programs have helped to reduce selection bias and provide us with a picture of a more "typical" stellar system in its earliest stages. The IRS is particularly well-suited to understanding the details of protostellar and protoplanetary systems. Although it is possible to get reasonable ground-based imaging in the established atmospheric transmission bands and thereby fit simple models to determine continuum levels, it is impossible to determine precisely what species are contributing flux to the mix. Spectrographs provide very specific details about the chemical composition of these systems; it becomes possible to characterize young stars based on their components, but this analysis is not possible if most of the wavelengths are inaccessible with ground-based telescopes.

In this thesis we consider first the broad sweep of the evolution of protostellar and protoplanetary systems. Then in order to track the effect of star formation on its natal cloud, we consider first what happens during an accretion cascading event, and then we track the particles as they are ejected back into the medium via jet launching, producing beautiful compression shockwave trails across the cloud, stirring up the medium and altering it in ways that may affect the structure and future development of the cloud thousands of years later.

1.4   A Spitzer-IRS Survey of FU Orionis Objects

The FU Orionis variables are pre-main sequence systems which initially were identified as having large ($\sim$ 5 mag), sudden outbursts which typically decay in decades (e.g., Herbig, 1977). FU Ori outbursts have been modeled as resulting from rapidly accreting disks in Keplerian rotation around pre-main sequence stars, a model which explains their broad infrared Spectral Energy Distributions (SEDs) and the variation of spectral type and rotational velocity with the wavelength of observation (Hartmann & Kenyon, 1996). FU Ori disks are thought to differ from those of most Classical T Tauri stars (CTTS) in that the heating of the disk is dominated by local accretion energy release (viscous dissipation), at least in the inner disk regions, while CTTS disks, although accreting, are thought to be heated mostly by radiation from the central star (e.g., Kenyon & Hartmann, 1987). Extended images show that FU Ori are typically surrounded by remnants of the original molecular cloud material out of which the system formed, still falling onto the disk (Herbig, 1977; Goodrich, 1987).

On the human time scale, FU Ori outbursts are rare events; there have only been $\sim$ 5-10 outbursts detected in the past seventy years. Compared to the local rate of star formation – $\sim$ 0.02 yr^{-1} within 1 kpc of the Sun (Miller & Scalo, 1979) – they happen frequently enough that it is plausible to suggest that stars commonly experience such events. Young stars may experience them repeatedly, early in their development (Herbig, 1977; Hartmann & Kenyon, 1996). If so, they may play a fundamental role in early stellar protoplanetary-disk evolution: the total mass accreted in these short-lived events represents a significant fraction (10% or more) of the final mass of the developing young star.

Mid-infrared spectra from the Infrared Spectrograph (IRS; Houck et al., 2004) on board the Spitzer Space Telescope (Werner et al., 2004) provide crucial constraints on the structure of the inner few hundred AU of FU Ori systems. These spectra may permit isolation of the contributions of the cold envelopes and disks heated by viscous dissipation.

1.5 The Most Complete Observational Diagnostics of Shocks So Far

The cascade that signals star formation is generally thought to begin with an initial clumping or density fluctuation of material within the cloud material. There are several suggested mechanisms to trigger clumping of material; most originate from the conditions surrounding massive stars. Photoionization of the region surrounding massive stars directly causes the formation of HII regions. The powerful winds and inertial forces generated by the massive stars can also directly affect their environment. In addition, when massive stars collapse into neutron stars, the supernova remnant shock sweeps through the galaxy and can cause star formation in spherical shells at great distances from the supernova.

Herbig Haro objects are small emission nebulae that signify the interaction between both broad outflows and collimated jets ejected from young stellar objects and the ambient molecular cloud material, an indication of a rolling compression wave of material. Outflows from YSOs, while not as energetic as supernovae or photoionization, are far more common and may play a significant role in stirring up the molecular cloud material, possibly disrupting or altering other protostellar cores. In particular we focus on a region with a powerful outflow that provides a wealth of information about the interaction of shock and the previously unperturbed medium.

GGD37 (Gyulbudaghian et al., 1978) is suspected to be an amalgamation of at least two superposed flows (including HH 168) traveling in different directions on the sky. Weaker shocks (less than ~ 10000 K) excite the molecular hydrogen into various rotational states detectable at IRS wavelengths, while strong shocks completely destroy the molecules and illuminate the ions. The Infrared Spectrograph on board *Spitzer* has enabled us to gather spatial information on a number of higher excitation species, and place greater constraints on the flows, allowing us to separate them chemically. How does the instability of driving sources of Herbig Haro jets affect their surrounding medium? By studying the pre-and post-shock gas, we can determine whether outflows from young stars have greater clumping or dispersive effects on their environment. Do outflows trigger or suppress star formation in the neighborhood? And finally, new observations from the IRS open

the question: precisely where is the protostar that is driving HH 168?

1.6   Thesis Organization

This thesis is structured as follows. Since my work is included in a large collection of papers produced by the IRS_Disks team and collaborators, in Chapter 2 we provide a comprehensive introduction to the IRS_Disks *Spitzer* survey of YSOs and protostars. In Chapter 3 we discuss the dynamics and properties of the FU Orionis phenomenon, a special cataclysmic early phase of star formation. In Chapter 4 we analyze the effects that young stars have on their surrounding environment through Spitzer-IRS maps of the GGD 37 outflow complex. In the final Chapter we summarize the results presented and suggest directions for future research.

2   How Does the IRS_Disks Program Contribute to Our Understanding of Protoplanetary Systems?

As we will see in later chapters, the process of star and planet formation does not occur in isolation; it is the interaction between the young protostar and its environment that enable the entire process, especially in the tumultuous early years of the star's lifetime. As stars mature and reach the main sequence, they become much more independent of their parent cloud, until giving back some of their accumulated material in their final violent stages of collapse. As such it is important to learn as much as possible both about parent cloud and the protostellar environment, tracking the path of particles from the molecular cloud through the circumstellar envelope in a cascade onto the circumstellar disk, and finally its ejection in the form of bipolar jets and outflows launched from the star or the disk, back into the cloud, sending rippling effects ringing through the nearby regions in the form of shocks.

In this chapter we will focus on the development of protostellar systems and planets from their natal clouds tracked primarily by the evolution of their mid-infrared spectral energy distribution, considering the implications of these observations for the traditionally understood stages of stellar development. The IRS_Disks project for the first half of *Spitzer* operations (December 2003- May 2006) encompasses ~ 170 hours of observations of young systems in nearby molecular cloud complexes, primarily Taurus-Auriga, Ophiucus, and Chamaeleon. We have motivated our studies of YSOs in the infrared in Chapter 1. In this chapter I

will describe the IRS_Disks survey, and provide details of the sample selection and data reduction process. Then I will highlight the important features that appear in IRS wavelengths; these are the diagnostics that we look for in our sample.

2.1 The Dataset

After post-processing, the IRS_Disks team (including the IRS_Disks program as well as the IRS_Amazing8 program of *nine* of the more famous debris disks) produced SL-LL or SL-SH-LH spectra for ~ 2400 protostars within 500 parsecs, the closest regions of active star formation. We selected targets to cover all classes of protostellar development as understood prior to the launch of *Spitzer*. Using data from ground-based infrared observations (such as 2MASS JHK), as well as ISO and IRAS, most of the low mass protostars had been sorted into classes. Class III protostars show little evidence of excess emission in the mid-infrared, and are dominated at near-IR and optical wavelengths by the emission from the photosphere of the central source, which is approximated as a blackbody at the effective temperature of star, or with more sophisticated colors from Kenyon & Hartmann (1995). Class II protostars appear photospheric (ie. exhibit no detectable excess emission above that predicted by a stellar photospheric model without additional material) at shorter wavelengths but show excess emission in the near or mid-IR. Class I protostars are dominated by colder material in the optical and IR, and the stellar photosphere is not a significant contributor to the flux. Class 0 protostars show no significant emission at short wavelengths and appear only in the mid-IR and longer wavelengths. Both Class I and Class 0 sources are frequently marked by bipolar outflows of material and exhibit heavily extinguished SEDs.

The IRS_Disks program includes YSO candidates in nearby star-forming regions and young clusters, in large enough numbers to achieve a high degree of statistical significance in any uncovered trends. We covered ~ 10 objects in each octave of luminosity ranging from M-stars (including stars below the hydrogen burning limit of 0.08 $M_\odot$) all the way to F-stars of 2 $M_\odot$. We selected potential YSO targets during the first 2.5 years of the mission based on their brightness and color: red, but not too red (to avoid galaxies), and blue, but not too blue (to avoid late-type stars that contain no remnant material) (Furlan, 2006). In the

second half of the mission we were able to utilize our collaborations with IRAC teams and select targets based on their IRAC colors that approximated the shorter wavelength SEDs of YSOs, supplemented with MIPS detections at 24 μm (e.g. Megeath et al., 2004).

2.2 Introduction to Spitzer-IRS and Data Reduction

The Infrared Spectrograph (Houck et al., 2004) onboard the Spitzer Space Telescope (Werner et al., 2004) collects data using its arsenic doped silicon blocked-impurity-band (Si:As BIB) detectors (at short wavelengths), and antimony-doped silicon (Si:Sb BIB) at long wavelengths. The data is collected at the Spitzer Science Center (SSC) and run through a pipeline that corrects the data for numerous artifacts including stray cross-dispersion light, cosmic ray impacts, and flat-fielding and produces a basic calibrated data product. We further process the data using IDL routines developed at Cornell and Rochester – the Spectral Analysis, Mapping, and Reduction Tool (SMART) data reduction package (Higdon et al., 2004) supplemented with additional routines – identifying unreliable pixels from previous campaigns and cleaning them using the imclean/imnan routines, interpolating from nearest neighbors.

There are several ways in which a pixel will "go bad." The pixel can become permanently illuminated or permanently dark, which is simple to catch from a single observation. More difficult is dealing with pixels that are functioning incorrectly – that is, pixels that have both high and variable dark current – which we refer to as rogue pixels. Rogue pixels have an illumination-dependet responsivity; the conversion factor from incident photons to detector electrons is dependent on the number of incident photons, which is very dangerous and much more difficult to diagnose. The number of bad pixels increases over time (although it decreases as the detector bias is turned up, trading off the longest wavelength data for reduced rogue pixel count – see Figure 2.1); this final step has become increasingly important to avoid mis-identifying rogue pixels as spectral lines. In particular we maintain a list of all pixels that exhibit 4σ errors in more than one IRS campaign dark referred to as the grand roguemask.
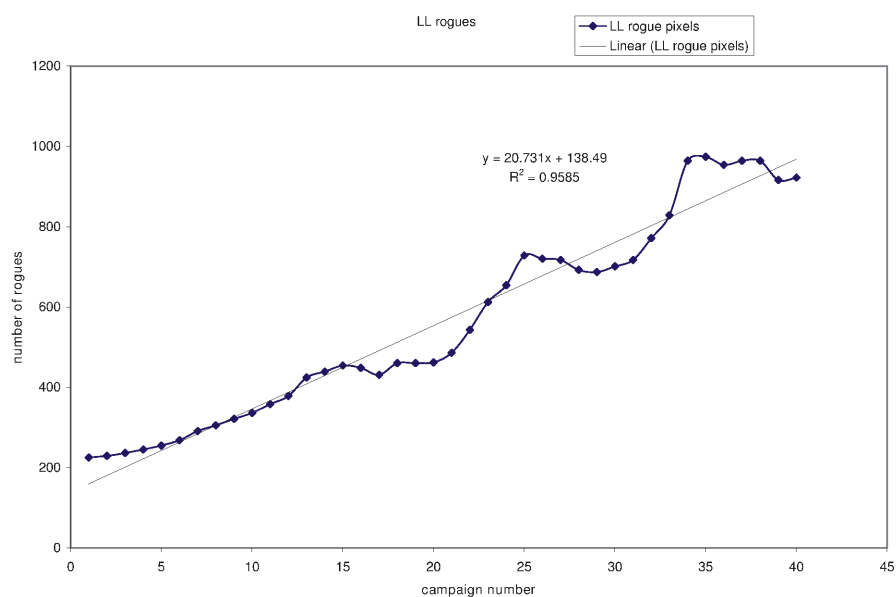
Figure 2.1 The number of rogue pixels as a function of campaign, for LL. The rogue pixels grow predictably from campaign to campaign; however the cause of these bad pixels is unknown, as this phenomenon did not occur in laboratory testing. Note that this plot only includes observations through March 2006.

An even better technique than cleaning bad pixels using nearby interpolated good pixels is replacing them with good data from another portion of the slit; this is possible in mapping observations as long as the positions are overlaid with sufficient density. The problem with interpolation is apparent when examining narrow features such as spectral lines; if a bad pixel is noted at the peak intensity, the flux will be systematically underestimated by using the nearby (off-peak) pixels to interpolate a now artificially flattened profile.

Unfortunately, there are limitations and caveats to pixel replacement as well. The edge pixels are particularly problematic if one hopes to use the spatial information in a mapping observation; thus it is wise to overlap observations so that, at a minimum, the edge pixel positions are covered by more central pixels from other mapping positions, ie. a horizontal step of no more than 60% of the slit length for the high resolution modules, which are five pixels across. In this way, pixel 1 is duplicated by pixel 4 from another map position. Ideally it is best to cover every position in the map twice (ie. a horizontal step of no more than half a slit length). With accurate pointing reconstruction, it is then possible to substitute good data from another map position for bad data, and produce a more reliable datacube. We have developed routines to apply these corrections to large maps, based on a 2-D image fixing routine (badpixfix.pro) written by Ben Sargent; his thesis contains a full description of the image fixing routine.

It should be noted that all data prior to pipeline version S12 suffered from poor flatfielding, and as such the flatfielded ("bcd") datatype was unreliable. For older data, including all of the FU Ori spectra presented in Chapter 3, we began with the non-flatfielded ("droop") data product from the Spitzer Science Center IRS calibration pipeline version S11.0.2, consisting of 2-D spectral-spatial, non-flatfielded images. The known wavelength calibration error in S11 was corrected before extraction, and the uncertainties from nod-differences were substantially reduced. For newer data, the basic calibrated data (BCD) were processed using version S12.0 (prior to mid-2005), S15.3, or S17.2 of the processing pipeline.

2.2.1   Point-Source Observations within IRS_Disks

Observations usually consisted of a SL-LL pairing or SL-SH-LH pairing in order to cover all wavelengths with minimal overlap in wavelength, with the minimum

integration times. The protostars were carefully selected from catalogues such as
Kenyon & Hartmann (1995) for the Taurus-Auriga complex and similar surveys
for Ophiucus and Chamaeleon as well as a few smaller regions, examining stars
with mid-infrared fluxes that fell between ~ 3 mJy to 100 Jy at 10 μm, in or-
der to achieve a minimum signal-to-noise of 3, up to ~ 50 – above which other
sources of uncertainty dominate the data. Sources below ~ 1 L$_\odot$ were observed in
SL-LL mode. Uncertainties were computed primarily by comparing independent
observations of the same point source at each of the nominal nod positions[1]:

$$F_{unc}(\lambda) = |\frac{F_{nod1}(\lambda) - F_{nod2}(\lambda)}{2}| \tag{2.1}$$

The resulting uncertainties are generally ~ 10 below the pipeline-provided un-
certainties, which are calculated from a derived error plane; the source of this dis-
crepancy is unclear and may indicate problems with uncertainty propagation. In
cases where we have repeated consecutive observations of the same target (multi-
ple "DCEs") we observe uncertainties similar to those derived from nod-differences
(with the exception of the artificial tail to zero uncertainty in the nod differences).
We always utilize nod difference uncertainty values whenever possible. The photo-
metric accuracy within a given module is $\sim 2\%$, although the variations in the size
of the various apertures can cause mismatches between modules that can exceed
10%.

In all cases, similarly-prepared spectra of the same pipeline version were pro-
duced from observations of two photometric standard stars, α Lac (A1 V) for
the short wavelengths ($\lesssim 14$ μm) and ξ Dra (K2 III) for longer wavelengths. We
then divided each target spectrum, nod position by nod position, by the spec-
trum of the one of the standard stars and multiplied by the standard's template
spectrum (Cohen et al., 2003). The final spectra are then averages of the nod
positions. In IRS SL and LL observations both orders are always observed, but
the point-source target is placed sequentially in each order, so the "off" orders
provide sky-background measurements which we subtracted from the on-target
spectra. We then extracted point-source spectra for each nod position using a

---

[1]Nod positions are standard slit positions with the source placed at $\sim 1/3$ and 2/3 of the slit
length. In a staring mode observation, a spectrum is taken with the point source centered at
nod position 1 and then at nod position 2 in rapid succession, which assists in data calibration
and the removal of many artifacts.

column of variable width scaled to that of the instrumental point-spread function. For our IRS SH and LH observations we simply extracted the full slit, and did not subtract sky background emission, which is negligibly faint compared to the targets at these wavelengths.

Most of the observations were performed in staring mode, with the source placed at each of the two nominal nod positions, which are located at approximately one-third and two-thirds of the distance along the slit. A minority of the observations were run in mapping mode, using a 3 x 2 raster of slit positions – two across in the spatial direction, three across in the spectral direction, spaced by half the slit length and width, respectively. Spectra were computed using the two central map positions, although it is also possible to compute the flux by fitting Gaussian profiles in both directions along the map and computing the centroid and scaling the flux appropriately. Sky frames were only available for low resolution observations, using either a portion of the sky in the opposite nod observation, or in the opposite order observation. As the low resolution modules are paired, there are twice as many independent observations available to use to calculate sky and uncertainty. Additionally, only the low resolution apertures are long enough to deconvolve sky from the target.

Theoretically the raster maps were a more efficient use of time than the staring mode observations, which initially included a time-intensive high-accuracy pointing peak-up using the onboard Pointing Calibration and Reference Sensor (PCRS). However after a the first cycle of science observations the blind pointing accuracy of *Spitzer* was rated at an impressive 0.36 arcseconds (radial rms), and it is frequently no longer necessary to use the peak-up cameras to guarantee that the point source target lands in the nominal nod positions – thus most of our later observations consisted of clusters of staring mode observations with a single initial peak-up.

After post-processing has been completed, there are still several corrections that can be made that can significantly affect both the flux and SED shape. First is a calculated adjustment for telescope mis-pointing, described in Sargent et al. (2006); a wavelength dependent correction was calculated and applied to the spectra if the source is substantially off from the nominal nod position. Second is extinction correction, using the interstellar extinction curve from Mathis (1990) or Draine & Lee (1984). When correcting for extinction, we find that the adjustment

to the continuum flux is sufficient, but the 10 μm silicate feature adjustment is only applicable up to an A_V of $\sim$ 12 (Flaherty et al., 2007). For more extinguished objects we used a new law based on the work of Chiar et al. (2007); McClure (2008).

2.2.2 Mapping Observations of Extended Sources

In Chapter 4 we present a mapping grid of observations taken with Spitzer-IRS, covering a large extended outflow region, allowing us to produce spatial maps of all features within the IRS wavelengths. Calibrating extended source maps is more complicated than point-source extractions.

GGD37 (Cep A West) was observed in a Spitzer-IRS map grid consisting of two adjacent rectangles, on two separate occasions; first in SH and LH in 2004, and again in SL and in deeper exposures in LH in 2007 (see Table 4.1). These maps cover approximately the same regions of the sky, although Cep A East was observed concurrently with the first set of observations of GGD 37. The resolution of individual pixels of the IRS is given in the Spitzer Observers' Manual [2] as ranging from $\sim$ 2 - 5 arcsec squares, depending upon the module in question; therefore the maps contain differing spatial resolution, although they have all been regridded and oversampled for display purposes. There are sub-pixel resolution features reproduced independently in different maps, suggesting that we may be resolving individual features even less than 5 arcseconds in extent. Additionally many of the individual features correlate strongly with features in higher resolution ground-based imaging at near-IR wavelengths. Despite this, any features that are smaller than a single resolution element should be treated cautiously.

The basic calibrated data (BCD) were processed at the Spitzer Science Center (SSC) using version S12.0, S15.3, or S17.2 of the processing pipeline, and then reduced using SMART, modified by additional routines that we have developed to deal with map grids (as opposed to single observation staring mode). We process the data beyond the traditional SMART reduction (as we did with point sources) by removing bad pixels in all modules, using a "grand" rogue mask created from a superposition of the bad pixel masks of each separate observing campaign. Rogues

---

[2]http://ssc.spitzer.caltech.edu/documents/som/
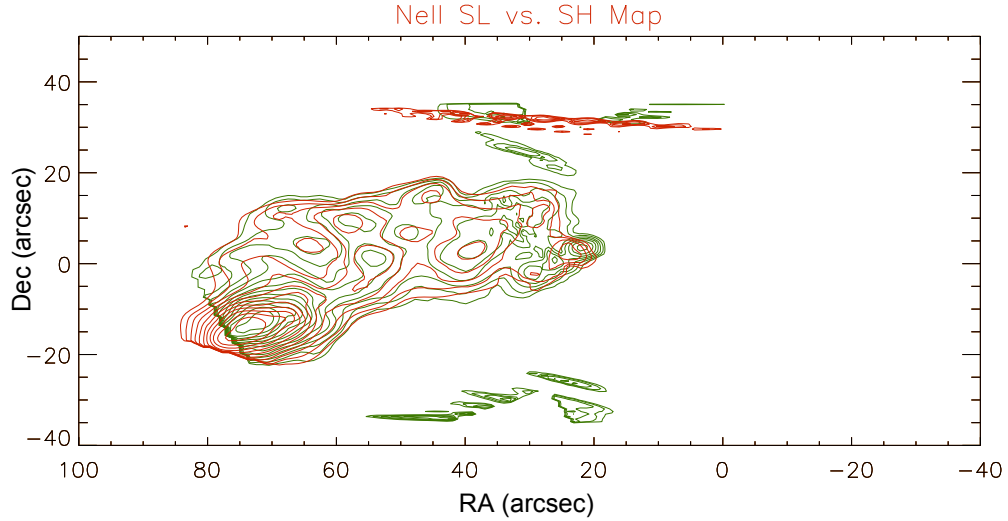
Figure 2.2 Comparison of [Ne II] [12.8 μm] observed in SH in 2004 (red) and in SL in 2007 (green). Although there are differences, individual features appear in both maps at the subpixel level.

that occur more than once at the 4σ level are considered to be permanently bad pixels and thus the grand rogue mask contains 25% more rogue pixels than a single campaign rogue mask. Bad pixels are fixed using a nearest neighbor routine (imclean.pro and imnan.pro).

Next we extract individual spectra using a modified version of SMART, not simply from each slit position, but from each individual resolution element of each slit position (Figure 2.3). In the case of SH and LH, we produce five (semi-)independent spectra, spatially separated by the resolution of a single pixel in the array; in SL we use 32 independent positions to generate spectra. The results suffer slightly (of order 10%) from stretching due to approximations in the pixel positions along the slit, but when properly rescaled are extremely consistent from module to module, even when observed independently years apart. Figure 2.2 is a comparison of SH and SL for the same spectral line, indicating why we are confident in our astrometry.

The spectra are then re-gridded onto a regular grid in RA and declination (Figure 2.3, upper right). Pixels with (nearly) identical positions are averaged together. We apply the slit loss correction function (SLCF) to correct for flux-calibrating created for point-sources, used by the SSC. The result is a downward
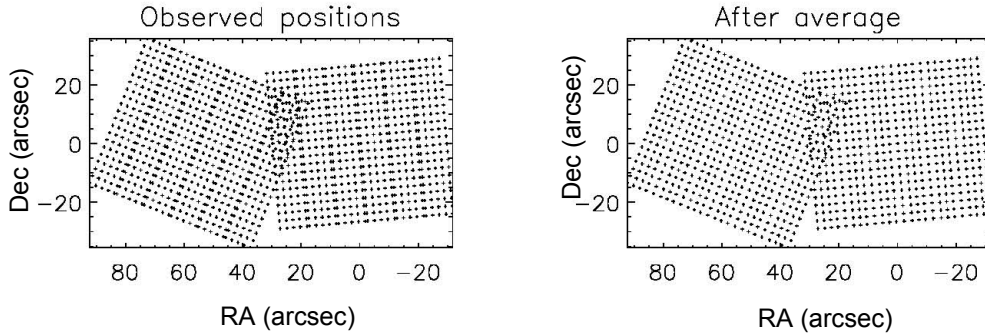
Figure 2.3 Map grid of SH observations of GGD37 from AORs 5005312 and 5005568. This sample shows how re-gridding occurs. In the left image, we plot the position of the all pixels derived from the central slit positions in the mapping sequence. In the right we show the grid after averaging nearby values together and renormalize the grid to even spacing.

correction to the flux of $\sim 60 - 90\%$ [3].

Finally, we determine continuum and line fluxes at each spatial position with the mapped region.[4] We fit a Gaussian line profile and up-to-second-order polynomial baseline at each wavelength of interest, individually choosing the order of the polynomials to achieve the best fit to the surrounding continuum. We calculate this fit twice; first with the line centroid and width as free parameters at a position of high S/N in the fitted spectral line, and then with a fixed value for the centroid and width generated by the first fit, varying only the height. This has the advantage of covering the positions in which the S/N ratio is lower than the best fit region, reducing the dependency of the fit on S/N ratio. As noted above, unless a line exhibits a velocity shift of more than 500 km/s or 5000 km/s (high and low resolution modules respectively), the centroid will not vary. The result is a datacube containing fluxes at every RA, Dec, and wavelength.

---

[3]Kindly provided to us by J.D. Smith

[4]The line-fitting was performed using a code built from a modern Levenberg-Marquardt routine called mpfit, developed by Craig Markwardt – see his IDL library at http://cow.physics.wisc.edu/ craigm/idl/ – a robust fitting routine that switches between the Gauss-Newton algorithm and the method of steepest descent as necessary.

2.3 General SED Characteristics of Protostars in the Mid-Infrared

What capabilities does the Spitzer Space Telescope have to aid in investigating young stars and outflows? Observations in the mid-infrared are limited to a few wavelength ranges that lie between the vast atmospheric absorption bands, due mostly to water vapor. Placing even a relatively small (0.85 meters in diameter) telescope in space, far away from the contaminating heat of Earth, allows unprecedented sensitivity on very short timescales. As such it is possible to survey large regions of the sky at previously unprobed wavelengths. Furthermore advanced adaptive optics techniques are now improving ground-based observations, which can be calibrated against this clean space-based data, providing a framework for future ground-based surveys after *Spitzer* has boiled off the last of its cryogens. Spectroscopic data is particularly valuable as it covers the entire range of features found between 5-40 μm, as well as emission from blackbody-like sources ranging in temperature from $\sim$ 100 K to 1500 K; this includes the majority of the archetypal bodies (dust, planetesimals, comets) in planetary systems that are heated by starlight or viscous dissipation, as well as weakly shocked gas. For the first time we can learn in detail what the parameter space of disk and envelope emission looks like in systems and clouds that are at different stages of development, allowing us to refine our understanding of the "typical" systems so that we can better identify the exceptional ones.

The 5-40 μm range covers a variety of spectral features, some resolved, and some unresolved by the low and high resolution IRS modules.

2.3.1 Broad Features

2.3.2 Continuum

The broadest feature of all is the continuum emission. The underlying flux from YSO systems is generally ascribed to three components. At the shortest wavelengths the stellar photosphere may be the dominant continuum feature (approximately represented as a blackbody centered at optical wavelengths based on the spectral type of the source, with T_{eff} between $\sim$ 3000 and 7000 K for M to F-

type stars). An ideal optically thick circumstellar disk, if present, would emit as a series of blackbodies at temperatures ranging from the dust sublimation radius (T $\sim$ 1400 K). The emission would trail off to colder temperatures as a function of distance from the central star (in the case of an optically thin disk) or distance below the disk surface and height above the midplane (in the case of optically thick partially flared disks) or as the accretion rate falls (in the case of accretion luminosity dominated SEDs). The final, coldest component is the circumstellar envelope– the infalling material feeding the system from the surrounding molecular cloud, which contributes to the SED primarily at wavelengths beyond 20 μm (although it is frequently correlated with high extinction and may result in strong adjustments to the SED at shorter wavelengths as well). Additionally, systems in which such cold components contribute significant flux can show signs of a veiled central source, lacking even an optical peak to identify properly the spectral type of the developing protostar.

2.3.3   Mineralogical or Solid-State Features

The broadest features are the silicate feature complexes at $\sim$ 10 μm (from Si-O stretching modes) and 18 μm (from O-Si-O bending modes) for grains at $\sim$ 300 K. Amorphous silicates – those without any defining internal structure – emit broad features with rounded peaks. The feature centroid and sub-peaks are used to fit different chemical species: primarily pyroxenes ($Mg_xFe_{1-x}SiO_3$) and olivines ($[Mg/Fe]SiO_4$), although silica (SiO_2) is also observed. Additionally grains of different sizes will have different centroid positions; it is possible to separate out the effects of grain growth and grain composition by careful fitting analysis (e.g. Sargent et al., 2006). It is thereby possible to probe the dust composition of the portions of the disk that fall within the temperature range covered by IRS wavelengths – generally the inner portions of the typical circumstellar YSO disk.

Amorphous silicates viewed through a cold envelope will appear in absorption in the SED, as they are re-emitted by the surrounding material. This is difficult to distinguish from edge-on YSO disks, which have a similar temperature gradient. Additionally there are viewing angles through which the envelope may be depleted, which can allow for both silicate emission from the disk (viewed nearly pole-on through a cavity in the envelope) and large infrared excess at longer wavelengths

from cold envelope material. Corrections due to extinction have their largest impact on the 10 μm silicate complex; because of the possibility of silicate self-absorption, an uncorrected silicate absorption feature can become an emission feature after reddening corrections are applied, and features that at first appear crystalline due to their jagged profiles can smooth into more amorphous features.

Amorphous silicate dust that reaches the inner disk or the outer disk layers may be processed through stellar radiation and annealed into crystalline structures. Crystalline silicates can provide narrower sharper peaked features at a variety of wavelengths, particularly around 10 μm and from $\sim$ 21 - 35 μm. With detailed lab opacities and spectral indices it is possible to uncover the relative abundance of a large variety of crystalline components in the disk, including annealed silica (dust grains baked at $\sim$ 1200 K for 5 hr) in addition to crystalline enstatite and forsterite.

2.3.4   Ices

A variety of ice absorption features are observed to originate primarily in the cold envelope material surrounding the more embedded sources, including H_2O (6 μm), a complex of features at 6.8 μm partially attributed to methanol (CH_3OH) and NH_4^+, CO_2 bending mode (15.2 μm) (Zasowski et al., 2009; Boogert et al., 2008; Pontoppidan et al., 2008). Detailed fitting of the 6 μm feature (Zasowski et al., 2009) suggests that although water ice is the dominant component – $\gtrsim$ 80% – additional contributions from other ices are significant. The 7.7 μm feature is generally attributed to solid CH_4. We attribute the 5.8 μm feature to a combination of H_2CO (formaldehyde) and HCOOH (formic acid) ices, and a weaker HCOOH feature has been identified at 7.2 μm. Finally it should be noted that the 15.2 μm feature will be double-peaked if the CO_2 ice formed outside of a matrix of H_2O (in which case it would appear as a single feature). This feature usually has a tail to longer wavelengths for which methanol would be responsible.

2.3.5   PAHs

Several complexes of polycyclic aromatic hydrocarbon (PAH) bending and vibrational mode features are scattered throughout the IRS wavelength range. Some

of the most prominent features are near ~ 8 μm and can dominate Spitzer-IRAC Band 4 emission, although PAH features often appear in all modules of the IRS (most strongly at 6.2, 7.7-7.9, 11.3, and 12.7 μm). PAH emission is generally stimulated by bombardment from UV photons; thus they are more commonly found among stars of earlier (more massive) spectral types, with more energetic winds and higher observed X-ray emission, although X-rays are noted in ~ 90 % of all YSOs in Taurus (Güdel et al., 2007). The ratios of various PAH features – and shifts in the central wavelengths of the features – are used to segregate the spectra into different types (Peeters et al., 2002; Sloan et al., 2005).

2.3.6 Absorption Features

The atmospheres of stars (and disks, should they be hot enough) exhibit absorption features in the shortest wavelengths of IRS; in particular we generally identify broad features at ~ 5.6 μm and 6.2 μm due to H_2O, as well as 8 μm attributed to SiO. These features are close enough in wavelength to the short wavelength ice features that it is important to disentangle them; this can be done most easily by fitting the features and comparing centroid positions.

2.3.7 Spectral Lines

Generally spectral lines are unresolved in the low-resolution IRS modules; many are resolved in high-resolution mode. There are a number of identified atomic, molecular, and ionized species that might appear in the SED of a YSO, possibly from a bipolar outflow originating from the central star, or from vaporous emission from the disk itself. Additionally background emission (particularly from active areas such as Cygnus) can dot the spectrum with more energetic species, including a range of excitation energies from 0.1 eV up to 97 eV. A forest of H_2O transitions appears in a few cases at wavelengths greater than 25 μm (and at shorter wavelengths as well in hotter regions), as well the lowest eight pure rotational lines of molecular hydrogen – H_2 S(0) - S(7). CO_2 gas emits a feature at 15 μm which can occasionally be seen arising from the broad trough of a CO_2 ice feature. In Chapter 4 we map an entire region of the sky rich in emission lines.

2.4 So what have we learned from IRS Observations of Protostars?

Ultimately we seek to learn about other solar systems not only to understand the development of the stars throughout the galaxy, but also to frame better the history of our own solar system as understood from meteoritics and planetary science. Many of these new findings can be connected with solar system models developed by meteoriticists and applied to specific cases in our own system. Was the water in the solar system delivered via a giant cascade from our natal envelope? Did the planets form within the first few million years of the sun's existence?

And what happens when this neat classification scheme is unsettled by violent events and cascades? In Chapter 3, I will discuss the case of runaway accretion in the form of FU Orionis events. And in Chapter 4 I will discuss the effects that such instabilities have on their ambient medium, possibly reseeding it for further star formation down the road.

3 IRS Observations of FU Orionis Objects

3.1 Introduction

FU Orionis variables [1] are starlike objects, in the sense that they appear to be distant point-sources– although they are often extinguished and frequently appear connected to extended arc-like structures. They are observationally identified by an optical outburst of 5 magnitudes or more (Herbig, 1977). This sudden jump in intensity is not particularly consistent across the class– the flare may reach maximum intensity within $\sim$ 1 yr (FU Ori, V1057 Cyg) or may take as long as $\sim$ 20 yr (V1515 Cyg), while the rate of decline from maximum light varies considerably as well. The e-fold decay time of the flux at B-band of the prototypical object, FU Orionis itself, is $\sim$ 100 yr. Classification of FU Ori objects by their visible spectral energy distributions indicate F-G supergiant spectral types, corresponding to effective temperatures of $\sim$ 6000-7000 K, but the near-infrared molecular absorption bands are typical of M supergiants with much lower effective temperatures (Mould et al., 1978). Thus in the optical (ie. visible) and near-infrared they are typified by an emission peak that is far wider than that characterized by a single effective temperature stellar photosphere, suggesting that the emission comes from a variety of temperatures distributed radially in the system; thus even the optical emission is not from the central protostar, but from the extremely bright circumstellar disk.

It is extremely difficult to determine spectral types for these stars from previous observations because the derived spectral type and effective temperature is different when measured at different wavelengths. These systems are often shrouded

---

[1]The science in this chapter appeared as Green et al. (2006).

in considerable nebulosity, which is also consistent with extended excess emission, and suggests that we may be systematically undercounting such events. Normal protostellar disks (see Chapters 1 & 2) do not exhibit such strong emission in the optical and near-infrared. What is causing this sudden temperature increase in the disk?

The spectral energy distribution of a typical protostar can be characterized by a multi-component model such as that used by Osorio et al. (2003): in the normal case the stellar photosphere, represented approximately by a single temperature blackbody centered at optical wavelengths is used to determine the optical spectral type; the disk, which contains much colder material at a variety of temperatures; and possibly an envelope of even colder material surrounding the system with a peak temperature at mid or far-infrared wavelengths. What distinguishes the SEDs of these sources from CTTS or an embedded protostar with an envelope is the breadth of the optical peak, which cannot be fit by a single temperature blackbody. The peak can be modeled as a series of annuli of blackbodies at very high temperatures. FUor disks are thought to dominate the luminosity at these wavelengths, heated not by the central source as in T Tauri stars (e.g. Hartmann & Kenyon, 1987a), but by viscous dissipation of energy released from the elevated level of accretion in the disk, and thus the stellar photosphere is not contributing significantly even at optical wavelengths, and any classification based on the optical peak is misleading. Additionally FU Orionis objects exhibit substantial near-infrared excess emission (e.g. Cohen & Woolf, 1971; Rieke et al., 1972; Simon et al., 1972; Grasdalen, 1973; Simon, 1975). This suggests the presence of a circumstellar disk of material colder than the photosphere.

Outbursting behavior had previously been recognized in close binary systems, and interpreted as the result of some kind of instability in accretion disks. Researchers who studied such accreting binary systems were the first to suggest that FU Ori outbursts were similarly the result of some temporary rapid increase in the rate of mass accretion in a circumstellar disk (Paczynski, 1976; Lin & Papaloizou, 1985; Hartmann & Kenyon, 1985). The accretion rate was understood to be so high that the disk itself might be producing the optical spectrum, completely overwhelming the luminosity of the stellar photosphere during the outburst phase.

Hartmann & Kenyon (1985), applied accretion disk models to pre-main se-

quence objects to suggest that mass accretion rates for FU Ori objects were $\sim$ 10^{-4} $M_\odot$ yr^{-1} to explain the observed spectra and accretion luminosities, at the high end rates for Class 0/I protostars ($\sim 10^{(-7)-(-4)}$ $M_\odot$ yr^{-1}). The frequency of observed FU Ori events, while still highly uncertain, exceeds the expected frequency of star formation in the solar neighborhood by a factor of five or more; thus, at least some stars must have repetitive outbursts. The outburst is estimated to last ~ 100 yr, but the light curves of each FU Ori candidate are different and none have yet settled down to their original pre-outburst state.

FU Ori outbursts appear to occur in the youngest protostellar objects. This agrees with the old suggestion that protostellar disks may outshine their central stars at very early ages ($\sim 10^5$ yr). The large extinctions and far-infrared emission of many FUors (most notably V1057 Cygni, V1515 Cygni, and V346 Normae from this sample) suggests that protostellar envelopes are still raining material down onto the disk. This mass infall may pile up material until the disk is able to rid itself rapidly of excess material by accretion onto the central star (Kenyon & Hartmann, 1991, hereafter KH91).

We have taken 5-35 μm IRS spectra of five FU Orionis objects: FU Ori, V1515 Cyg, V1057 Cyg, BBW 76, and V346 Nor. All but V346 Nor reveal amorphous silicate grains in emission at 10 μm and 20 μm, and show water-vapor absorption bands at 5.8 and 6.8 μm and SiO or possibly methane absorption at 8 μm. These absorption features closely match these bands in model stellar photospheres — signs of the gaseous photospheres of the inner regions of these objects' accretion disks. The continuum emission at 5-8 μm is also consistent with such disks, and, for FU Orionis and BBW 76, longer-wavelength emission may be fit by a model which includes moderate disk flaring. V1057 Cyg and V1515 Cyg have much more emission at longer wavelengths than the others, perhaps evidence of substantial remnant of their natal, infalling envelopes.

Table 3.1.   Observations Times and AOR IDs

Object	AORID	Date	JD
V1057 Cyg	3570176	2003-12-15	2452988
V346 Nor	3570688	2004-02-27	2453063
FU Ori	3569920	2004-03-04	2453068
BBW 76	3571200	2004-04-14	2453110
V1515 Cyg	3570432	2004-05-11	2453137

Note. — Spitzer-IRS observation log of the FU Ori objects.

3.2   Observations

3.2.1   IRS observations

Five FU Ori objects – FU Ori, V1057 Cyg, V1515 Cyg, BBW 76, and V346 Nor – were observed between December 2003 and May 2004 using Spitzer-IRS. Table 3.1 is a journal of the observations. The data reduction was covered in Chapter 2, with a few differences as described below.

All of these objects were observed in both orders of the IRS SL. BBW 76 was also observed in both orders of the IRS LL. The other targets were observed in IRS SH and LH. We began with the non-flatfielded ("droop") data product from the Spitzer Science Center IRS calibration pipeline version S11.0.2, consisting of 2-D spectral-spatial, non-flatfielded images. The final spectra are the usual averages of the nod positions as mentioned in Chapter 2, except for V346 Nor, for which only one nod position was used. In two cases, BBW 76 and V346 Nor, slight pointing errors led to 20% flux-density discrepancies between spectra from SL and the other (wider-slit) modules, which we resolved by increasing the SL signal by a scalar factor. As no significant narrow spectral lines were detected in the high-resolution data for V1057 Cyg, FU Ori, and V346 Nor, we improved the signal-to-noise ratio in these spectra by convolution to lower spectral resolution, $\lambda/\Delta\lambda \sim 120$. We estimate the photometric accuracy of the final spectra to be approximately 5-10%.

3.2.2 Optical and near-IR photometry

At any point in time, the continuum emission in our IRS spectra is a smooth extension of the shorter-wavelength emission. However, because FU Ori objects display short-term variation in addition to the steady decay of the outburst, comparison to shorter-wavelength observations from the same epoch as the Spitzer-IRS observations is preferred. Thus we employ UBVR observations of V1057 Cyg, FU Ori, and V1515 Cyg that were made at Maidanak Observatory throughout 2004, the continuation of a long monitoring campaign begun in 1981 for V1057 Cyg and V1515 Cyg, and in 1984 for FU Ori. Observations in this program before 2004 are available online (see Ibrahimov, 1996, 1999; Clarke et al., 2005); those for 2004, contemporaneous with our Spitzer-IRS observations, are presented in tables 3.2, 3.3, and 3.4. The data were taken with two 60-cm Zeiss reflectors and the 48-cm AZT-14 reflector equipped with identical photon-counting photometers, reproducing the Morgan-Johnson system of photometry. The observations were carried out using differences with nearby reference stars. The RMS uncertainty of a single measurement is $\Delta V = \Delta(V - R) = 0.015$ mag, $\Delta(B - V) = 0.02$ mag. The RMS uncertainty in U-B was approximately 0.03 mag for FU Ori, and somewhat larger for V1057 Cyg and V1515 Cyg. The resulting average visible-UV photometry for V1057 Cyg, FU Ori, V1515 Cyg and BBW 76 is displayed in table 3.5.

For BBW 76, we used the visible-UV data compiled by Reipurth et al. (2002) to determine average decay rates between 1983 and 1990 for UBV photometry and linearly extrapolate values for 2004. The decay rate in the B and V-band was ~ 0.02 mag yr^{-1}, while the U-band decay rate was ~ 0.003 mag yr^{-1}. Next we calculated the decay at near-infrared wavelengths (J, H, and K_S bands) by comparison of 1983 and 1998 (2MASS) observations. This yielded a decay rate of ~ 0.026 mag yr^{-1}. We assumed this rate to apply to R as well, and extrapolated to 2004 from the 1994 data in Reipurth et al. (2002).

Contemporaneous near-infrared photometry is not available for any of our targets, but comparison of older observations with those in the 2MASS point-source catalogue (PSC), as in BBW 76 above, indicate that the extrapolation from the 2MASS epoch (~ 1998) to the IRS epoch is negligibly small. Thus for V1057 Cyg, V1515 Cyg, and BBW 76 we adopt the 2MASS PSC J, H, and K_S magnitudes. FU Ori is too bright to have been included in the 2MASS PSC; instead we

used the 1989 near-infrared observations by KH91. Though these observations are significantly older than 2MASS, the M-band ($\lambda = 4.8~\mu$m) flux density matches closely at the shortest wavelengths in the IRS spectrum, indicating that FU Ori has not varied significantly at these wavelengths over the past fifteen years.

Table 3.2.   V1057 Cyg in 2004

JD	V (mag)	U-B	B-V	V-R
53185.2727	12.361		1.875	1.737
53186.2465	12.368		1.890	1.755
53187.2281	12.364		1.853	1.749
53189.2199	12.374		1.932	1.764
53190.2565	12.388		1.980	1.772
53195.2785	12.444	1.484	1.892	1.769
53196.2637	12.469	0.986	1.875	1.770
53205.4167	12.463		1.906	1.798
53227.4443	12.402	1.804	1.958	1.759
53228.3340	12.451	1.861	1.918	1.790
53229.3367	12.450	2.266	1.942	1.789
53230.2871	12.429	0.706	1.900	1.783
53231.3084	12.441	1.858	1.873	1.795
53232.2428	12.408		1.939	1.759
53233.2331	12.412	1.106	1.904	1.788
53234.2302	12.366	1.665	1.976	1.767
53235.3605	12.426		1.939	1.736
53236.3604	12.466	1.190	1.906	1.776
53237.3542	12.495	1.418	1.876	1.806
53238.2251	12.483	1.123	1.909	1.788
53240.2332	12.474	1.123	1.907	1.779
53241.3390	12.477	2.277	1.886	1.775
53242.3228	12.499	1.616	1.956	1.793
53243.3501	12.488		1.935	1.773
53250.2696	12.503		1.937	1.821
53251.2416	12.469	1.555	1.943	1.792
53252.2603	12.480		1.891	1.789
53253.2421	12.458		1.923	1.771
53254.2550	12.487	1.032	1.933	1.794
53255.2796	12.495	2.030	1.887	1.771
53256.2439	12.491		1.885	1.794
53258.2582	12.480	1.590	1.928	1.767
53259.3363	12.460		1.912	1.774
53260.2522	12.513	1.340	1.882	1.782
53261.2235	12.485	1.958	1.905	1.767
53262.2218	12.478	2.552	1.906	1.759
53263.2217	12.446	1.384	1.952	1.756
53263.2386	12.388		2.096	1.747
53264.2634	12.487	2.958	1.914	1.773
53264.2891	12.527		2.070	1.768
53266.1891	12.513	1.854	2.016	1.766
53266.2446	12.511	1.151	1.894	1.784
53267.2124	12.482	1.375	1.909	1.771

Table 3.2 (cont'd)

JD	V (mag)	U-B	B-V	V-R
53267.2236	12.488	1.088	2.032	1.742
53268.1896	12.537	1.237	1.975	1.785
53270.2043	12.523		1.904	1.763
53271.2405	12.537		1.921	1.792
53272.2170	12.486		1.939	1.787
53273.2196	12.490		1.951	1.765
53289.1960	12.600	2.405	2.013	1.802
53291.2346	12.644		1.955	1.835
53292.2314	12.600	1.860	1.965	1.833
53310.1500	12.771		2.041	1.884

Note. — The UBVR photometry for V1515 Cygni, FU Orionis and V1057 Cygni, was observed by Mansur Ibrahimov at Maidanak Observatory in 2004; the average magnitude is shown here. The UBVR photometry for BBW 76 is from Reipurth et al. (2002) and has been projected to 2004, using linear decline rates from the data (see text): U - 0.003 mag yr^{-1}, B - 0.014 mag yr^{-1}, V - 0.023 mag yr^{-1}, R - 0.026 mag yr^{-1}. Also included are estimated visual extinction correction factors for each object.

3.3 Observational results

The IRS spectra of our five program objects are displayed in Figures 3.1, 3.2, and 3.3. Four of the five objects — FU Ori, BBW 76, V1515 Cyg, and V1057 Cyg — have silicate emission features (peaking at $\lambda = 10$ and 18 μm), and steeply-rising continua shortward of the silicate features. At the shorter wavelengths the spectra of these four objects are similar. In each case, the 5-9 μm continuum (Figure 3.2) is modulated by broad absorptions at $\lambda = 5.8$, 6.8 and 8.0 μm. Based on comparisons with IRS spectra of low-mass stars (Roellig et al., 2004), and model photospheres of low-mass stars and brown dwarfs (e.g., Allard et al., 2000), we identify the two shorter wavelength features with a collection of rotation-vibration bands in gaseous H_2O. Calvet et al. (1991) previously noted that features between 1.4 and 2.4 μm match models of water vapor absorption. Tentatively we suggest that the feature at 8 μm is the fundamental rotation-vibration band of gaseous SiO, but note that it could potentially be due to or influenced by absorption by methane (CH_4) as well.

Suppose that FU Ori disks exhibit gaseous features at effective temperatures

Table 3.3.   FU Orionis in 2004

JD	V (mag)	U-B	B-V	V-R
53278.4601	9.654	0.682	1.361	1.169
53280.4504	9.629	0.735	1.342	1.159
53281.4718	9.639	0.799	1.349	1.173
53283.4811	9.682	0.757	1.349	1.194
53284.4826	9.677	0.748	1.347	1.173
53299.4914	9.676	0.787	1.346	1.183
53309.4760	9.659		1.350	1.176
53310.4598	9.661		1.338	1.175
53311.4993	9.652		1.373	1.175

Table 3.4.   V1515 Cyg in 2004

JD	V (mag)	U-B	B-V	V-R
53184.2758	12.973	0.620	1.599	1.509
53185.2461	12.990		1.597	1.531
53186.2267	12.936		1.563	1.485
53187.2125	12.949		1.566	1.477
53189.2030	12.926		1.764	1.502
53190.2430	12.957		1.741	1.536
53193.2865	12.950	1.211	1.734	1.467
53195.2580	12.866			1.483
53196.2507	12.856	1.045	1.642	1.481
53205.3837	13.048	1.056	1.634	1.523
53224.3872	13.018	0.722	1.650	1.542
53226.4111	13.062	1.302	1.640	1.530
53227.3657	13.046	1.560	1.660	1.524
53228.3002	13.052	1.228	1.688	1.518
53229.2663	13.073	1.011	1.674	1.506
53251.2222	13.054		1.695	1.535
53252.2431	13.115		1.642	1.586
53253.2262	13.116		1.670	1.561
53254.2282	13.118		1.680	1.521
53255.2192	13.175		1.637	1.543
53256.2161	13.160		1.649	1.508
53258.2446	13.199	1.185	1.665	1.562
53259.3272	13.137	1.705	1.680	1.528
53260.2360	13.121	2.027	1.697	1.543
53261.2048	13.054	2.366	1.733	1.545
53262.2066	13.066	1.968	1.645	1.545
53263.2063	13.049	0.660	1.689	1.549
53264.2492	13.064	1.191	1.683	1.520
53266.2246	13.071	1.865	1.636	1.564
53267.1977	13.033	1.379	1.660	1.505
53268.2515	12.977		1.664	1.489
53270.1930	12.952		1.624	1.507
53271.2320	12.963		1.643	1.490
53272.1869	13.011		1.586	1.527
53273.1885	13.039		1.654	1.530
53289.1777	13.108	1.347	1.632	1.536
53292.1552	13.042	0.912	1.615	1.489

Table 3.5.   Estimated 2004 Brightness Levels and Visual Extinction

Object	U(mag)	B(mag)	V(mag)	R(mag)	A_V
V1057 Cyg	17.00	14.70	12.65	10.85	3.7
FU Ori	11.81	11.01	9.67	8.49	1.9
BBW 76	14.23	14.04	12.59	11.81	2.2
V1515 Cyg	16.50	14.74	13.11	11.57	3.2

Note. — Current UBVR photometry and uncorrected for redden-
ing, and assumed reddening corrections for the FU Ori objects. The
average values for V1057 Cyg, V1515 Cyg, and FU Ori are com-
puted from tables 3.2, 3.3, and 3.4. The values for BBW 76 are
extrapolations from older data, as explained in the text.

> 1400 K, but only featureless dust continuum at lower effective temperatures. The continuum corresponds to the hottest dust temperatures seen in CTTS disks (Muzerolle et al., 2003). In this case the dust opacity dominates the gaseous opacity at temperatures $\lesssim 1400$ K. From the standard steady, blackbody FU Ori disk model with a large outer radius (Kenyon et al., 1988), we estimate that almost half of the flux at 6 μm, and about a third of the flux at 8 μm, is contributed by annuli hotter than 1400 K. This model predicts that we should detect gaseous features at these wavelengths in FU Ori objects, diluted by dust continuum emission from cooler disk regions. The appearance of strong emission due to dust at just slightly longer wavelengths (Figure 3.1) warns us that the 5-9 μm continuum emitted by dust grains in cooler parts of the accretion disk is probably still significant here, as previously found in the spectra of CTTSs (Furlan, 2006). However, neither suitable models nor observed spectra of disk photospheres at mid-infrared wavelengths yet exist for assessment of the dust-continuum dilution of the gaseous features. The spectra of FU Ori, BBW 76, V1515 Cyg, and V1057 Cyg are not as similar at the longer IRS wavelengths: the Cygnus objects are quite a bit redder at $\lambda = 15 - 40$ μm than the other two, indicating a greater predominance in these objects of emission by colder dust.

3.3.1   V346 Normae

In contrast to the others, V346 Nor shows strong silicate absorption, consistent with its large visual extinction; Graham & Frogel (1985) estimate $A_V \sim 6.2$ mag.
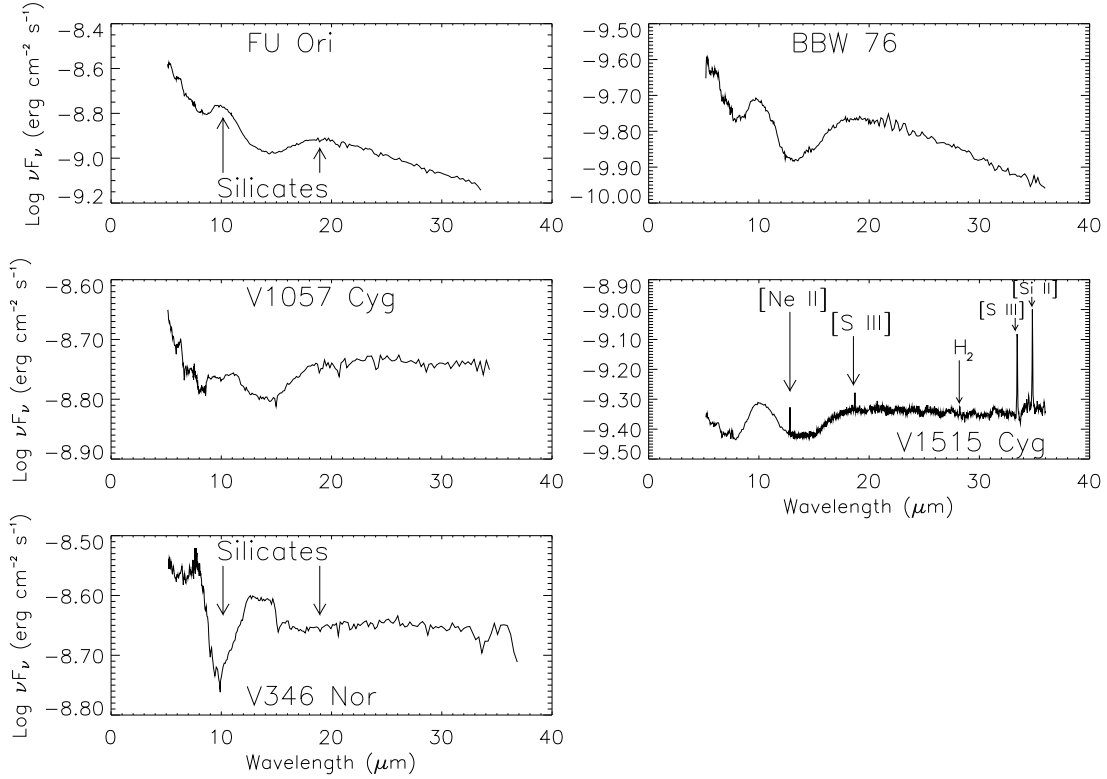
Figure 3.1   Observed IRS spectra of FU Orionis variables, uncorrected for reddening. The data for BBW 76 and V1515 Cygni are shown at full resolution: BBW 76 was a low resolution observation, and we show the high resolution data for V1515 Cygni in order to display the spectral lines. The data for the other three objects have been rebinned to low resolution. As discussed in the text, the ionic emission lines in V1515 Cyg arise in the foreground or the background.

Figure 3.3 is a comparison of IRS spectra for V346 Nor and a typical Class I young stellar object, IRAS 04016+2610 (Watson et al., 2004). The spectra are quite similar, and thus the identity of the features is the same as in Class I objects, namely water, "methanol", and carbon dioxide ices, and amorphous silicates.

3.3.2   V1057 Cygni

The 10 μm silicate feature of V1057 Cyg appears different from the others. As we show later, after correction by the adopted $A_V = 3.7$, using a reddening curve from Savage & Mathis (1979) the difference vanishes (Figure 3.4). Thus the appearance of the feature is due to selective extinction, rather than difference in dust composition. After subtracting a continuum derived from the 6-8 μm
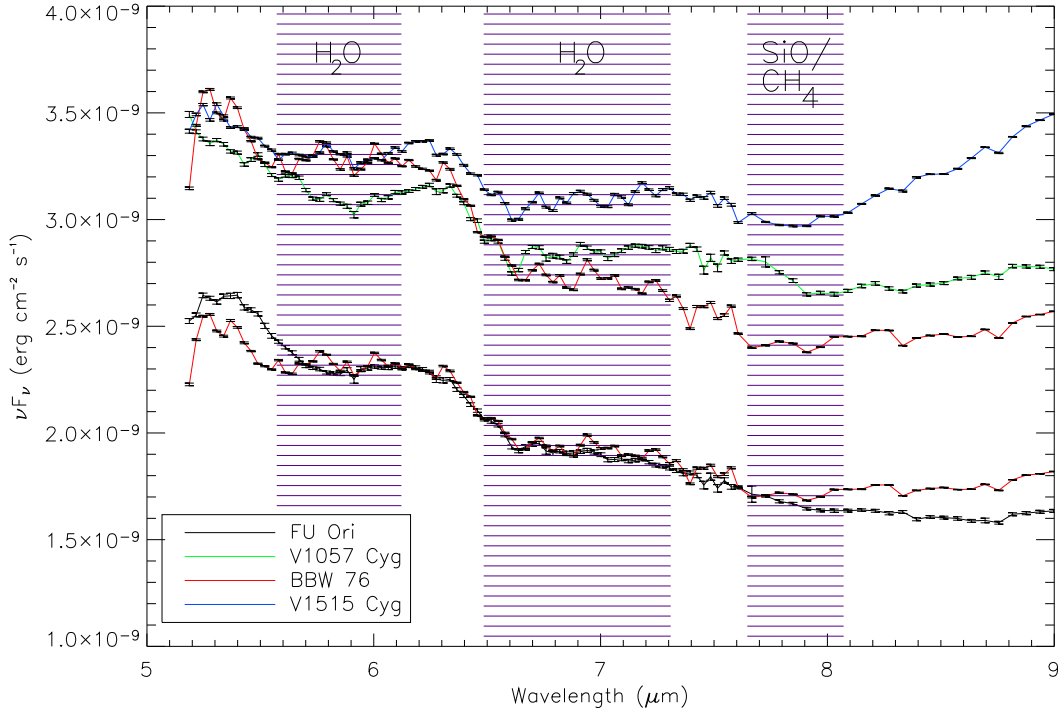
Figure 3.2 Comparison of the 5-8 μm region of the four FU Ori objects show-ing gaseous absorption features: H_2O absorption bands 5.8 and 6.8 μm and an SiO band at 8 μm. The spectra have been scaled, and BBW 76 is shown twice at different scales for comparison to the sources with more emission at longer wave-lengths (V1057 Cyg, V1515 Cyg), and to the source it most closely resembles (FU Ori). The error bars in the plot are derived from the difference of the two nod positions.

region, and deriving an emissivity based on a single temperature model for the dust grains (Sargent et al., 2006), we find that the peak of the silicate emission is at 9.5 μm, which is indicative of amorphous silicates of pyroxene composition. This is a common component of CTTS disks (Demyk et al., 2000; Sargent et al., 2006), and within the usual range of composition of interstellar dust. We have not attempted such a fit to the silicate features of the other objects in the study; their silicate features have approximately the same peak wavelength and width as those of V1057 Cyg (see Figure 3.4). They all appear smooth and should yield composition similar to V1057 Cyg.
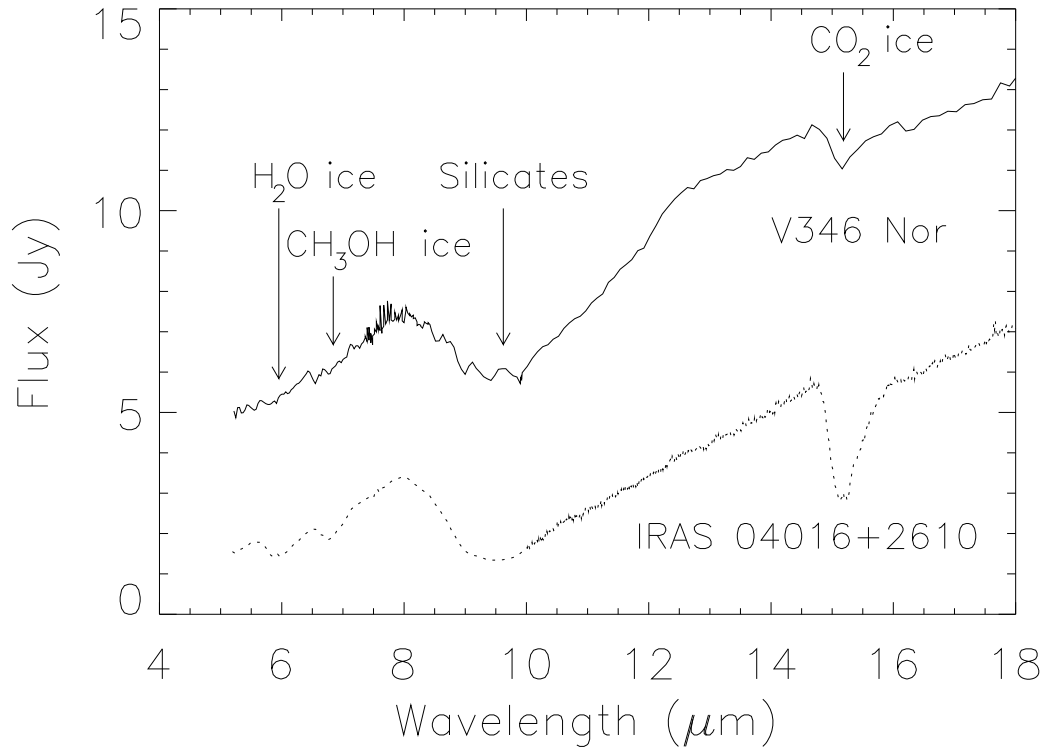
Figure 3.3 Comparison of the 5-18 μm region of V346 Nor to the Class I YSO IRAS 04016+2610 (Watson et al., 2004). The spectra are unscaled, although V346 Nor has been rebinned to low resolution. The spectrum of V346 Nor is considerably more noisy despite being brighter, because of significant telescope pointing errors.

3.3.3 V1515 Cygni

As is common in the Cygnus clouds, the line of sight toward V1515 Cyg intersects a great deal of foreground and background nebulosity, and as a result the spectrum exhibits many spectral features from ions, molecules and small dust grains. Most prominent are the infrared bands identified with polycyclic aromatic hydrocarbons (PAHs), at $\lambda = 6.2$, 7.7, 8.6 and 11.3 μm. This emission is removed almost completely by the off-order sky subtraction carried out for SL spectra during data reduction, and thus does not appear in the spectrum shown in Figure 3.1. That it subtracts away so precisely is an indication that the emitting material is neither associated with, nor excited by, V1515 Cyg. The same is true for [Ne II] emission at $\lambda = 12.8$ μm. For wavelengths longward of 14 μm, observed only with SH and LH, we lack a nearby blank-sky spectrum for subtraction, and thus spectral lines

from extended nebulosity appear in Figure 3.1: [S III] (18.7 μm and 33.4 μm), H$_2$ (28.2 μm), and [Si II] (34.8 μm). We expect that all these lines therein would subtract away as precisely as [Ne II], the SH profile of which we leave in Figure 3.1 for comparison.
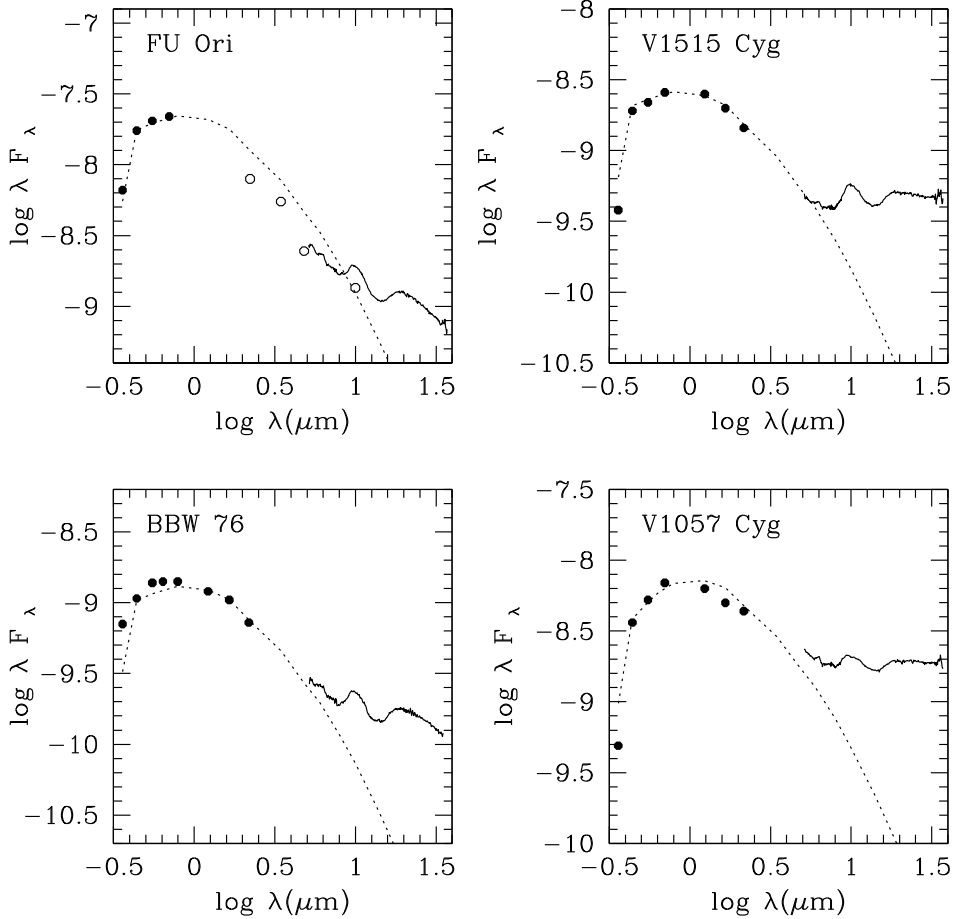

Figure 3.4 Dereddened IRS spectra (solid line) and older optical and near-IR ground-based data (circles); the dashed line is a fit from the steady accretion model using standard photometric colors down to 3000 K from Kenyon & Hartmann 1995 (Table A5) with fit parameters listed in Table 6. Below 3000 K, blackbodies are used. The value of A$_V$ for each object is listed in Table 5. The filled optical data circles are observations made at Maidanak Observatory during 2004; the filled near-IR data circles are 2MASS observations circa 1998; the open circles are 1989 KLMN bolometer data from KH91.

3.4 Discussion

3.4.1 Emission by the hot inner disk: comparison to simple models

To compare the SEDs of the four moderately-reddened FU Ori objects with disk models, it is necessary to make extinction corrections, as most of the disk luminosity is radiated at visible wavelengths. Extinction corrections are uncertain because these systems do not have single, well-defined effective temperatures; this leads to larger uncertainties in SED shapes and system luminosities. We apply extinction corrections to the ground-based photometry (Savage & Mathis, 1979) and the IRS spectra, assuming that the optical depth at 9.7 μm $\tau_{9.7} = A_V/18$ (Schutte et al., 1998; Draine, 2003). These extinction values are reasonably consistent with previous estimates in the literature but may differ by as much as 0.2 to 0.5 magnitudes in A_V. This in turn leads to an uncertainty in the peak of the SED, generally around 1 μm or a little less, of order 20-30%, with a similar uncertainty in the system luminosity for a given distance. The resulting, corrected spectra appear in Figure 3.4.

In Figure 3.4, we also show SEDs for steady accretion disk models assuming no inclination along the line-of-sight. The most common steady accretion disk models (e.g., Hartmann, 1998) assume the disk radiates as a blackbody at a temperature that varies with radius R according to

$$T_d^4 = \frac{3GM\dot{M}}{8\pi R^3 \sigma} \left[1 - \left(\frac{R_i}{R}\right)^{1/2}\right] \tag{3.1}$$

The maximum temperature of the disk is then given by

$$T_{max} = 0.488 \left(\frac{3GM\dot{M}}{8\pi R_i^3 \sigma}\right)^{1/4} \tag{3.2}$$

which occurs at

$$R_{max} = \frac{49}{36} R_i \tag{3.3}$$

Thus the total luminosity can be calculated:

$$L_\nu \;=\; \int_{R_{in}}^{R_{out}} \pi S_\nu T_d(R) 2\pi R dR \qquad\qquad (3.4)$$

assuming no inclination along the line-of-sight . Rather than using blackbodies ($S_\nu = B_\nu(T)$) we used photospheric emission computed using the photometric colors of standard stars taken from Table A5 of Kenyon & Hartmann (1995) to provide a slightly more realistic estimate of real disk flux density at short wavelengths (blackbodies are used at long wavelengths and for all wavelengths at disk temperatures below 3000 K). The same disk model is used for FU Ori, BBW 76, and V1515 Cyg, slightly scaled in luminosity, for ease of comparison; for V1057 Cyg we have used a disk model with a slightly lower T_{max} (table 3.6). Steady disk models are in fair to good agreement with the observations shortward of about 6 μm, but at longer wavelengths there is more flux than would be predicted by the models.

Disks heated from the outside have thermal inversions, a property which explains the silicate emission features (Calvet et al., 1992). In contrast, FU Ori objects have optical and near-infrared absorption features which are interpreted as resulting from dominance of internal heating by viscous dissipation (Hartmann & Kenyon, 1985, 1987a,b). All the FU Ori objects in Figure 3.4 show silicate emission features at 10 and 18 μm, whereas at shorter wavelengths absorption bands are observed. It therefore seems likely that the spectrum longward of about 8 μm or so should be considered in terms of irradiation, either of a flared disk or an envelope. We therefore first analyze the short-wavelength IRS SEDs in terms of accretion disk models and then consider irradiation of disks and envelopes for explaining the longer wavelength region in section 3.4.3 below.

3.4.2 Disk models with radially-variable accretion rate

FU Ori stands out in Figure 3.4 because its SED appears to be a bit narrower, with less infrared emission, than a standard steady disk model. This had been found before (e.g., KH91, Figure 5) without explicit comment. Of course, as the luminosity of FU Ori objects varies with time, they cannot be represented precisely by steady accretion disks. Moreover, thermal instability models of FU Ori outbursts, which can explain rapid rise times (Bell & Lin, 1994; Bell et al.,

1995), predict that only an inner region of the disk participates in the outburst; this implies that, beyond a certain radius, the accretion rate is lower, reducing the amount of long-wavelength emission from outer, cooler regions. Thus we have also constructed simple disk models of this type, with results as shown in Figure 3.5.

The upper left panel of Figure 3.5 (a) shows the FU Ori SED with various disk models. Since the Bell & Lin (1994) and the Bell et al. (1995) FU Ori models predict a much higher accretion rate in outburst within $\sim 20\ R_\odot$ than outside this radius (where the accretion rates tends toward the supplied infall rate), a first approximation might be to assume that the outer disk accretion rate is so low that the disk is effectively truncated at some radius. However, it is clear from our spectra that disk models with substantial accretion rates must extend well past 20 $R_\odot$ to explain the observations (Figure 3.7). Steady disk models need to extend to $\sim 100\ R_\odot$ or more to explain our FU Ori spectra. A more realistic approximation in the thermal instability models would be to assume a lower but non-zero accretion rate and steady disk temperature distribution outside of the radius at which the thermal instability is triggered. As shown in the upper left panel of Figure 3.5 (a), a model in which the accretion rate is arbitrarily dropped by a factor of ten at $\sim 30\ R_\odot$ does a reasonably good job of joining to the IRS spectrum. Again, this requires an accretion rate in the disk which is two orders of magnitude higher than typical T Tauri rates ($\sim 10^{-8}$ $M_\odot\,\mathrm{yr}^{-1}$ in Taurus; Calvet et al., 2004), out to 100 $R_\odot$ or more.

These models of FU Ori have higher maximum temperatures, 7710 K, than the 7200 K adopted by Kenyon et al. (1988). Part of the difference may be due to the adoption by Kenyon et al. (1988) of a constant inner temperature interior to $1.36R_*$, whereas in our steady accretion disk models the peak temperature is at this radius and then declines inward assuming a slowly-rotating central star; (e.g. see Hartmann, 1998). We have also examined the effect of dropping the maximum temperature to correspond to a decrease in extinction of $\Delta A_V = 0.3$ in visual magnitudes (certainly within the uncertainties), shown in Figure 3.5 (b). Although the new model disks are less luminous, with a lower T_{max} of 7140 K, there is little difference in the model comparison at long wavelengths, because the SED shifts slightly toward longer wavelengths, compensating for the decrease in system luminosity. Thus the conclusion that the disk of FU Ori must be rapidly
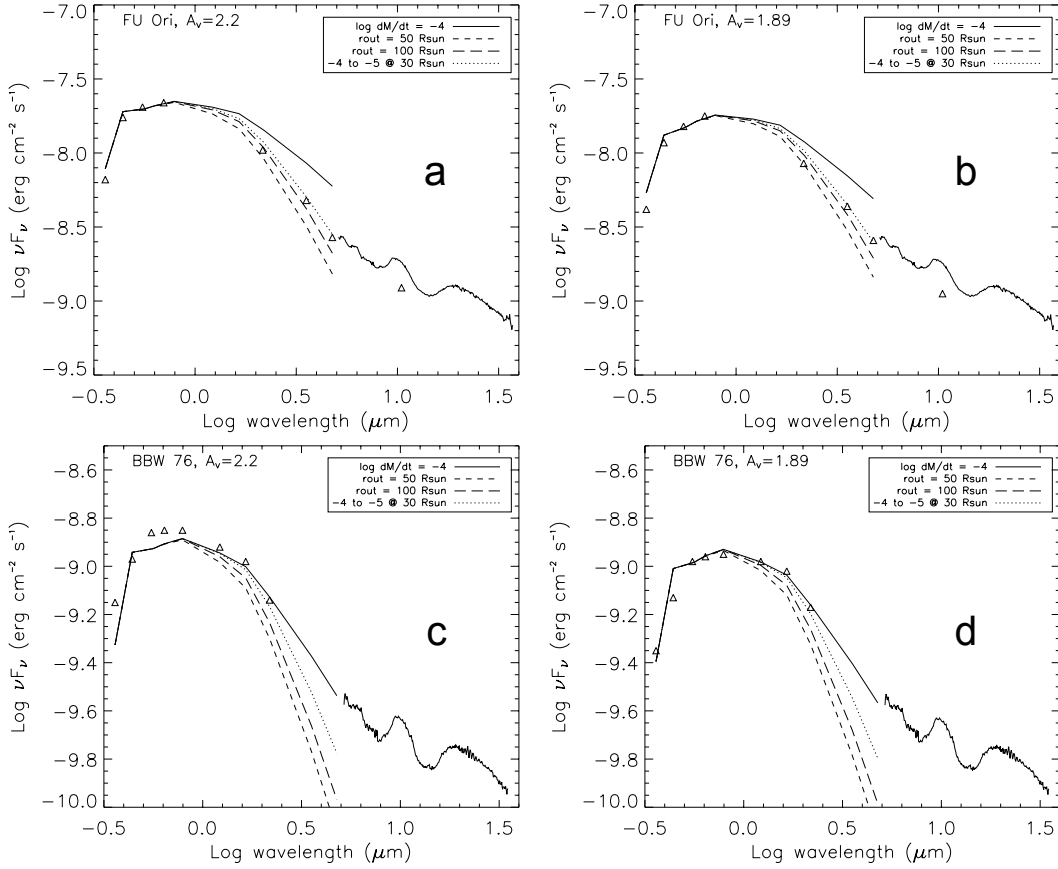
Figure 3.5 Comparison of different disk models of FU Orionis with varying conditions in the outer disk. In each plot, the solid line represents a disk with a constant accretion rate of 10^{-4} $M_\odot\,\mathrm{yr}^{-1}$. The dotted line represents a model where the accretion rate is decreased to 10^{-5} $M_\odot\,\mathrm{yr}^{-1}$ beyond 30 $R_\odot$. The longer dashed line represents a disk which is truncated beyond 100 $R_\odot$, and the disk represented by the shorter dashed line is truncated beyond 50 $R_\odot$. a) The model shown for FU Ori uses the values given in Table 3.6. b) The same comparison after applying a lower extinction correction, assuming $A_V = 1.89$, and reducing $M\dot{M}$ from 1.5 to 1.1. For this model, $T_{max} = 7140$ K. c) The same comparison for BBW 76. The parameters are taken from table 3.6. d) $M\dot{M}$ has been reduced from 0.72 to 0.65, consequently reducing T_{max} to 7140 K. The optical photometry in the case of BBW 76 does not match the disk model as well as it did for FU Ori, but the extended steady disk model which passes through the 2MASS JHK data connects well to the IRS spectrum.

accreting out to of order 100 $R_\odot$ or more appears to be insensitive to plausible changes in the extinction estimate.

Also shown in Figure 3.5 (c,d) is a comparison of the SED of BBW 76 with a steady disk model similar to that used for FU Ori - that is, a disk model with the same maximum temperature, but with a slightly smaller inner radius (Table 3.6). The optical photometry does not match the disk model as well as in FU Ori. On the other hand, the extended steady disk model which passes through the recent 2MASS data points joins fairly well to the IRS spectrum. Again, the conclusion is that BBW 76 has relatively high accretion rates out to radii of order 100 $R_\odot$ or more.

As shown in Figure 3.4, the steady disk model which passes through the 2MASS photometric points in V1515 Cyg extrapolates very well to the short-wavelength end of the IRS spectrum. This may be somewhat misleading, as there is evidence for a contribution from the dust disk or envelope in the 6-8 μm region in addition to the contribution from the steady accretion disk (see following subsection). The IRS spectrum of V1057 Cyg clearly falls well above the extrapolation of a steady disk model, but this excess is probably due to the envelope or disk regions responsible for the far-infrared excess and silicate emission (see next subsection).

3.4.3 Long-wavelength dust emission and envelopes

Adams et al. (1987) suggested that FU Ori might have a tenuous spheroidal envelope, based in part on IRAS observations. KH91 combined IRAS data with other IR observations to study the longer-wavelength regions in FU Ori objects, with special emphasis on FU Ori, V1057 Cyg, and V1515 Cyg, and found that the infrared spectrum of FU Ori might be fit by a disk without an envelope. KH91 concluded that V1057 Cyg and V1515 Cyg needed to have an additional dusty envelope subtending a significant solid angle, which contributed strongly at wavelengths $\gtrsim 10$ μm. KH91 suggested that this dusty structure represented infalling material which replaced the disk mass accreted in each outburst as a way of obtaining multiple outbursts in the lifetime of each FU Ori object. Further investigations of model envelopes were carried out by Turner et al. (1997). The
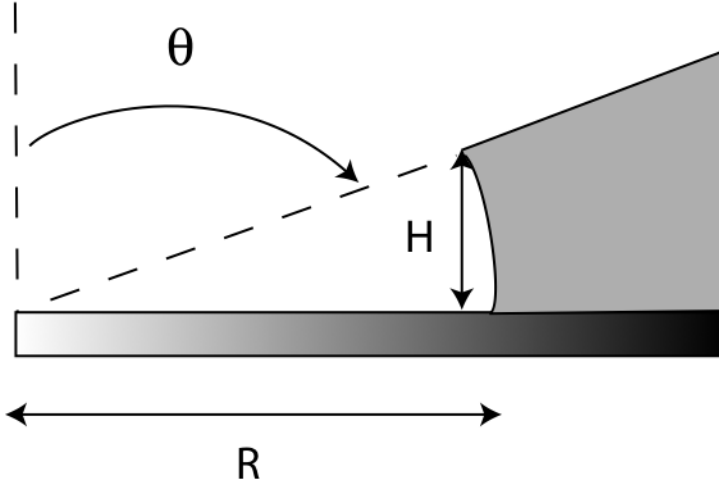
Figure 3.6   Geometry of the simple disk plus envelope model (see text).

IRS data provide an opportunity to reexamine more precisely the question of disk vs. envelope irradiation.

It may not be obvious that an envelope need be invoked, as T Tauri disks can have SEDs that flatten out beyond $\lambda \gtrsim 10$ μm (e.g., Kenyon & Hartmann, 1987; Chiang & Goldreich, 1997; D'Alessio et al., 1999). However, in the case of T Tauri disks, the irradiating source is the star, not the inner disk, and this makes a crucial difference. Consider the geometry shown in Figure 3.6, where for simplicity we have indicated a wedge of material which captures all the radiation emitted at angles $\theta > \theta_m$. In a more realistic disk/envelope combination or a flared disk, this absorbed radiation would be distributed over a wider range of radii, such that the height of the disk or the envelope at R is H. Assuming an isotropically-emitting central source, the fraction of the central luminosity f_* absorbed within R, H is simply the fractional solid angle subtended by the envelope or disk region as seen from the central source (e.g., Hartmann, 1998),

$$f_* = \int_{\theta_m}^{\pi/2} d\theta \sin\theta = \cos\theta_m \, , \tag{3.5}$$

where $\theta_m = \arctan(R/H)$. On the other hand, if the radiating source is a flat disk, even if the emergent intensity is assumed to be isotropic, the emitted *flux* is peaked in the direction perpendicular to the disk, due to the projection of the emitting area in the line of sight. For a geometrically flat disk with luminosity

L_d, the *apparent* luminosity at a viewing angle θ is

$$L(app) = 2L_d \cos\theta \qquad (3.6)$$

Thus, the fraction of the radiation from a flat inner disk, much smaller in radius than R, that can be intercepted by the structure in Figure 3.6 is

$$f_d = \int_{\theta_m}^{\pi/2} d\theta \, 2\cos\theta \sin\theta = \cos^2\theta_m \,. \qquad (3.7)$$

A typical, strongly-flared T Tauri disk might have an aspect ratio of about $H/R = 0.2$ and thus could intercept about 20% of the light from its central star (equation 3.5). On the other hand, the same disk around the flat inner irradiating disk can intercept only about 4% of the inner disk luminosity (equation 3.7). Thus, large long-wavelength excesses due to irradiation by a flat disk require dusty structures which subtend much larger solid angles than would be the case if the central object radiated isotropically.

Thus, unlike a star, the apparent luminosity of a flat disk can be as much as a factor of two larger than its true luminosity if seen pole-on (equation 3.6). In particular, V1515 Cyg and V1057 Cyg have much smaller values of projected rotational velocity, $v\sin i$, than those of FU Ori or BBW 76 (Hartmann & Kenyon, 1985, 1987a,b; Reipurth et al., 2002), which suggests that the former two objects are observed much closer to pole-on. This suggestion is reinforced by the analysis by Goodrich (1987), who argued for similar low viewing inclinations for V1057 Cyg and V1515 Cyg on the basis of outflow envelope morphology. To the extent that the long-wavelength excess is produced in an envelope which emits more isotropically than the inner disk, the envelope will appear to absorb a smaller fraction of the total luminosity in a pole-on system than in reality.

We now consider the case of V1057 Cyg. The disk model shown in Figure 3.4 corresponds to a total flux received at the Earth of $\sim 1.5 \times10^{-8}$ erg cm^{-2} s^{-1}. The total observed flux in the IRS range is about 3.6×10^{-9} erg cm^{-2} s^{-1}. If we assume that all of the flux at 5 μm is due to the accretion disk and not to the dusty structure responsible for the long-wavelength excess, and extrapolate this accretion disk flux as $\nu F_\nu \propto \nu^{4/3}$ to longer wavelengths or lower frequencies, then the excess above this disk emission is about 2×10^{-9} erg cm^{-2} s^{-1}. However, as

discussed above, there is evidence for dust excesses contributing at short wavelengths in V1057 Cyg; in addition, the IRS SED shows no signs of turning down at the longest wavelengths, so we have underestimated the total long-wavelength emission. We adopt $\sim 3 \times 10^{-9} \mathrm{erg\,cm^{-2}\,s^{-1}}$ as an estimate of the total long-wavelength excess; this is 20% of the apparent disk luminosity. Using equation (3.7),

$$\cos(\theta_m) \sim (0.2)^{1/2} \qquad (3.8)$$

or

$$\theta_m \sim 63° \qquad (3.9)$$

so

$$H/R \sim \tan(90 - \theta_m) \sim 0.5 \qquad (3.10)$$

This is a considerably larger aspect ratio than for most known T Tauri disks. In addition, the transition in the height of the absorbing dust structure must be fairly abrupt to explain the SED. We conclude, as did KH91, that there is an additional dusty envelope to explain the far-infrared excess. The true aspect ratio could be even larger if we are viewing V1057 Cyg nearly pole-on and the envelope radiates more isotropically than the inner disk.

At the other extreme, consider FU Ori. Assuming that the accretion disk emission dominates at 5 μm, which seems reasonable, and extrapolating this steady disk spectrum as before, the long-wavelength excess is approximately 2% of the total system luminosity. Even if we assume that all of the flux in the IRS range arises from an excess component, this constitutes no more than 4% of the total luminosity. According to equation (3.7), this excess in principle can be explained by absorption in a modestly flared disk with $H/R \lesssim 0.2$. We therefore reinforce the conclusion of KH91 that the SED of FU Ori can be explained by a flared disk without significant envelope contributions in the IRS wavelength range.

V1515 Cyg has a SED which is quite similar in shape to that of V1057 Cyg (Figure 3.4), but with a bit smaller long-wavelength excess. The excess over the

extrapolation of the steady disk model is about 10%, and the total flux in the IRS range is about 14% of the total luminosity; again, the SED shows no sign of turning down at long wavelengths so there must be significant longer-wavelength flux that we are not including. Adopting an estimated excess of about 12% implies $H/R \sim 0.37$, larger than typical of T Tauri disks. In addition, V1515 Cyg has an extremely low $v \sin i$, implying a very low angle of viewing. As discussed above, this suggests that we are underestimating the relative magnitude of the long-wavelength excess by overestimating the central luminosity, by perhaps as much as a factor of two; this would increase the required H/R even more, similar to that of V1057 Cyg. We therefore conclude that V1515 Cyg must also have a dusty envelope which dominates the long-wavelength infrared emission.

BBW 76 represents an ambiguous case. The shape of its SED is more similar to that of FU Ori than to V1057 Cyg (Figure 3.4), but with a considerably larger excess. The excess above the steady disk model is about 5% of the total luminosity; this is very sensitive to the disk model assumed, as the the total emission in the IRS range is about 10% of the total. If we conservatively estimate a total excess of 6%, then $H/R \sim 0.25$. Thus it is not clear whether some additional, perhaps relatively optically-thin envelope needs to be added to a flared disk to explain the IRS SED.

Bell & Lin (1994), Bell et al. (1995), and Bell et al. (1997) constructed detailed models for FU Ori objects based on specific mechanisms for the outburst and parameters. They pointed out that the inner disk might exhibit departures from purely flat geometry. However, it seems unlikely that this will have a major effect on the above analysis; any regions which have "walls" which are more face-on to the envelope or disk are not likely to be large in extent, and we have neglected limb-darkening, which will reduce the flux at large θ even more than we have assumed. Bell et al. also constructed a number of disk and envelope models to explore the long-wavelength SEDs of FU Ori objects; however, these models have many parameters and it is not entirely clear how to apply their results to our new observations. The above analysis has the virtue of being minimally model-dependent while illustrating the basic geometry.

Our suggestion of envelopes that intercept significant amounts of radiation from the central disk in V1057 Cyg and V1515 Cyg is supported by recent observations in the K-band with the Keck interferometer (Millan-Gabet et al., 2006),

who found that these objects are significantly more extended than predicted by the accretion disk model. Millan-Gabet et al. estimated that their observations could be explained if 3 - 12% of the K-band flux in V1057 Cyg and 5 - 14% of the K flux in V1515 Cyg arises from an extended source that is well-resolved (i.e., bigger than 1 AU or so), as the KH91 envelope model would predict. The approximate amount of K-band excess, on the order of 5-10% of the central source K luminosity, is in reasonable agreement with the intercepted fractions of disk luminosity on the order of 10% derived above, assuming a moderately large ($\sim 0.3 - 0.5$) effective albedo at K. In contrast, FU Ori, which has much less far-infrared excess, shows little sign of being extended at K in interferometric measurements, and matches the predictions of accretion disk models quite well (Malbet et al., 2005).

In estimating the amount of solid angle that the envelope must span from the observed long-wavelength emission, we have included only that emission in the IRS range, i.e. for wavelengths $\leq 35 \ \mu$m. Given that the long-wavelength SEDs of V1057 Cyg and V1515 Cyg are nearly flat, this is clearly an underestimate of the true total excess emission. (We do not use the IRAS fluxes because they very likely include extended, non-envelope emission due to the large beam sizes.) If the SEDs were to remain flat out to $\sim 100 \ \mu$m, as in many Class I sources, the total envelope excesses and thus the inferred solid angle subtended by the envelope could be significantly larger. Longer-wavelength observations, perhaps with MIPS or SOFIA, could help considerably in the characterization of the geometry of the circumstellar dust in these objects.

3.4.4   Envelope model

To explore the possible parameters of remnant envelopes, we explore an approximate calculation and compare it with the observations of V1057 Cyg. The models shown in Figure 3.7 combine a simple steady accretion disk assuming blackbody radiation, plus a flattened envelope with a polar hole in the density distribution, similar to that used in Osorio et al. (2003). The flattened density of the envelope is consistent with gravitational collapse of a sheet beginning in hydrostatic equilibrium as discussed in Hartmann et al. (1994) and Hartmann et al. (1996), referred to as η models. The model parameters include $\eta = R_{outer}/H$, the ratio of the envelope's outer radius to the scale height (Hartmann et al., 1996); ρ_1, the
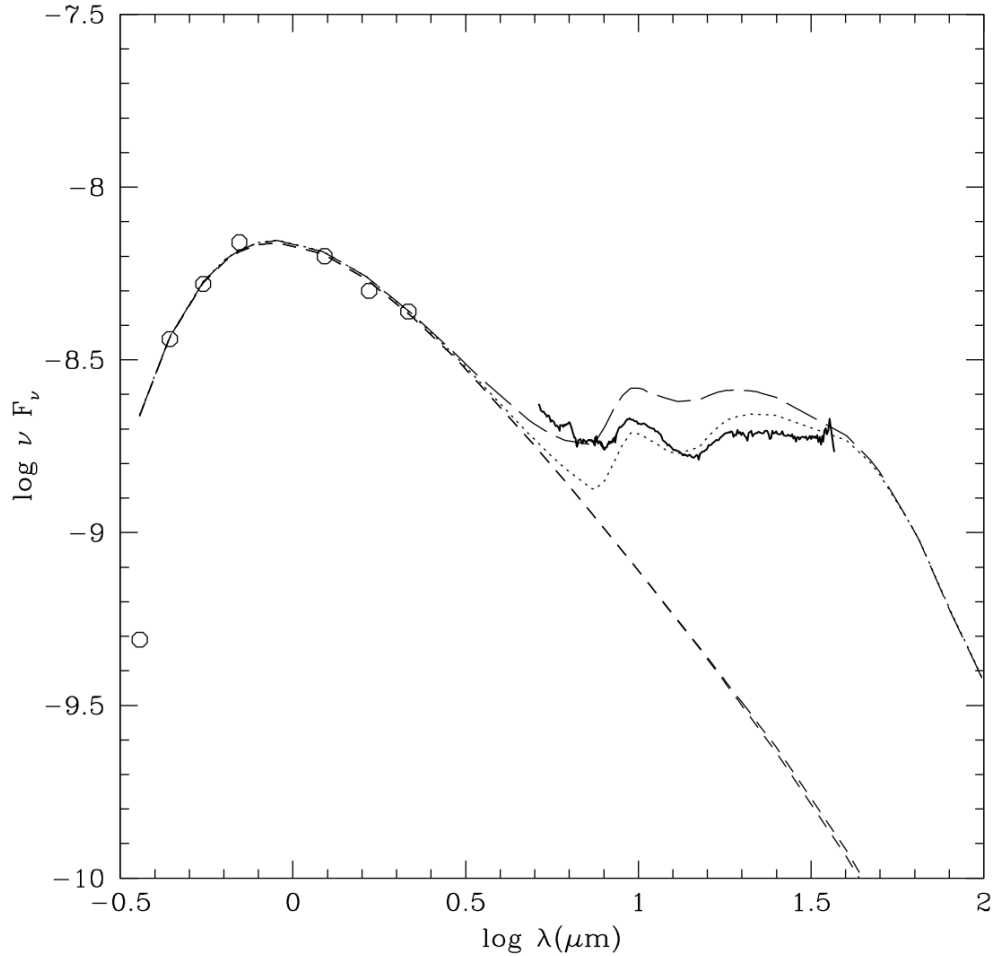
Figure 3.7 Envelope plus steady accretion disk models of V1057 Cyg from Hartmann et al. (1994) and Hartmann et al. (1996). The contribution of the disk alone (a series of annuli of blackbodies at a range of temperatures) is represented by the short dashed curve. The dotted curve shows the fluxes for a model with $\eta = 3.0$, $\rho_1 = 10^{-13} \mathrm{gcm}^{-3}$, $R_c = 20$ AU, $r_2 = 7000$ AU, $r_1 = 5$ AU, and $z_2 = 4000$ AU. This model fits the long-wavelength IRS range reasonably well but has too little flux shortward of 10 μm. The long-dashed curve is for a model in which the envelope is brought closer in ($r_1 = 3$ AU and $R_c = 10$ AU; the other model parameters are identical to the previous case). This model is too bright in most of the IRS range, although it matches the short-wavelength end better.

Table 3.6.   Steady Accretion Model Parameters

Object	d(kpc)	$L/L_\odot$	$T(max)$	$R_i/R_\odot$	$M\dot{M}/(10^{-4}M_\odot^2\mathrm{yr}^{-1})$
FU Ori	0.5	466	7710	5.0	1.5
V1057 Cyg	0.6	170	6590	3.7	0.45
V1515 Cyg	1.0	177	7710	3.1	0.35
BBW 76	1.8	287	7710	3.9	0.72

Note. — Distances are from Hartmann & Kenyon (1996), except for BBW 76, which is taken from Reipurth et al. (2002). Note: if V1057 Cyg and V1515 Cyg are observed pole-on, then the true accretion luminosities may be a factor of up to two smaller, with a reduction of $2^{1/2}$ in the inner radius and a reduction of $2^{3/2}$ in $M\dot{M}$.

density of the infalling envelope at 1 AU given a spherical non-rotating envelope; R_c, the centrifugal radius, the innermost radius on the plane of the disk on which infalling material can be deposited. In addition, we include a polar hole cut out of the density distribution whose boundary is given by

$$z = a(r_2 - r_1),\qquad(3.11)$$

where z is the height above the equatorial plane and r_2 and r_1 are radial distances; r_1 signifies the position where the envelope edge intersects the disk. The system is then viewed at inclination i. A schematic of this model is displayed in Figure 3.8.

In order to calculate the temperature structure of the envelope, we assume radiative equilibrium, using a single central source. We calculate the temperature of each spherical shell using a density averaged over all angles (Kenyon et al., 1993). The luminosity of the central source is given by the steady accretion models in table 3.6. The dust destruction radius is taken to be at $\sim$ 1400 K, corresponding to the sublimation temperature of silicates in a low-density environment (D'Alessio, 1996). The specific intensity at each wavelength is calculated by solving the radiative transfer equation along rays that thread the envelope, using the angle-dependent density distribution, as in Kenyon et al. (1993) and Hartmann et al. (1996). The source function is determined with a mean intensity from the spherical case.

Use of the spherical average radiative equilibrium to determine the tempera-
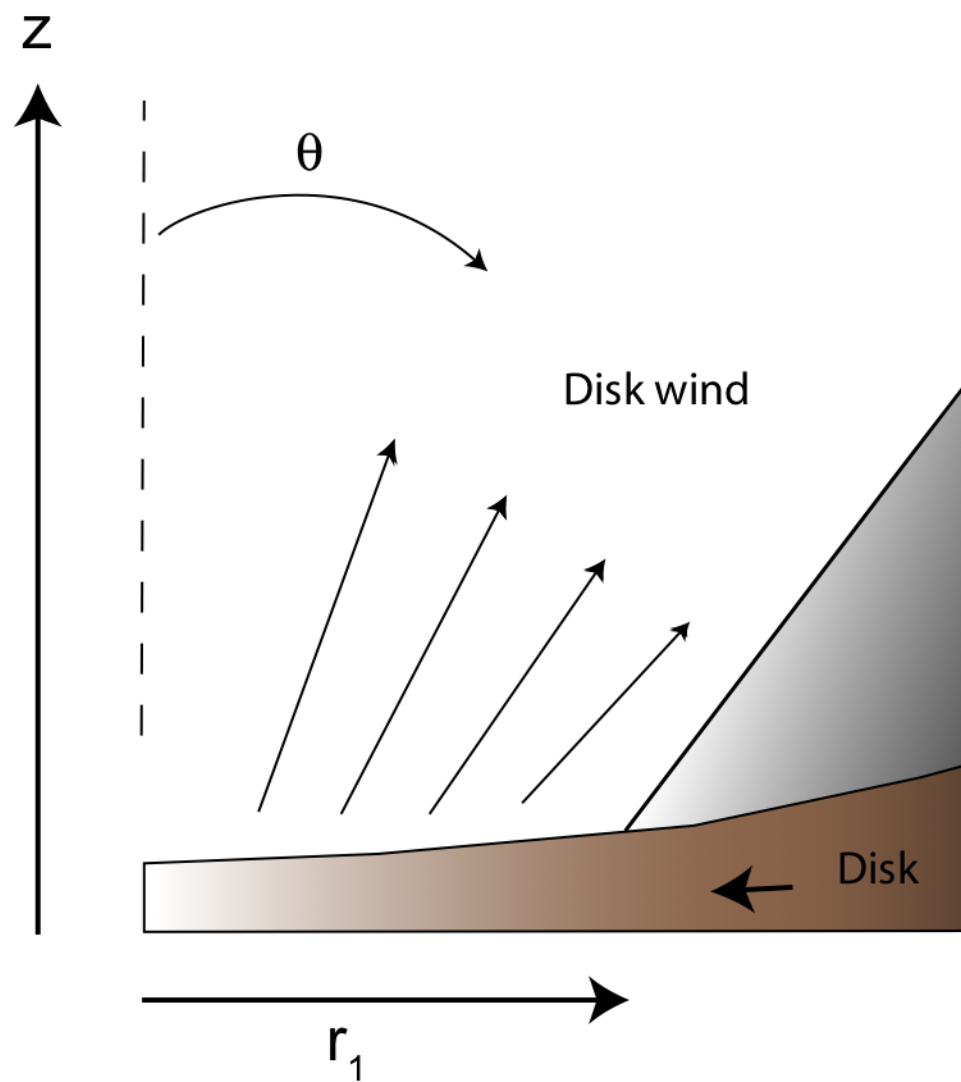
Figure 3.8   A schematic of the steady accretion disk plus envelope model from Figure 3.7.

ture distribution is no longer self-consistent when a (bipolar) hole is present. We adjust the luminosity of the central source in the spherical calculation so that the total luminosity of the envelope integrated over all solid angle is approximately that expected for the particular envelope geometry heated by a flat disk, as discussed in the previous section.

The dust in the envelope uses the standard grain size distribution of the ISM: n(a) α a$^{-3.5}$. The grain radii are between a$_{min}$ = 0.005 μm and a$_{max}$ = 0.3 μm. We use a mixture of dust grains from Pollack et al. (1994), as well as a mixture from Draine & Lee (1984) known as "astronomical silicates." The grains are assumed to be spherical and we calculate their absorption efficiency factor Q_{abs} using Mie scattering code (Wiscombe, 1979). The optical properties of the compounds are taken from Warren (1984), Begemann et al. (1994), and Pollack et al. (1994).

In Figure 3.7 we compare the results of two model envelope calculations to the observations of V1057 Cyg, for $i = 45°$. The short dashed curve indicates the contribution of the steady blackbody accretion disk. This model does a reasonably good job for the long-wavelength IRS range but has too little flux shortward of 10 μm. The long-dashed curve is for a model with the same parameters except for $r_1 = 3$ AU and $R_c = 10$ AU; this model is too bright in most of the IRS range though it matches the short-wavelength end better. We suspect that if we had included the heating of the disk by the envelope (e.g., D'Alessio et al., 1997), the 5 - 8 μm region of the first model would be in much better agreement with the observations.

Given the complexity of the situation, the envelope parameters derived for the envelope are not definitive but merely suggestive that envelope models can account for the long-wavelength IRS fluxes in V1057 Cyg and V1515 Cyg, as suggested by KH91. Further progress on this question will require full two-dimensional axisymmetric radiative transfer calculations. For example, Zhu et al. (2008) pick up on this idea, modeling V1057 Cyg with a cavity-based structure, rather than the somewhat unphysical flattened envelope model, and conclude that the 14/40 μm spectral index can be used to classify FUors into early and late-types.

3.4.5   Envelopes and outbursts

The envelopes we have suggested for V1057 Cyg and V1515 Cyg apparently cover modest solid angles as seen from the central sources. This implies that the (bipolar) outflow holes driven by the winds of these objects have a wide opening angle. Theories of magnetocentrifugally-driven winds from young stellar objects suggest that such winds might have a significant opening angle but have a strong dependence of ram pressure on distance from the rotation axis, such that the jets frequently seen in such objects constitute not the entire flow but merely the densest and most energetic part of a broader flow (e.g., Shu et al., 1995; Matzner & McKee, 1999).

During much of the protostellar phase, the accretion rates are small; since the mass loss rate tends to track the accretion rate (e.g., Calvet, 1998), the outflow is relatively weak in this phase. An FU Ori outburst occurs when the mass accretion rate increases, perhaps by as much as three to four orders of magnitude; in consequence, lower-density, wider-angle portions of the wind can now drive out the infalling envelope. In this picture, it is no surprise that the FU Ori objects have wide-angle envelope holes. V1057 Cyg and V1515 Cyg may be relatively younger, or have had fewer outbursts, than FU Ori and BBW 76, and thus retain envelope material at smaller radii/larger covering solid angles.

Of course, each FU Ori outburst is limited in time so that only a small fraction of a protostellar envelope would be driven off by any given event. The time evolution of the envelope geometry in a situation with repeated outbursts could be quite complicated. In particular, some protostellar sources clearly have narrow outflow holes, which may indicate they have not experienced outbursts, or have particularly large envelope infall rates and thus higher infall ram pressures. The implications of this picture require further exploration.

If infall and outflow were spherical, ram pressure balance would occur for the condition

$$\dot{M}_{wind}\ v_{wind} = \dot{M}_{infall}\ v_{infall}. \qquad (3.12)$$

Consider, for example, V1057 Cyg. KH91 assumed an envelope infall rate of $\sim 4 \times 10^{-6}$ M$_\odot$ yr^{-1} in their envelope model for V1057 Cyg, with an inner radius

of about 7 AU. At that radius, the infall velocity is (for a 0.5 $M_\odot$ central object) ~ 8 km s^{-1}. With a typical wind velocity of order 300 km s^{-1} or more (Croswell et al., 1987), a mass loss rate of $\dot{M} \gtrsim 10^{-7}$ $M_\odot$ yr^{-1} would suffice to blow out the envelope. As the mass loss rates during peak accretion rates should be closer to $10^{-5} - 10^{-6}$ $M_\odot$ yr^{-1}, it is clear that even a relatively small off-axis wind component will suffice to drive out envelope material.

3.5 Conclusions

We have presented IRS spectra of five of the best-known FU Ori objects. One of these sources, V346 Nor, shows ice absorption features and a large mid-IR excess, indicating that it is embedded within a cold icy envelope. The other four program objects are moderately-reddened and show many features in common. In these objects, the IRS spectra provide direct evidence of a gaseous accretion disk through the presence of absorption features, while silicate emission features indicate the presence of outer, cooler dust.

A dusty flared disk probably can explain the long-wavelength dust emission of two of the objects (FU Ori and BBW 76); this suggests that FU Ori events can ignite even as the protostellar envelope is dispersing. Flared disk models have difficulties with accounting for the large excesses longward of 10 microns in V1057 Cyg and V1515 Cyg; instead, we conclude that an outer dusty envelope is necessary to explain the observations, as originally suggested by KH91, and which can provide the extended structure in scattered light detected in near-infrared interferometry by Millan-Gabet et al. (2006). One important feature of the envelope model is that it requires an outflow hole with a large opening angle; we suggest that such a wide outflow-driven cavity is a result of the high mass loss rate accompanying rapid accretion in the FU Ori outburst state. Further near-infrared interferometry with better imaging properties could confirm our picture of the envelopes around V1057 Cyg and V1515 Cyg. This would help support the overall picture of FU Ori outbursts occurring during the late phases of protostellar collapse.

Since the publication of this paper, there has been a larger census taken of IRS spectra of FU Oris, most notably in Zhu et al. (2008) and Quanz et al. (2007).

They pick up on the previous idea of the FU Orionis phase as a transition between embedded and revealed protostellar systems, suggesting that FU Ori events can occur sporadically during the Class I phase as the envelope slowly dissipates. The other possibility is that the FU Ori event actually causes the dissipation of the envelope. This suggests that low mass protostars are capable of dissipating their natal envelopes and blowing them out simply with their outflows. Envelope dissipation was already a problem, as the envelope lifetimes were quite a bit longer than 10^5 yr, particularly in the outer regions where they become stable in distant orbit around the young system. This may explain how envelopes are unbound and allow the protostar to reach the next stage of development.

If a *low mass* protostar can generate an episodic burst of ejecta and blow off its envelope, then what are the implications for *higher mass* protostars? If higher mass protostars maintain a steady flow that exceeds the outflow rate of a low mass FU Ori object, then we would expect that the continuous outflow would dissipate an envelope almost immediately. Furthermore a flow capable of dissipating an envelope should be able to shock the medium as it punches through, creating a giant wide-angle cavity in the surrounding cloud over considerable distances. What would something like this look like when observed in the infrared? In the next chapter we consider the somewhat more continuous of intermediate-mass protostars, and their stirring and disruptive effects on molecular clouds.

4 Chasing Interstellar Shockwaves with Spitzer-IRS

4.1 Introduction

4.1.1 The Consequences and Causes of Protostellar Accretion

Anisotropic outflows and shocks are associated with young stars of all masses, during their earliest phases of development when their accretion rates are sufficiently high, ie. $\gtrsim 10^{-7}$ $M_\odot$ yr^{-1}. In the standard picture of star formation, a small part of a cloud composed primarily of molecular hydrogen is compressed, slowly collapsing on itself, coalescing into a dense clump of material heated by the collapse to high temperatures. This central clump photodissociates (ionizes and dissipates) the gas and forms a cavity around itself, creating a thermal pocket of high energy in the cloud. This ball of gas collapses over about 10^4 yr to form a protostar surrounded by an envelope of colder gas. The infalling material rotates more quickly as it spirals inward, conserving its angular momentum. While the star is still growing to its final mass, much of the surrounding material flattens into an annular shape that rotates about the central protostar. If all of the angular momentum from the disk were transferred to the protostar, it would spin so quickly that much of its material would be ejected. Instead, the star releases much of the excess angular momentum through a dramatic mechanism, firing off symmetric bipolar jets into the ambient medium and out of the photodissociation region, raking the cloud with a collimated compression shockwave in much the same way that a speeding boat creates wake in the ocean. As the protostar evolves, more of the mass from the surrounding envelope falls onto the central

protostar – although a considerable amount will remain in the circumstellar disk for a much longer timescale – but the depleted envelope remains optically thick and veils the system; the SEDs of these systems correspond to Class I sources. Eventually the envelope clears from around the star via accretion onto the star or the disk (or perhaps dispersed by powerful winds from the protostar when the envelope density becomes sufficiently low), and the disk dust grains collide and accrete to form larger grains and crystalline structures, slowly building into planetesimals. After the envelope is gone, the now isolated central protostar has neared its final mass, and the disk remains optically thick, the system is referred to as Class II, and the bipolar outflows are generally not observed around these objects, although occasionally extended emission may be attributed to them.

Accreting stars of all masses exhibit bipolar outflows. Truly massive (greater than 15 $M_\odot$) stars can trigger chains of star formation during their dying stages, releasing their energy in vast explosions. Very low mass stars may rake their local environment with high velocity flows, but they are heavily embedded and may have minimal cloud-wide impact. Intermediate mass stars are an interesting case; is there a feedback loop of star formation and ejecta? How much impact do young stars have on shaping their natal clouds, or in dissipating them? The shock picture was pieced together by Draine (1980), who envisioned three types of shocks: those in which the magnetic field from the shocked ions is either frozen into the shock, or is non-existent; J-type shocks with magnetic precursors (or radiative precursors), in which the neutral fluid undergoes a discontinuous "jump" in density and temperature; and C-type shocks in which the fluid changes continuously over the shock boundary. The signatures of these shocks can be disentangled by observations of the transitions of the excited species. C-type shocks ($\lesssim$ 45 km/s) excite the molecules of the medium but do not significantly alter the chemistry, whereas fast J-type shocks can utterly disrupt them. We want to determine how much of interstellar chemistry is affected by the proximity of star clusters, and many of the most crucial diagnostics of these interactions are in the mid-infrared. The Spitzer Space Telescope allows us to peek into these regions with unprecedented sensitivity and provides a wide range of constraints.

Roughly 5% of T-Tauri stars exhibit P-Cygni profiles, with a redshifted absorption trough indicating mass outflow. Another $\sim$ 5% exhibit inverse P-Cygni profiles, with a blueshifted absorption indicating mass infall (Lada, 1985). Ob-

servations of optically thin ^{13}CO indicate the presence of high velocity, poorly collimated molecular flows around young stellar objects, encompassing $\sim$ 1 - 100 $M_\odot$ of material, at 10-90 K, at a density of n $\sim$ 300-3000 cm^{-3}. As mentioned in the previous chapter, it is quite common for young stars to undergo energetic mass ejection through massive bipolar outflows driven by strong stellar winds. The launching mechanisms are less well-understood; one possibility is that the material is lifted from the disk on twisting magnetic fields lines, exchanging angular momentum with the star and accelerated through the poloidal magnetic field lines into the ambient medium.

It is not known whether these collimated jets originate near the pole of the star, or are launched from somewhere on the disk itself. In fact both mechanisms may be at work, as outflows exhibit widely varying degrees of collimation, and the collimation factor of the emitted jets is much higher than the surrounding outflow. Particles might reach the edge of the circumstellar disk and ride along the field lines up toward the poles of the system. All models of jet launching are magnetocentrifugal, but use different footpoints for launch. One possibility is a photoevaporative disk outflow (e.g. Hollenbach et al., 1994), particularly in the case of high bolometric luminosity. Another model involves a line-driven wind from the inner-disk surface (Drew et al., 1998). Thermal energy released at the disk/star boundary could efficiently release kinetic energy in the form of outflows (Torbett, 1984; Soker & Regev, 2003). Another model is the "X-Wind" theory (Shu et al., 2000; Shang et al., 2007, and references therein). Whatever the source of the magnetic field, it is necessary to anchor the field lines and use the twist to launch material in a collimated outflow. Part of the difficulty in modeling the outflow as a single process is the difficulty in accreting particles onto the star at all. It is beyond the scope of this work to discuss solutions to this theoretical problem; for the purposes of this work we assume that protostars drive bipolar outflows with high ($\sim$ a few hundreds of km/s) and low ($\sim$ a few tens of km/s) velocity components which cause shocks to radiate throughout the parent cloud, potentially providing clues to the power of the shock, and to the shocked environment itself. Furthermore these outflows can drive off or at least penetrate portions of the surrounding envelope and environs, creating a cavity in the cloud around the spinning protostar. If the launching mechanism is precessing about an axis, the cavity may become quite wide.

Infall is an unsteady process at any stage; much of the material may rain down onto the protoplanetary disk in sudden bursts, triggering disk accretion shocks. Watson et al. (2007) observed with Spitzer-IRS over 70 transitions of H_2O, OH, and $H_2^{18}O$ emitted from the Class 0 source NGC 1333-IRAS 4B, at a molecular hydrogen density $n(H_2) \sim 10^{12-13}$ cm^{-3}. As typical outflow densities are observed to be $n(H_2) \sim 10^{4-5}$ cm^{-3}, the nature of this observed shock is quite different: a shock from icy grain mantles vaporizing upon contact with the accretion disk.

If we consider the measured flow rates for infall and outflow, we find something unexpected. The infall rate for this source has been estimated as 3.5×10^{-5} $M_\odot$ yr^{-1} (Di Francesco et al., 2001) or 10^{-4} $M_\odot$ yr^{-1} (Maret et al., 2002). The envelope to disk accretion rate 0.7×10^{-4} $M_\odot$ yr^{-1}. The outflow rate is 2×10^{-6} $M_\odot$ yr^{-1}. The absolute upper limit for accretion onto the protostar, assuming that the luminosity of IRAS 4B (~ 4.2 $L_\odot$) was entirely due to accretion, is $\sim 10^{-6}$ $M_\odot$ yr^{-1}. The infall rate derived is $\sim 10^{-4}$ $M_\odot$ yr^{-1}, assuming that the protostar is very favorable to accretion. Thus most of the infalling material is not landing on the protostar, or being ejected via an outflow; this suggests that gas may be building up in the disk, soon to trigger an FU Orionis event in the system.

This phenomenon was observed in 1 out of 30 Class 0 sources, suggesting that, without accounting for the large effect of source inclination angle, $\sim 10\%$ of the Class 0 phase is spent in high accretion events. Such episodic accretion also occurs with similar frequency in Class I and II sources in the form of FU Orionis events (see Ch. 3). FUors are responsible for 5-10% of the accretion within 1 kpc (Herbig, 1977; Hartmann & Kenyon, 1996). Outflow models suggest the ejection of material varies directly with the infall rate through the disk. Thus if accretion is episodic – and we assume that disk accretion translates directly into accretion onto the central protostar – we might expect outflows and jets to be episodic and ejection rates to vary by $\sim 100\times$ or more. The validity of the assumption that the accretion flow and outflow rate are perfectly correlated has not been established, but objects similar to NGC 1333-IRAS 4B provide a unique opportunity to check this, utilitizing Spitzer-IRS observations of the disk accretion shock and outflow, in addition to high-resolution submillimeter imaging (using instruments like SMA) of the extended flow.

We can observe outflows from young protostellar systems only through the heavy veil of extinguishing gas and dust that surrounds them. In many cases this

will obscure both the accretion flare and the outflow from view. However, if we are fortunate enough to view the protostar at a near pole-on inclination angle, the outflow may create a cavity in the envelope by which we can view the inner disk. Additionally we can track the progress of the outflow as it pushes through the surrounding environment.

4.1.2 The Natural Environment of Protostars

Giant molecular clouds are reservoirs of cold material for star formation, shielded from the radiation of the interstellar medium, first discovered in the infrared in 1968. They contain $\sim 10^{4-6}$ M$_\odot$ of material and range from 1-100 parsecs in size, with the material typically at temperatures ~ 10 K. The sound speed in molecular clouds is a few $\times$ 0.1 km s^{-1}, but the measured FWHM of the ^{12}CO emission lines measured in these clouds ~ 1 - 3 km s^{-1}; this indicates supersonic bulk motion. The wings of the ^{12}CO emission indicate velocities in excess of 150 km s^{-1}; columns of rapidly moving material are filtering through and interacting with the cloud material. The motions in CO indicate the interaction between young stars and the cloud, which power turbulence in these regions (Quillen et al., 2005).

Outflows from young stellar objects, while not as energetic as supernovae or photoionization, are far more common and may play a significant role in stirring up the molecular cloud material. A typical YSO outflow represents $\sim 10^{43-47}$ erg, compared to $\sim 10^{51}$ erg from a Type II supernova. Shocks are pressure waves that effect an irreversible change upon the medium as they pass through. It is not well understood whether the passage of these shocks causes material to clump further, enhancing the possibilities for star formation (particularly of the low-mass variety) or causes material to scatter and dissociate, suppressing star formation. Population density studies of young stellar objects in nearby molecular clouds suggest that there is somewhat less clumping than we might expect (Gutermuth et al., 2008) if star formation tended to feed further star formation, but we can also answer this by studying the effects on the ambient medium directly. Although we can observe the extent of cloud in CO, the composition of the cloud is difficult to determine directly, as most of the species are optically thick and normally veiled from our view. It is the passage of interstellar shocks that illuminate the cloud interior and reveal much more of the composition, and using spectroscopic

mapping techniques we can study both pre- and post-shock material in various molecular and excited ionic species to give some insight into the dynamics of stellar nurseries.

Young stellar objects are generally linked to material outflow that manifests in several ways: Herbig-Haro objects at optical wavelengths, high-velocity water maser sources, optically visible tightly-collimated jets emitted directly from the polar regions, and shock excited molecular hydrogen and fine structure emission regions (particularly at infrared wavelengths) and cold, poorly collimated, extended molecular flows (Bachiller, 1996).

A general picture of shock excitation is as follows (see Figure 4.1 for a simple cartoon picture). Material ejected from the driving source passes through the cavity created in the surrounding envelope. The material travels supersonically in a collimated jet and collides with slower moving material (including gas previously ejected by the source and slowed by the ambient medium at earlier stages) within the molecular cloud. The interactions occur both at the front of the jet as it rams through the medium, and at the edges, where shear forces may spark smaller shocks, producing a structure that resembles the wake of a ship, known as a bow shock. It is easiest to consider what happens from the reference frame of the jet material, which sees two different shocks: a forward shock, in which the front end of the jet rams into the surrounding medium and causes it to accelerate (known as the terminal working surface), and a reverse shock, in which material more recently ejected from the driving source collides with the slower moving material at the head of the jet (known as the internal working surface) (Draine & McKee, 1993). Additionally, material from the jet may move at different speeds (if the Alfven speed of the postshock gas is greater than the speed of the shock itself) , or emit photons that impact material before the shock arrives, in which case a third precursor region forms ahead of the terminal working surface. The signature of these different effects is directly observable in the mid-infrared, fully utilizing the tools provided by instruments like the IRS.

Shock velocities typically reach a few $\times$ 10 km s^{-1}; wind-driven flow velocities can exceed a few $\times$ 100 km s^{-1}, and trails of bow shocks are frequently observed in star forming regions across the sky. Additionally the outflows are marked by "bullets", areas of much higher density (Bachiller, 1996). These could reflect either a change in the ambient medium (a local density fluctuation) or a change in the
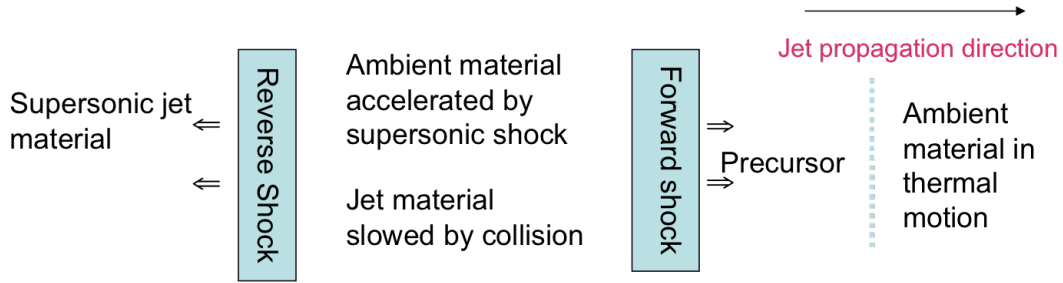
Figure 4.1 A cartoon of a two-shock model, including a J-shock and a non-dissociative C-shock.

outflow; the later case is suggested by the episodic nature of accretion in driving sources like FU Orionis objects. Timescales observed between bullets are comparable to estimated statistics of semi-periodic FU Orionis outbursts. Additionally, when combined with precision velocity measurements, assuming periodicity allows one to calculate precession rates in the driving source itself (Cunningham, 2006).

4.1.3   Cepheus A

Herbig Haro objects are small emission nebulae that signify the interaction between both broad and collimated outflows from YSOs and the ambient molecular cloud material. At 700 pc distant, the region Cepheus A contains some of the best observed Herbig Haro objects. Cepheus A consists of at least two broadly extended CO outflows, Cepheus A East and Cepheus A West (Hughes & Wouterloot, 1982); sometimes referred to as HH 168 (Reipurth & Raga, 1999). Both flows have been mapped by Spitzer-IRS, and are discussed in detail in Sonnentrucker et al. (2006). I will only briefly touch on some interesting facets of Cep A East here, noting its intertwined nature with Cep A West. The Cepheus A East-West complex is shown in Figure 4.2.

Cepheus A appears to have at least two bipolar outflows centered roughly at the same location, in the vicinity of a source known as HW2, a 15 $M_\odot$ protostar. Cep A West appears to be accelerating away from the core of the molecular cloud, while the Cep A East outflow exhibits evidence for a turbulent flow (Rodríguez et al., 2005). Curiel et al. (2002) noted an arc of water maser activity extending from HW2, and they suggest that the exciting source is a cluster of protostars, or alternately an expanding HII region. Additionally, HW2 has powerful colli-

mated bipolar jets. Interestingly, a number of the HH objects in Cep A East (to the northeast of HW2) can be convincingly explained as originating from HW2, despite having different orientations. The distance to these HH clumps seems semi-periodic, and the difference in orientation can be explained if the launching mechanism from HW2 is in fact a precessing disk, torqued by an unseen binary companion. Near-IR observations of molecular hydrogen around HW2 suggest that it has rotated ~ 45 degrees in the last 10,000 years (Cunningham, 2006; Hiriart et al., 2004). Additionally, Sonnentrucker et al. (2006) observed CO_2 ice absorption from the protostar HW2, fairly typical for a Class 0/I protostar.

The triaxial nature of the molecular outflows in the region suggest that they spring from more than one source. To the south of HW2 lies a 10 $M_\odot$ protostar known as HW3c, suggested as the source of the flow in Cepheus A West (GGD 37), specifically HH 168 (Cunningham, 2006; Rodríguez et al., 2005). They posit that HW2 may be driving the extremely high velocity molecular flow with a more northeasterly orientation, and the corresponding southerly flow may be lost to extinction in the region, while HW3c is driving both the western and the eastern flows. As for HH 168 and GGD 37, while the orientation of several of bow shocks in GGD37 point toward a launch from the vicinity of HW3c, the evidence is inconsistent. First, several of the bow shocks appear to be angled away from a source near the southeastern corner of the flow. Second, a chain of several extremely high proper motion knots of [Fe II] 1.644 μm emission connects the southeastern flow (Raines, 2000). Here we provide additional evidence that another source is driving the HH 168 train: the radio source W2[1] at the base of the GGD 37 flow, as originally suggested by Bally & Lane (1991). The question of the driving source is most simply settled with high-resolution velocity gradient measurements, but with *Spitzer* we have a group of diagnostics that can shed some light on the nature of the flow.

The region has been mapped in both hard and soft x-rays (Pravdo & Tsuboi, 2005). Both HW2 and HW3c are detected in hard x-rays, while HH 168 (including the W1-W2-W3 region) is detected in soft x-rays (indeed there is a suggestion of a SE-NW flow as well). They note two distinct soft x-ray sources within HH 168 flow, one near the W2 region, and one at the far end of the flow. They conclude

---

[1]Nomenclature from Garay et al. (1996)

that the HH 168 flow luminosity is 1.1×10^{29} erg/s, and infer a shock velocity of 620 km/s, and a temperature of 4×10^6 K from comparisons to L1551 IRS 5 / HH 154 (Favata et al., 2002; Bally et al., 2003). They observe that the flow is extreme in temperature, although not in luminosity. The x-ray observations are both underluminous by comparison to the radio flux, and offset from both the optical and radio observations, and they conclude this is due to the complex morphology of the region and multiple driving sources, as well as anisotropy in the medium. In this chapter we will propose that the offset and extended nature of the soft x-ray emission is directly tied to the cloud shock.

The outflow region GGD37 (Gyulbudaghian et al., 1978, Cepheus A West) is suspected to be an amalgamation of at least two superimposed flows (Raines, 2000), traveling in different directions on the sky. C-shocks excite the molecular hydrogen into various rotational states detectable at IRS wavelengths, while strong shocks completely destroy the molecules and illuminate the ions. A few lines of [Fe II] and molecular hydrogen are detectable from the ground at H and K-band and have been mapped. *Spitzer* enabled us to gather information on a number of higher excitation species, and place stronger constraints on the flows. The spatial information of these bands placed constraints on the temperatures in those regions where they dominate and allowed us to differentiate between the two flows chemically.

4.1.4 Methods

We can derive independent measures of the gas flow density and temperature that results from the interaction of the jet (whatever its driving source) using the toolbox of diagnostics provided by Spitzer-IRS. The spectrograph allows us to measure the energy output of the region at every wavelength, and therefore the density of photons at every energy, at every point in the map, for each chemical species and each vibrational mode that emits between 5.3 and 38 μm.

In the case where there is no vibration we observe the S-branch. The S(0) - S(7) transitions represent the eight lowest pure rotational states for hydrogen molecules – transitions of $\Delta J = -2$, while the Q and O branches do not appear in the emission spectrum as long as $\Delta v = 0$. Thus for example the S(3) line represents the $\Delta v = 0$, $J = 5 \rightarrow 3$ line (at 9.67 μm). Odd J states represent
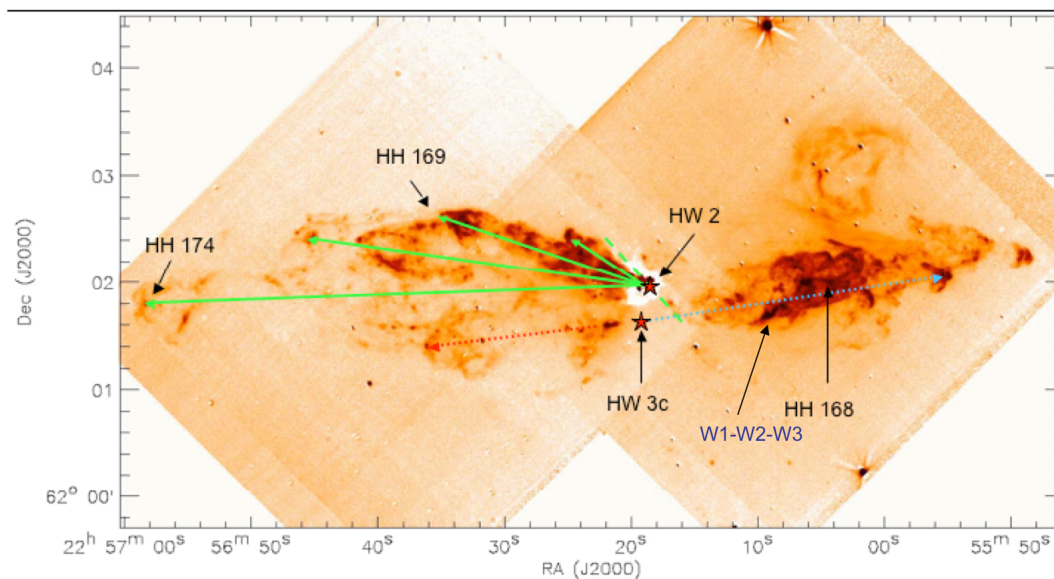
Figure 4.2 Near-IR H_2 image of Cepheus A (Bally & Lane, 1991). Overlaid
are suggested directions for separate jet launches, suggesting that many of the
flows in Cep A East are from the slowly precessing HW2 system, while HH 168
appears to be shocked from somewhere in the direction of HW3c. We propose
that W2 may in fact be the sole driving source.

triplet spin states (ortho-H_2) in that their spin wavefunctions change sign when the nuclei are reversed, and even J states conversely represent singlet spin states (para-H_2); there are three potential odd J configurations for every even J state. The mid-IR lines dominate the hydrogen emission at lower temperatures ~ 500 K, where as the near-IR lines such as those seen in the images in Raines (2000) (e.g. v $= 1 \to 0$, J $= 3 \to 1$ and J $= 2 \to 0$ in K-band imaging) are much stronger at 2000 K.

In addition to ro-vibrational spectroscopy, we can detect ionizing radiation from the metallic components of the cloud. When an electron jumps to another energy state around its atomic nucleus, whether spontaneously or stimulated by a colliding photon or particle, the atom will emit a photon equal in energy to the potential of the transition:

$$E_2 - E_1 = h\nu \tag{4.1}$$

Thus the photons from a particular transition will line up at a specific frequency or wavelength and create a large spike in the spectral energy distribution (SED). Spectral line observations are records of the distribution and frequency of the transitions of electrons from one energy state to another around the atomic nucleus. In thermal equilibrium the excitation of electrons (due to photon absorption or other causes) will balance out the de-excitation and the temperature will remain constant. When a shock compresses the medium it causes heating and irradiation of photons that disturbs the equilbrium, and we observe cooling behavior in its aftermath through these spectral lines.

In this chapter we consider two main de-excitation mechanisms. Spontaneous emission is characterized by the Einstein A-coefficient (the probability per unit time that an electron will jump from upper state 2 to lower state 1). In the case that the excitation is subthermal (ie. the density is low enough that collisional de-excitation of the upper level is negligible), the fraction of population in each state is

$$f_2 = \frac{n_0}{A_{21}} \sum_{j>i} \gamma_{01} \tag{4.2}$$

where γ_{01} is the collisional rate coefficient to state 1 from the ground state,

and the summation is over all states that can join the population of state 2.

At higher densities the states are thermally populated:

$$f_2 = \frac{g_2 \; exp(-E_2/kT)}{\sum_1 g_1 \; exp(-E/kT)} \tag{4.3}$$

Thus spectral lines are powerful diagnostics of temperature and density of the local gas, and can be used to measure the effects of the shock. Furthermore as these two techniques have independent excitation mechanisms, we can probe different energy regimes of the gas to see if there are fundamental morphological differences. We have an entire suite of energies (and therefore temperatures and density regimes) that we can probe using mid-IR spectra from Spitzer-IRS, as we will see.

Two Different Diagnostics

We use two different techniques to analyze the spectral lines in our spectra. The first is the LTE (local thermodynamic equilibrium) treatment for the H_2 rotational lines; the second is a multi-level excitation for [Fe II] and [S III]. Molecular hydrogen is excited by collisions with molecular hydrogen, while [Fe II] and [S III] are excited by collisions with electrons, and are thermally populated at these densities; H_2 is a good probe of temperature and extinction. All of the detections of [Fe II] fine structure lines in the mid-IR are optically thin, as the states are not fully populated to have reached thermodynamic equilibrium, and are not fully populated thermally; these make good probes of density. However we can use this to work backward to the density and temperature of the ions by fitting models to the line fluxes.

Kirchoff's law relates macroscopic emission to absorption if the system can be considered in thermodynamic equilibrium; the Einstein coeffiicients extend this relationship to the molecular and atomic level. The A-coefficient represents the transition probability from one to state to another per unit time from spontaneous emission (when an electron drops from an excited state to a lower state), while the B- coefficient represents the absorption/excitation probability. The number of transitions out of a given state must equal the number of transitions into that state – in other words, the distribution of ions amongst the fine structure levels is

determined by the assumption of steady state under collisional excitation – and we can derive probabilities for excitation and de-excitation:

$$n_1/n_2 = \frac{\gamma_{12}}{\gamma_{21}} = \frac{g_1}{g_2} exp\frac{hc}{\lambda_1 kT} \tag{4.4}$$

and

$$\gamma_{21} = \frac{h^2}{(2\pi m_e)^{\frac{3}{2}} k^{\frac{1}{2}}} \frac{\Omega_{21}}{g_2 T^{\frac{1}{2}}} \tag{4.5}$$

where n_1 and n_2 are the number densities of the states, γ_{12} is the collisional excitation probability from state 1 to state 2, γ_{21} is the de-excitation probability, g_1 and g_2 are the statistical weighting of population distribution for the states – where $g_j = 2J+1$, the degeneracy of the state j – and Ω_{21} is the form for the collision strength using a polynomial fit presented by Pradhan & Zhang (1993):

$$\Omega = \omega_0 + \omega_1 T + \omega_2 T^2 \tag{4.6}$$

We can thus derive the energy level population fraction from balancing the emission and absorption components:

$$B_{jj} = \sum_i n_e \gamma_{ij} + A_{ij} \tag{4.7}$$

$$D_{ij} = B_{ij} - n_e \gamma_{ij} - A_{ij} \tag{4.8}$$

and the fraction as a function of state is given as

$$f = D^{-1}E \tag{4.9}$$

where E is the normalized initial condition. We calculate the emission coefficient:

$$\epsilon_{ij} = \frac{hc}{4\pi \lambda_{ij}} A_{ij} f_j \tag{4.10}$$

We then fit our two- or three-component models – temperature (T), electron density (n_e), and later extinction(A_V) from an interpolated Mathis law ($R_V = 3.1$) and generate a fit to the state population ratios (which are proportional to the observed flux), as equivalent widths of optically thin lines are proportional to column densities in the lower state of the transitions. A Grotrian diagram showing the relationship between the mid-IR [Fe II] lines is shown in Figure 4.3.

In the case of [S III], for which we have a pair of lines, if we assume only the lowest three states are populated we can solve for the number density analytically (e.g. Watson, 1985):

$$n_e = \frac{\gamma_{01}(A_{21} + A_{20}) + \gamma_{02}(A_{21} + (R/a)A_{10})}{\gamma_{01}(R/a)\gamma_{12} - \gamma_{21} - \gamma_{20}) + \gamma_{02}((R/a)(\gamma_{12} + \gamma_{10}) - \gamma_{21})} \tag{4.11}$$

where the two transitions are $2 \rightarrow 1$ (higher; in this case 18.7 μm) and $1 \rightarrow 0$ (lower; in this case 33.4 μm), R is the ratio of the intensities of the two lines I_{10}/ I_{21}, A_{xy} are the Einstein A-coefficients for spontaneous emission, γ_{xy} are the probabilities of de-excitation or excitation (Greenberg et al., 1977; Pottasch et al., 1984), and a = $\lambda_{21}A_{10}/\lambda_{10}A_{21}$.

We make the additional assumption that the A-coefficients $A_{0\rightarrow2}$ and $A_{2\rightarrow0}$ are ~ 0. This will provide us with a density value for the highest temperature gas in the shock.

4.2   Highlights of the GGD37 Dataset

The data reduction procedure is described in detail in Chapter 2 of this work; our observation log is found in Table 4.1.

Here we publish our datacube (Figures 4.5, 4.6, 4.7, 4.8, 4.9, 4.10, 4.11, 4.12) and show all line maps and selected continuum plots (Figures 4.19, 4.20, 4.21, 4.22). All images are plotted in right ascension (RA) vs. declination (Dec) in units of arcseconds from the centroid of the westernmost mapping AOR grid – the coordinates of the center point are RA $\bar{3}$43.99455 and Dec $\bar{6}$2.032823 (in decimal degrees). All detected lines are listed in Table 4.2. Although we truncate our LH spectra at 36 μm due to data artifacts at the long wavelength edge of of the array,
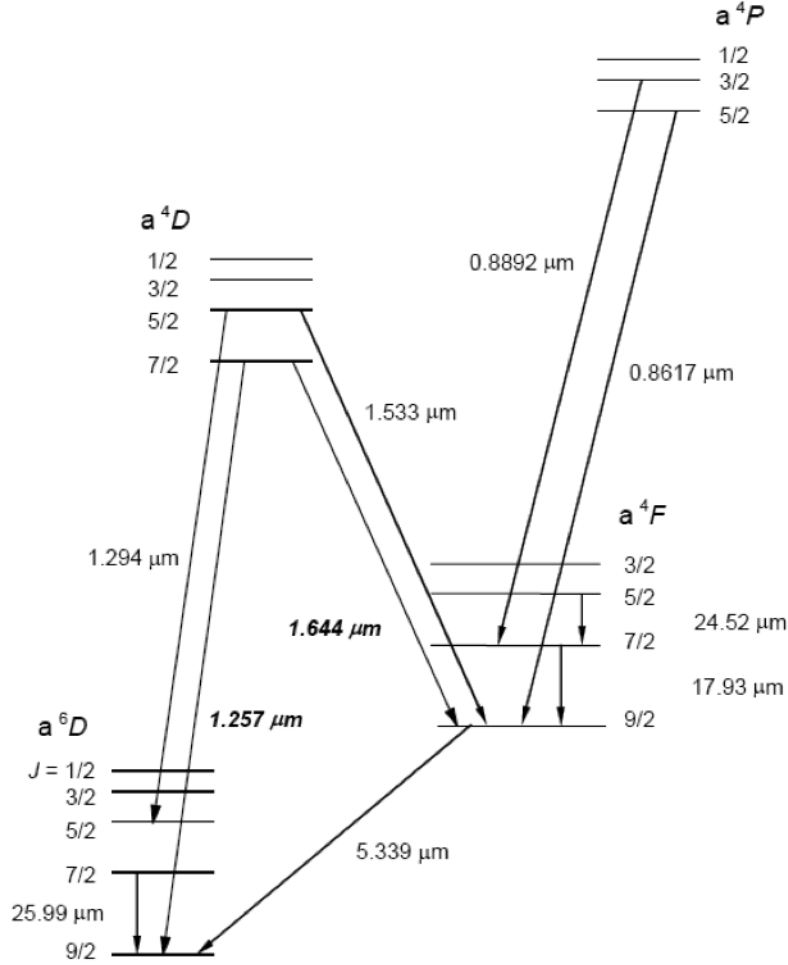
Figure 1: The four lowest-energy multiplets of Fe⁺, not drawn to scale. Several strong forbidden transitions – each accounting for more than 4% of the total [Fe II] intensity in the spectra shown in Figure 3– are indicated on the diagram; the two lines we observe most frequently, at 1.257 μm and 1.644 μm, are labeled in bold italics.

Figure 4.3   Grotrian diagram of the five [Fe II] transitions at IRS wavelengths.

Table 4.1.   Observations Log of GGD 37

AOR	Modules	Observation Date	Data SSC Pipeline Version
5005312	SH/LH	2004-08-10	S12.0
5005568	SH/LH	2004-01-07	S12.0
17856768	SL/LH	2007-08-30	S15.3/S17.2
17857536	SL/LH	2007-08-29	S15.3/S17.2
17857792	LH	2007-09-04	S15.3/S17.2
17858048	LH	2007-08-29	S15.3/S17.2
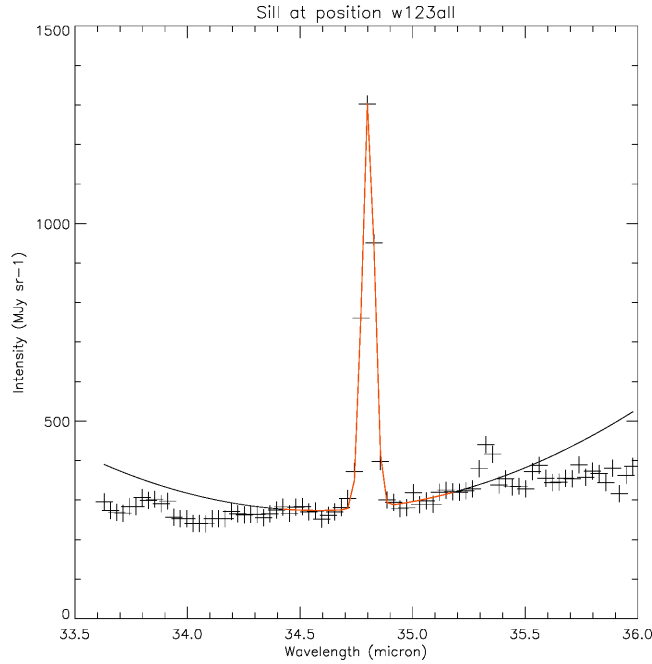
Figure 4.4 Example of a fit to a detected line, [Si II].

it should be noted that we expect no fine structure or rotational lines to appear at those wavelengths. Additionally we republish high-resolution H-band images of H_2 and [Fe II] from Raines (2000).

4.2.1 H_2 Emission

As in Neufeld et al. (2006b) and in Maret et al. (2009) we fitted a two-temperature model to the rotational diagrams (Table 4.5) based on a simple local thermodynamic equilibrium (LTE) treatment, with results similar to those obtained for the outflows in the previous paper, suggesting nondissociative C-type shocks of 10-20
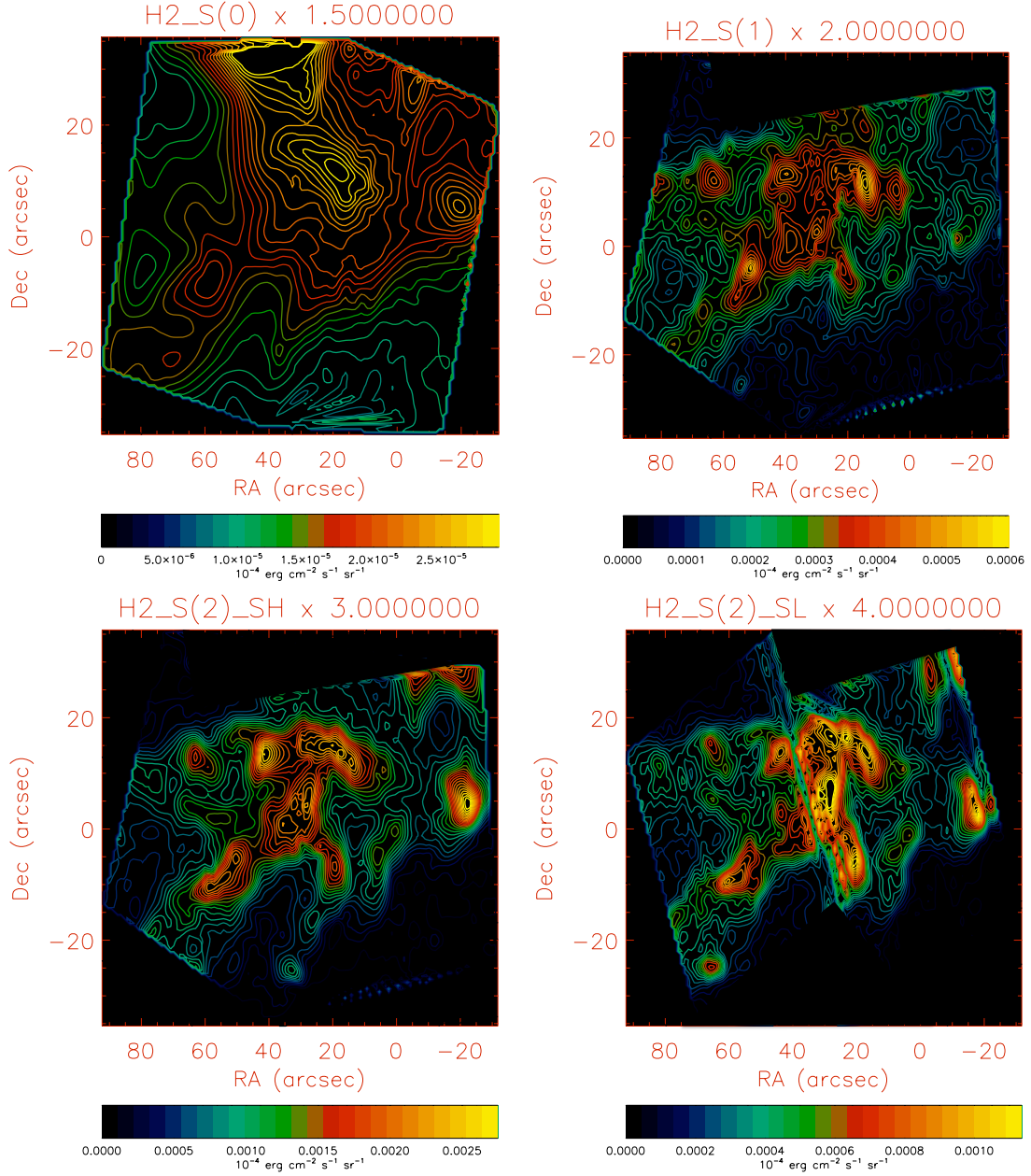
Figure 4.5 Intensity contour maps of all the detected lines and selected continuum maps and solid state feature maps.
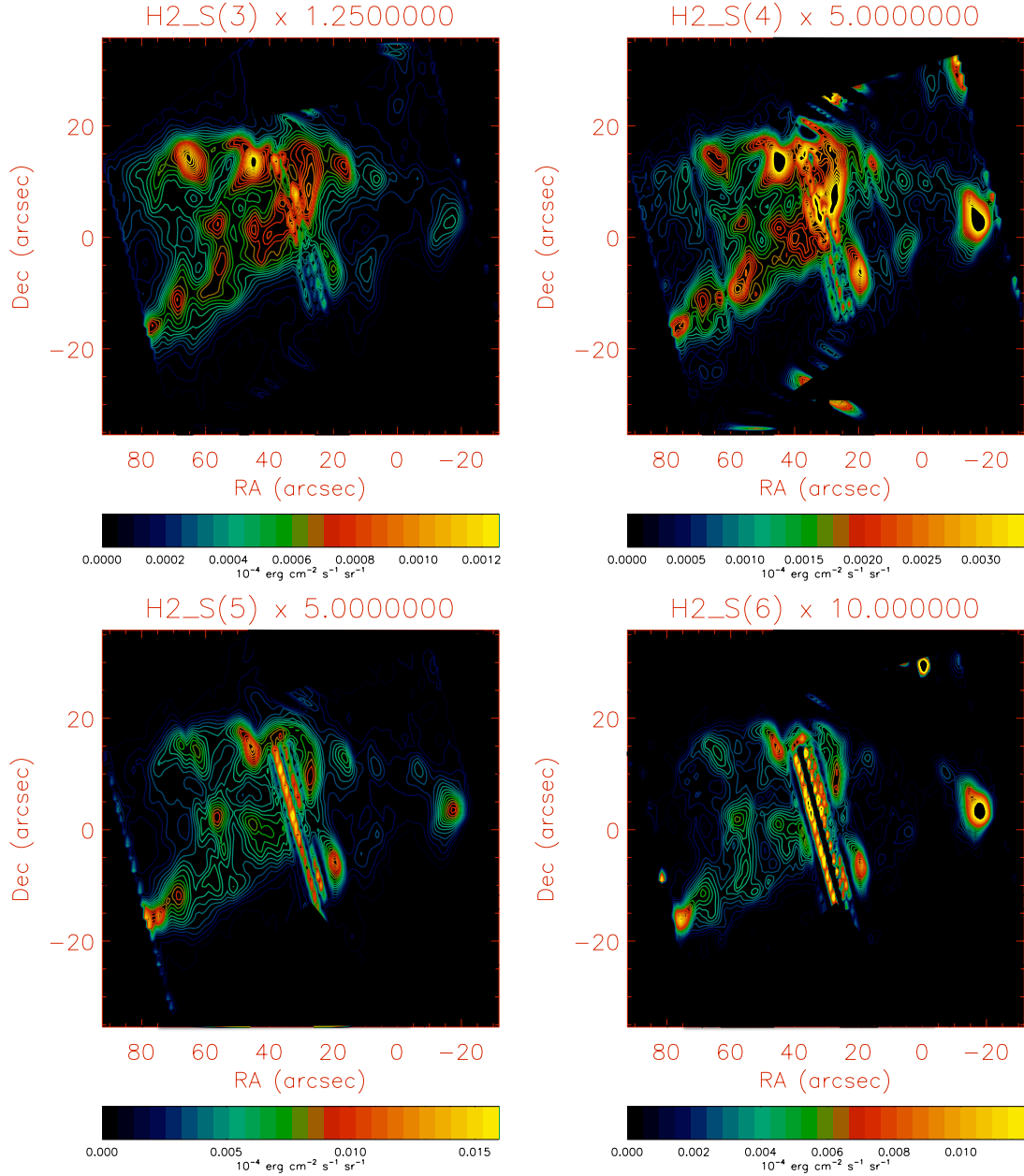
Figure 4.6   Intensity contour maps of all the detected lines and selected continuum maps and solid state feature maps.
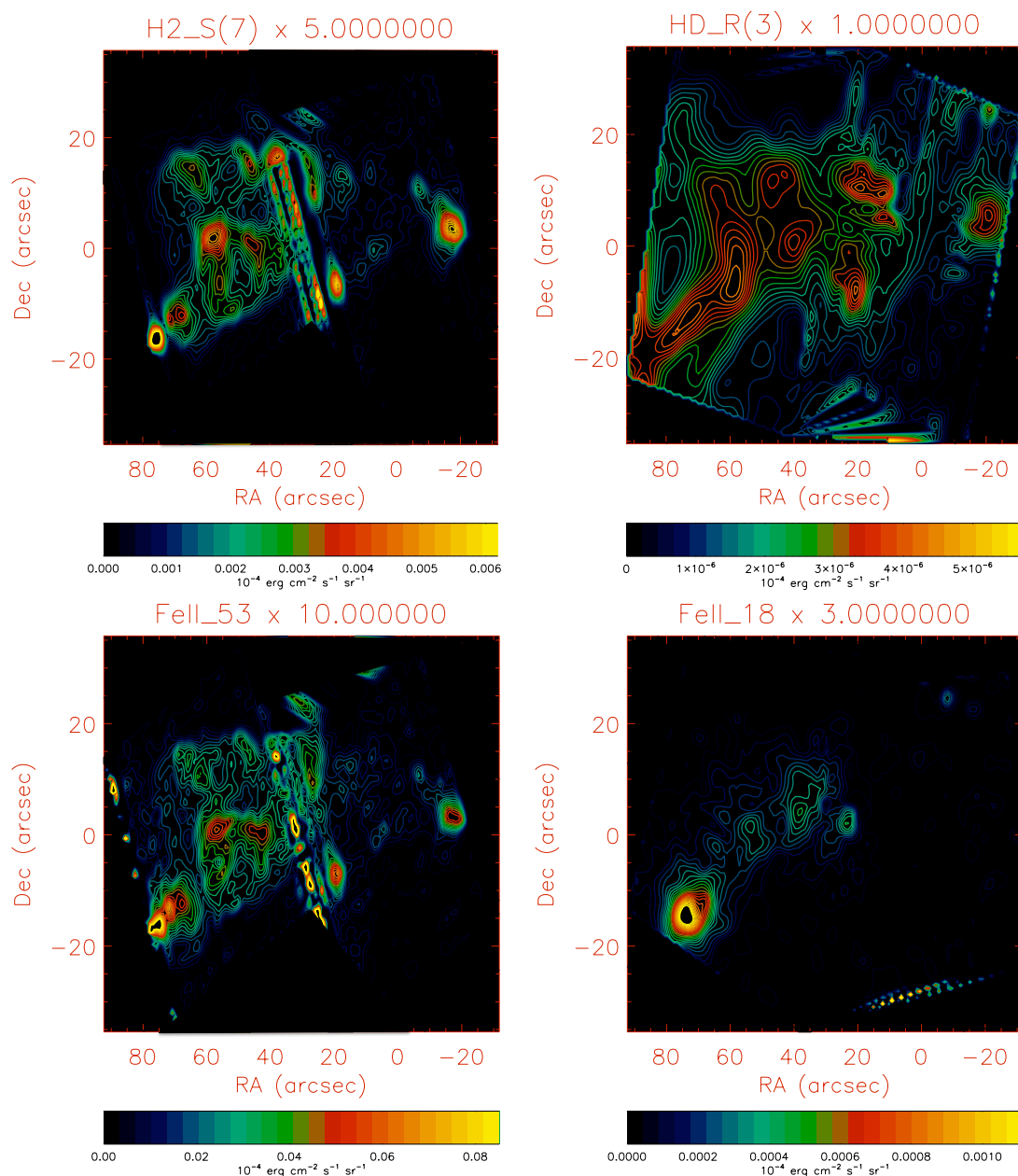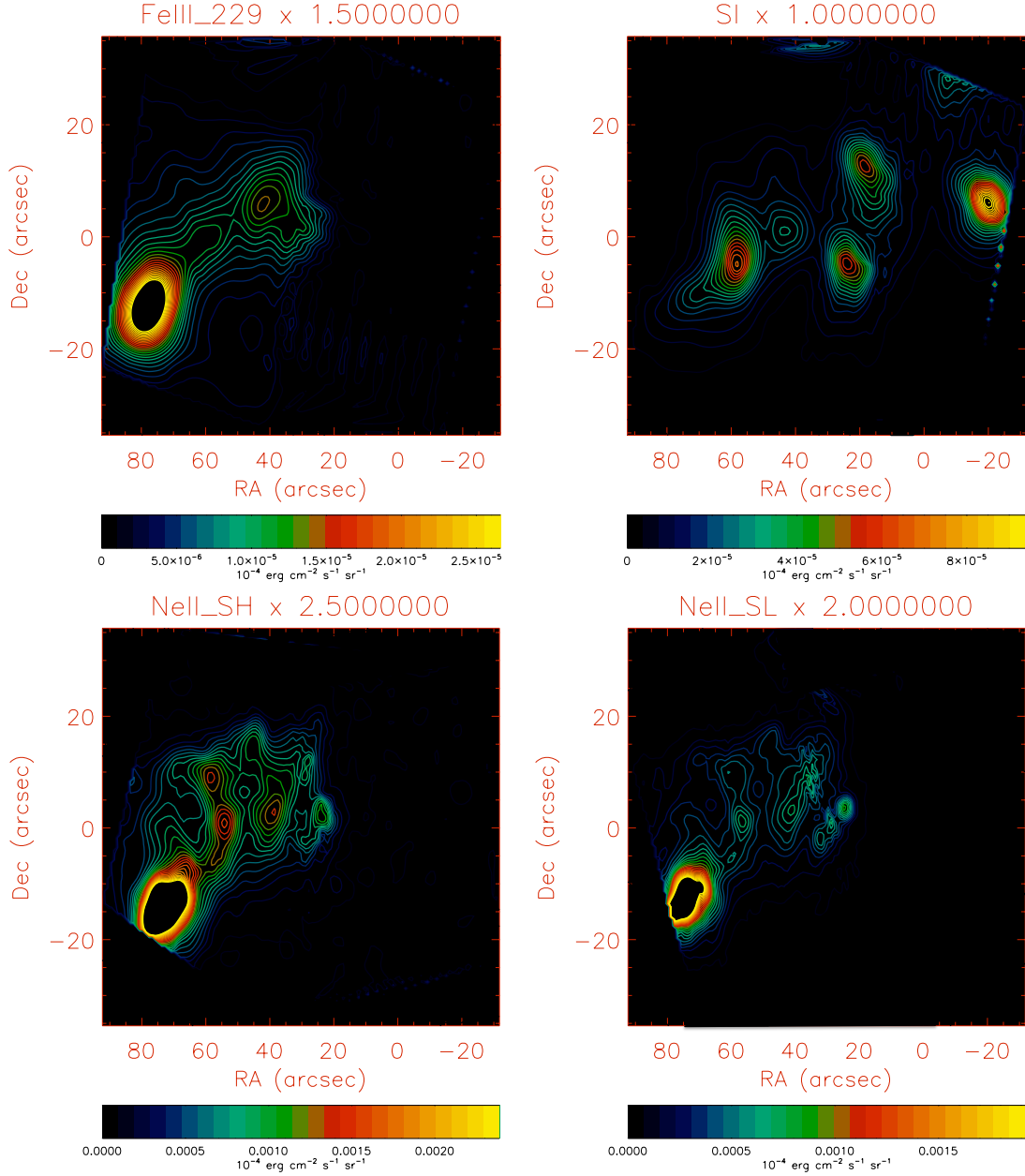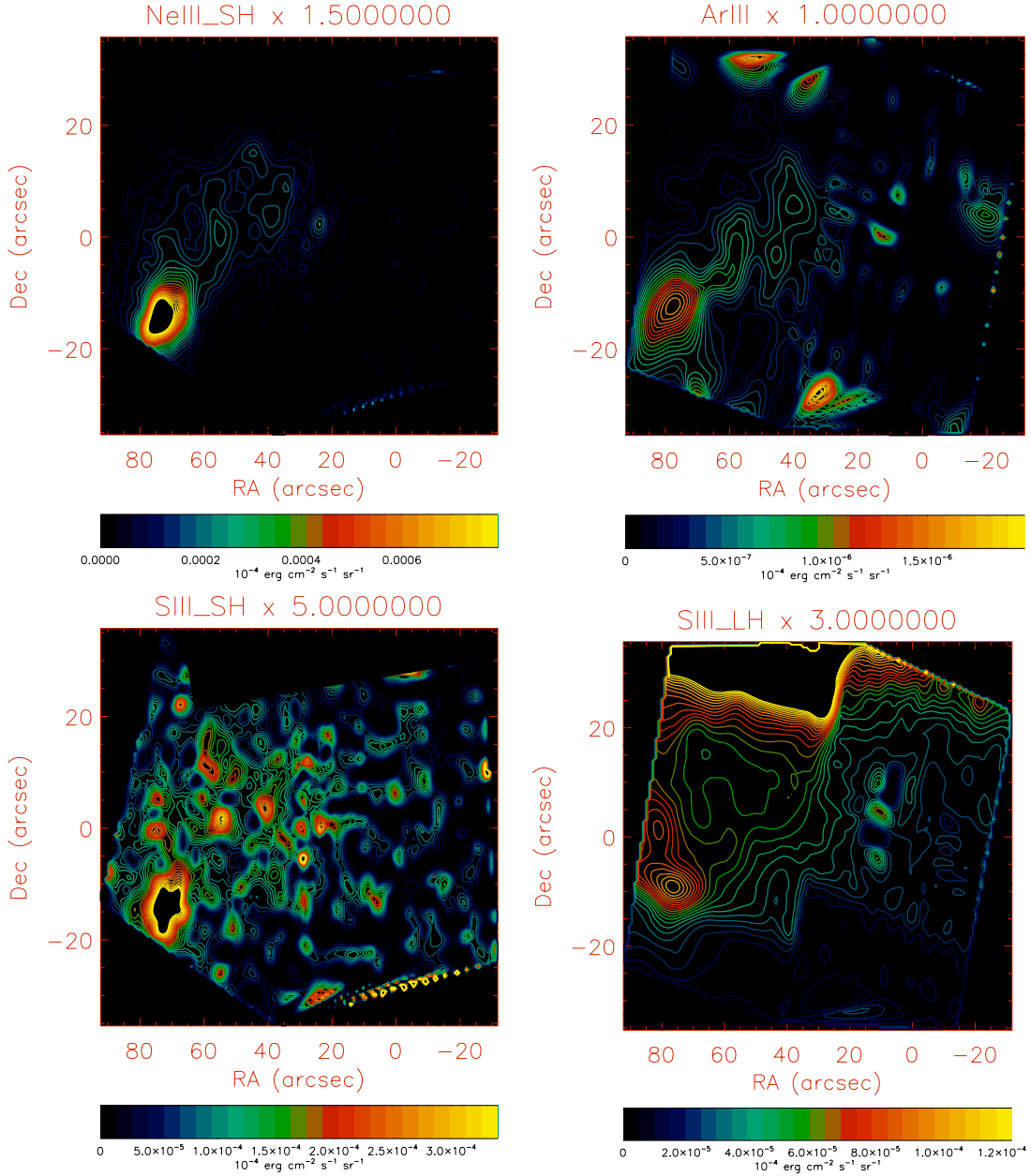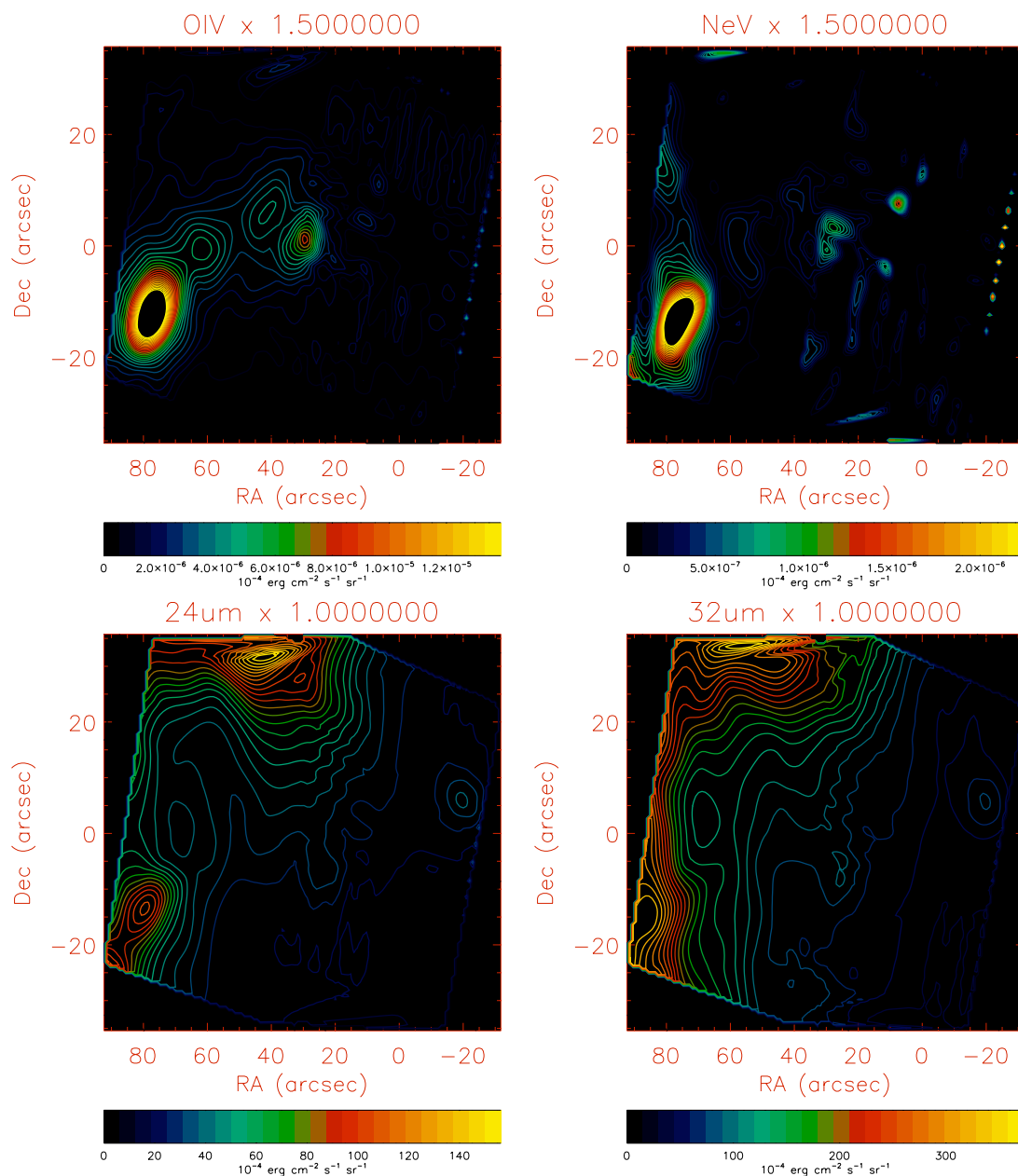
Figure 4.7 Intensity contour maps of all the detected lines and selected continuum maps and solid state feature maps.
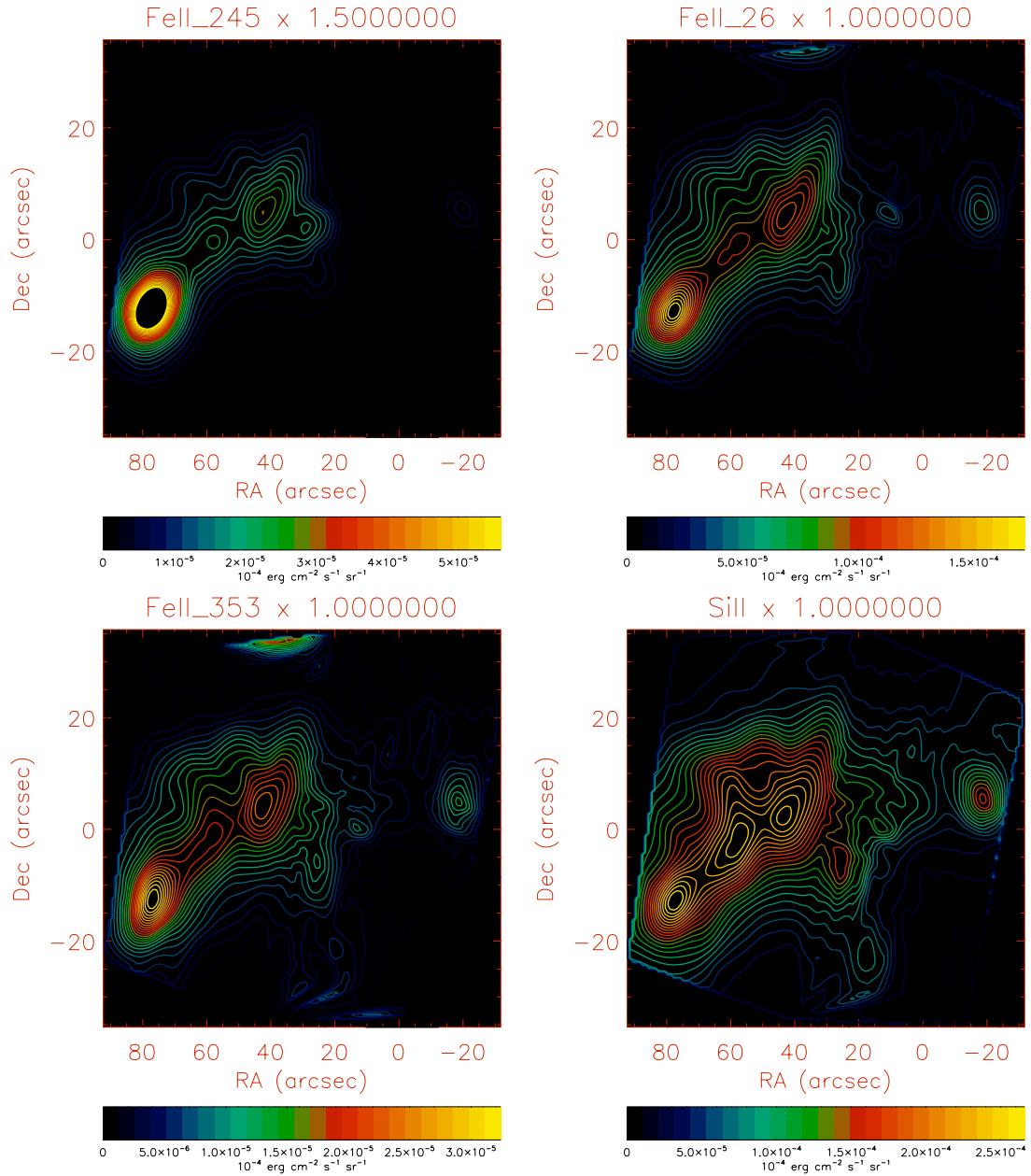
Figure 4.8 Intensity contour maps of all the detected lines and selected continuum maps and solid state feature maps.
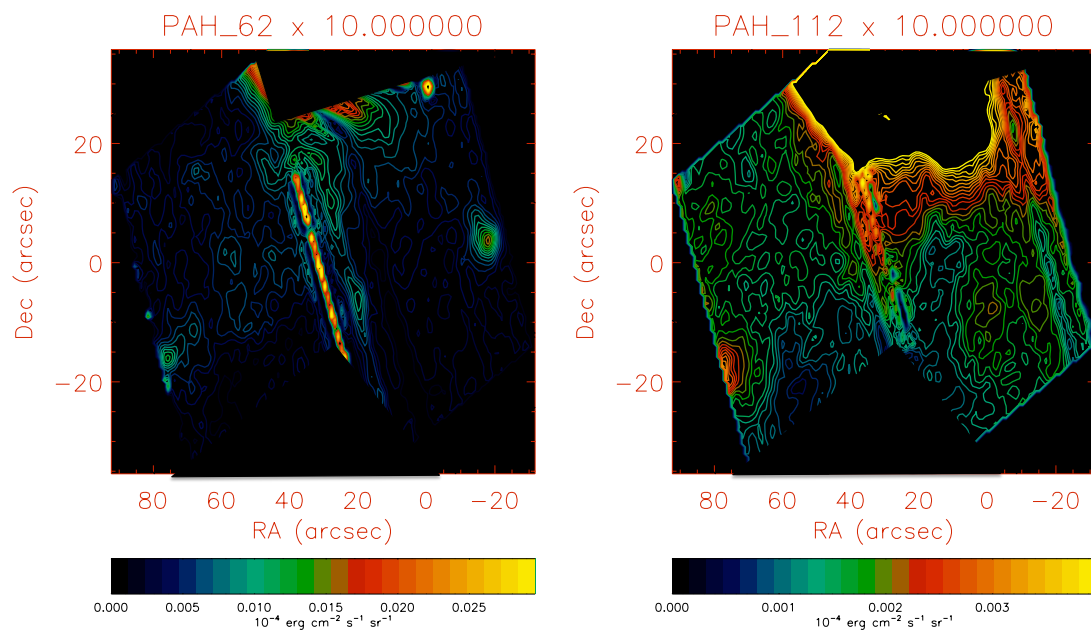
Figure 4.9 Intensity contour maps of all the detected lines and selected continuum maps and solid state feature maps.

Figure 4.10 Intensity contour maps of all the detected lines and selected continuum maps and solid state feature maps.

Figure 4.11 Intensity contour maps of all the detected lines and selected continuum maps and solid state feature maps.

Figure 4.12 Intensity contour maps of all the detected lines and selected continuum maps and solid state feature maps.
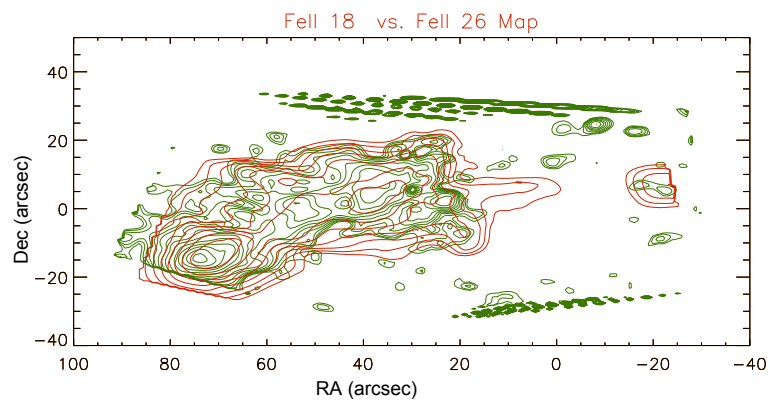

Figure 4.13 Comparison of [Fe II] [18 μm] (red) and [Fe II] [26 μm] (green).
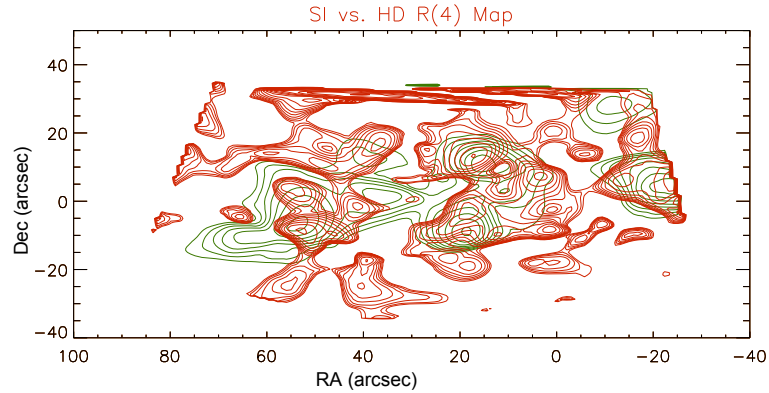
Figure 4.14   Comparison of HD R(4) [23 μm] (red) and [S I] (25.2 μm) (green).

km/s velocity appear throughout the map. The column density, temperature, and ratio are mapped in Figure 4.28. LTE assumes that at any given point all processes are in thermodynamic equilibrium at the local temperature; the collisional excitation and de-excitation rates are precisely balanced, as are the photon excitation and (spontaneous and stimulated) de-excitation rates.

Molecular hydrogen pure rotational emission is detected in all transitions from H_2 S(0) to S(7). The spatial distribution of the lower seven transitions are consistent, even in independent observations at different resolutions and times. It also correlates quite well with the higher resolution maps taken in K-band and shown in Raines (2000). The ratio of ortho-H_2 to para-H_2 drops off along the line of the northwest flow (Figure 4.28). The exception is the map of H_2 S(0), which shows additional excess emission to the north. This is likely due to emission from a protostellar source to the north of the mapped flow, which confuses the northern half of the map. The emission does not appear in S(1) through S(7) (Figure 4.21). We can also use the ortho-to-para ratio to determine a dynamical timescale, through a chemical clock, as we will see.

4.2.2   Fine Structure Emission

We detect and map spectral lines of ionized Fe, S, Si, Ar, O, and Ne. All lines of these species at IRS wavelengths are detected – with the exceptions of [S IV] at 10.5 um and [Ne III] at 36 μm – at excitation energies of up to 55 eV, and possibly higher (including five lines of [Fe II], two lines of [S III], and single lines
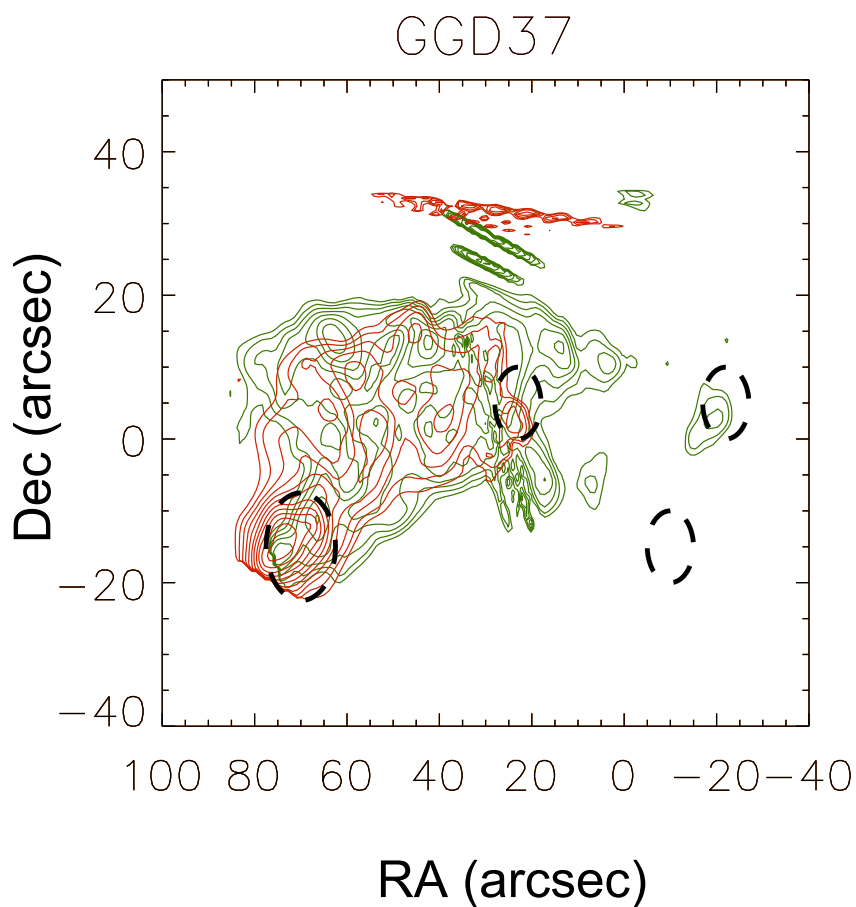
Figure 4.15 Comparison of [Fe II] [18 μm] (red) and H$_2$ S(1) (green). The peak of the molecular emission is shifted to the west by $\sim$ 5 arcseconds from the peak of the ionized emission region. The dashed circles represent four apertures of interest; from left to right: "W123", "Jethead", "Continuum", and "Westclump".
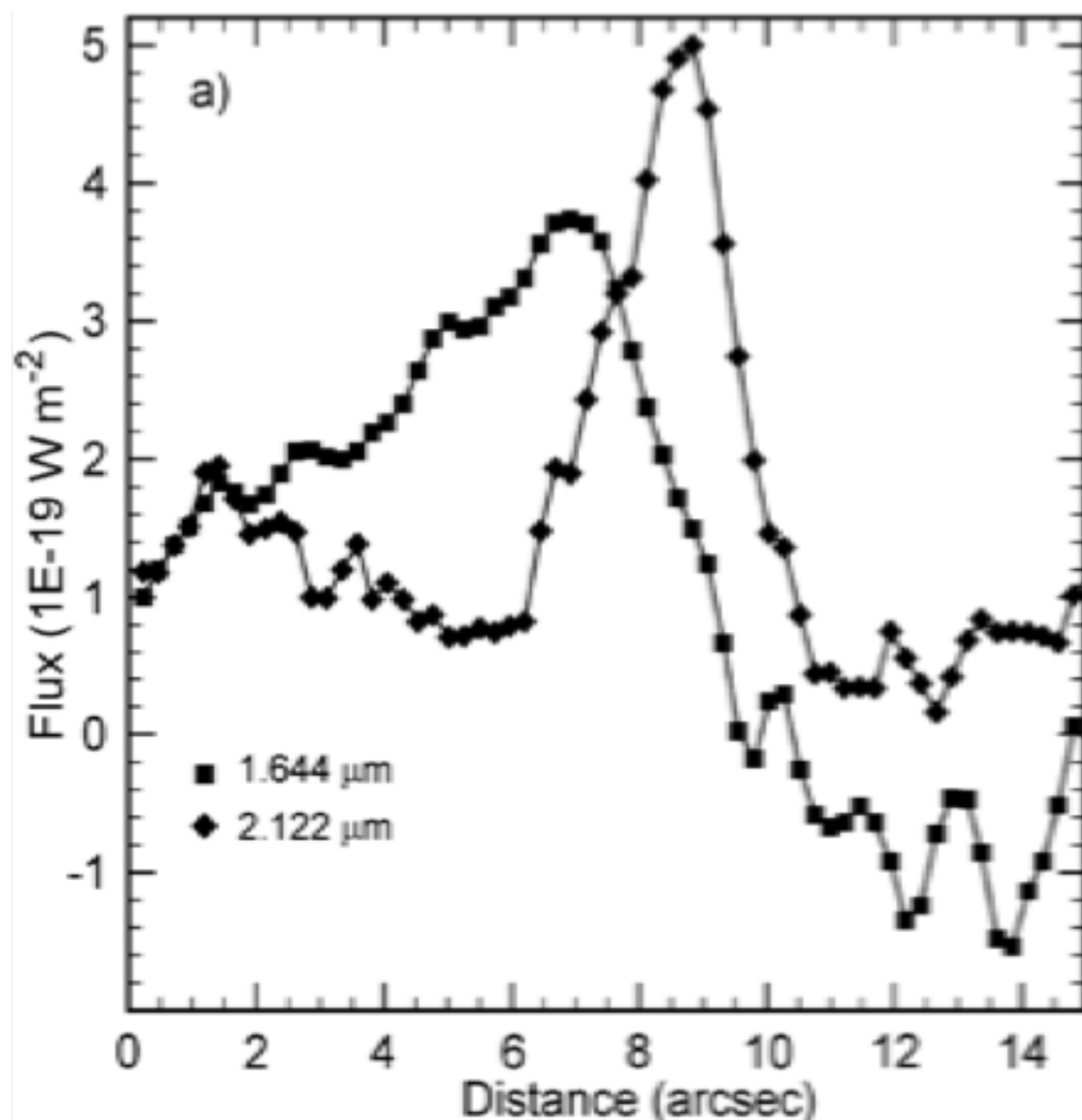
Figure 4.16   Comparison of the [Fe II] H-band emission and H_2 K-band emission
integrated over declination, showing the the difference in peak emission of each
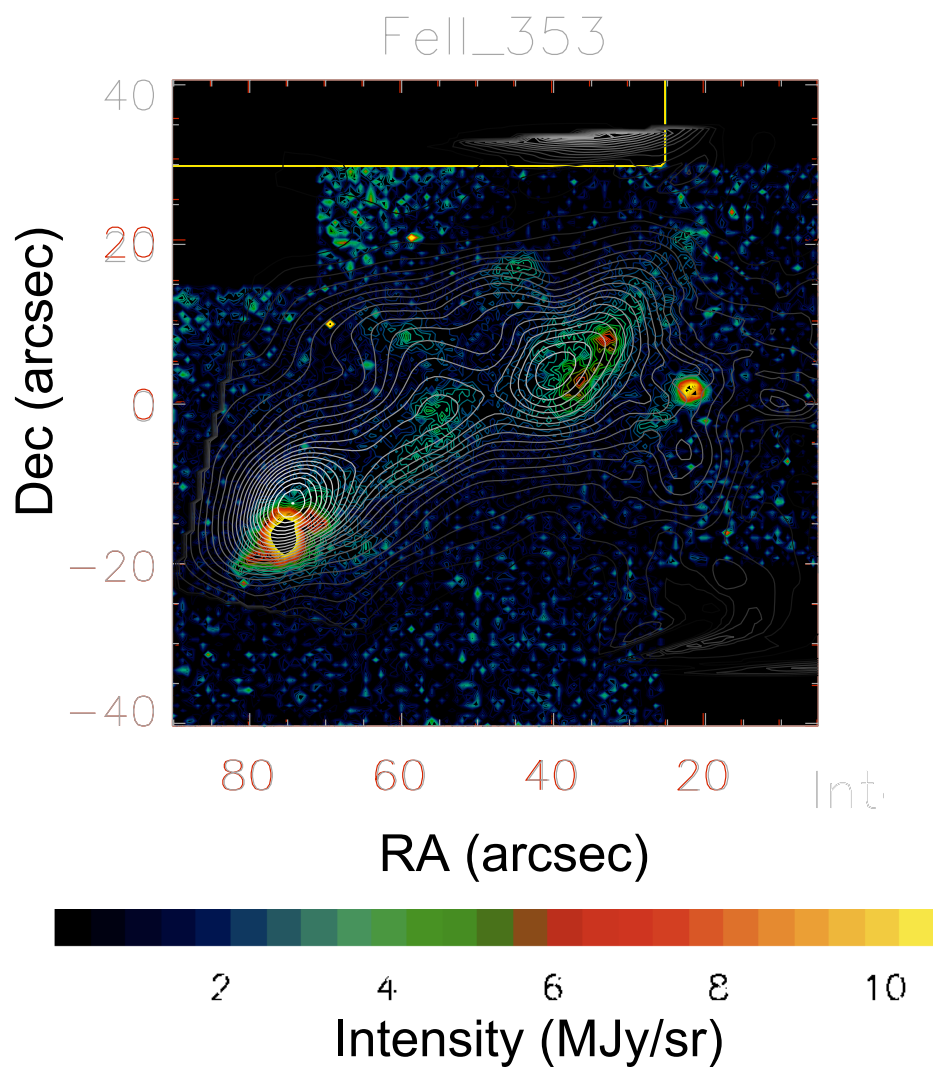species, reprinted from Raines (2000).

Figure 4.17 Comparison of [Fe II] [1.644 μm] (color contours) and [Fe II] [35.3 μm] (silver contours). The knots seen in the higher resolution H-band image match up well with the contours of the IRS map, suggesting that bow-shock features would be observed for all [Fe II] transitions at higher resolution.
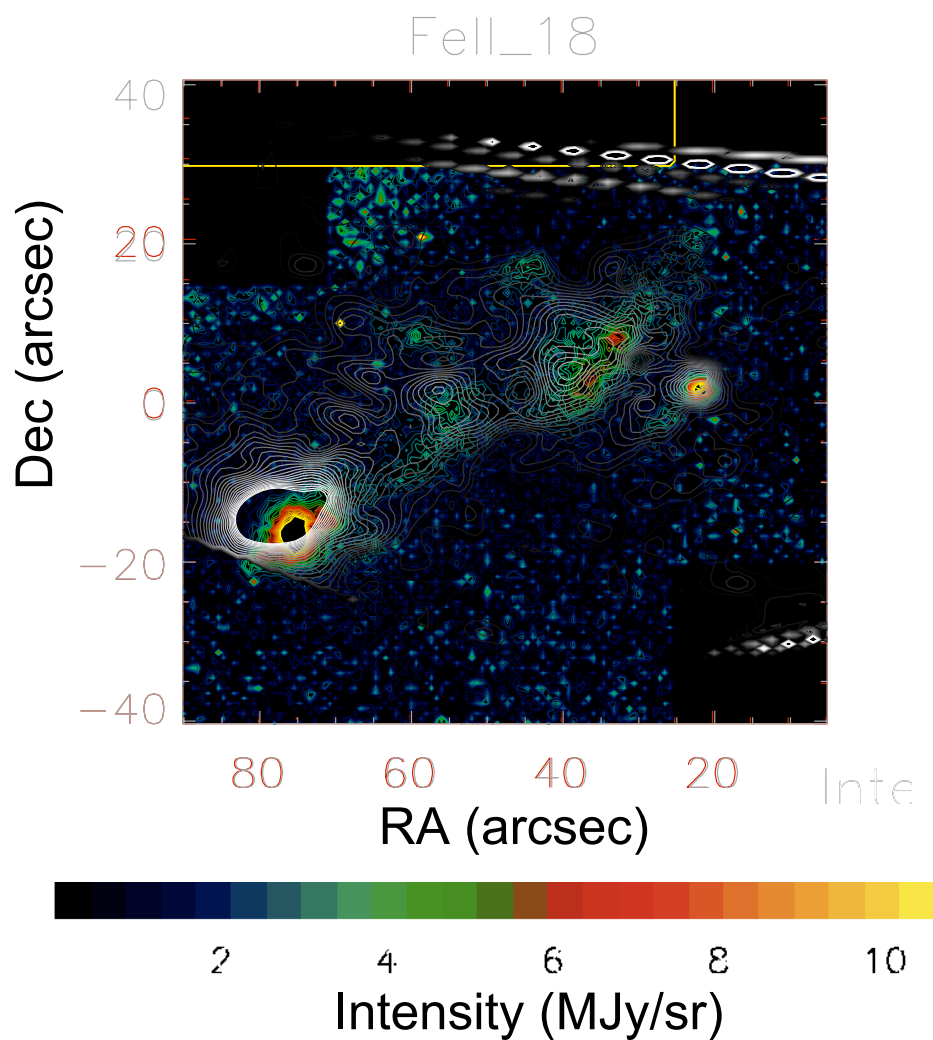
Figure 4.18   Comparison of [Fe II] [1.644 μm] (color contours) and [Fe II] [18 μm] (silver contours). The Short-High module has twice the spatial resolution and some of the finer features are reproduced at 18 μm as well as a few potentially new knots.
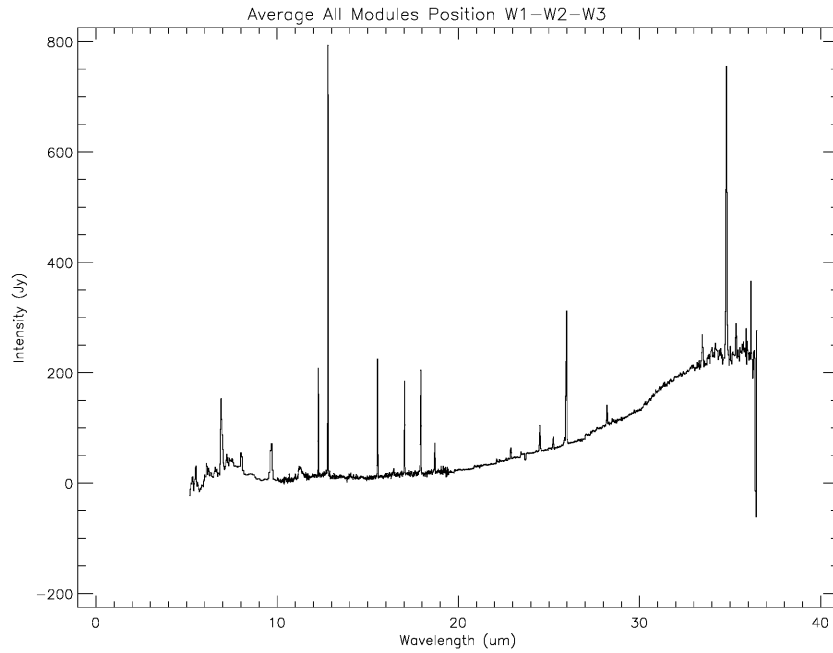
Figure 4.19 Spectrum taken in all modules from an aperture centered around the main concentration of higher excitation emission, the region around W1/W2/W3. The SL has been multiplied by 1.5 to match SH.
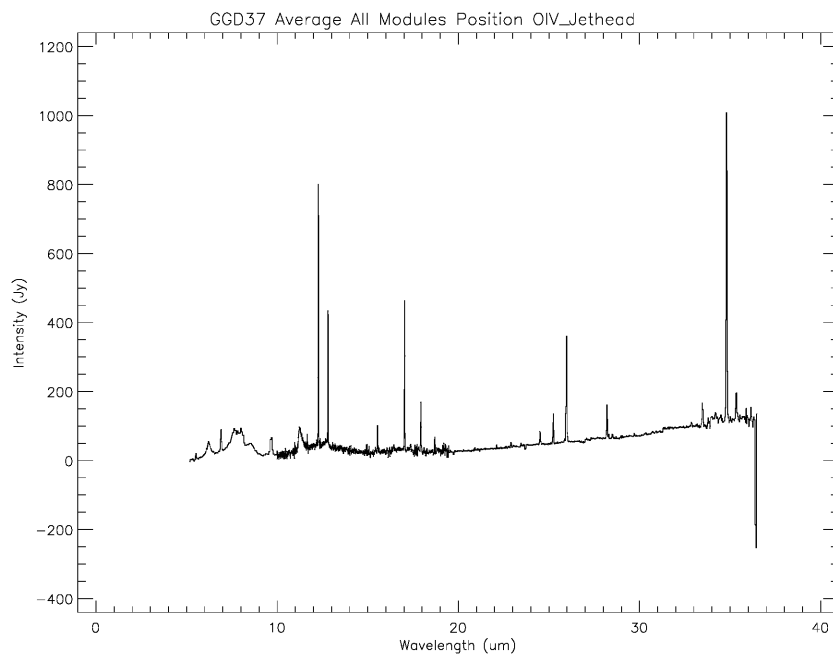
Figure 4.20 Spectrum taken in all modules from an aperture centered at the
northwestern edge of the higher excitation flow, which may represent the working
surface where the shock front is colliding with the molecular cloud. The SL has
been multiplied by 1.5 to match SH.
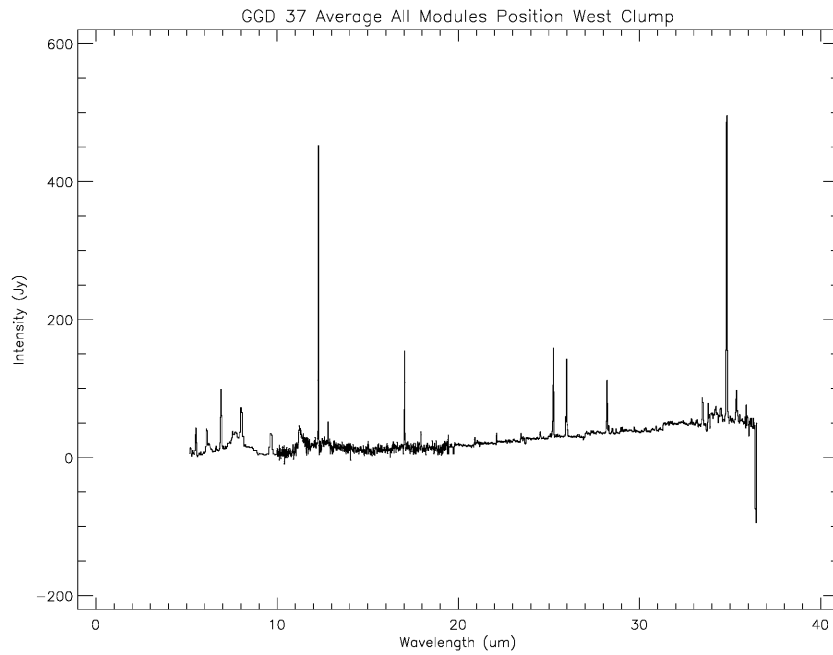
Figure 4.21   Spectrum taken in all modules from an aperture centered around the westernmost clump of emission in the map. The SL has been multiplied by 1.5 to match SH.

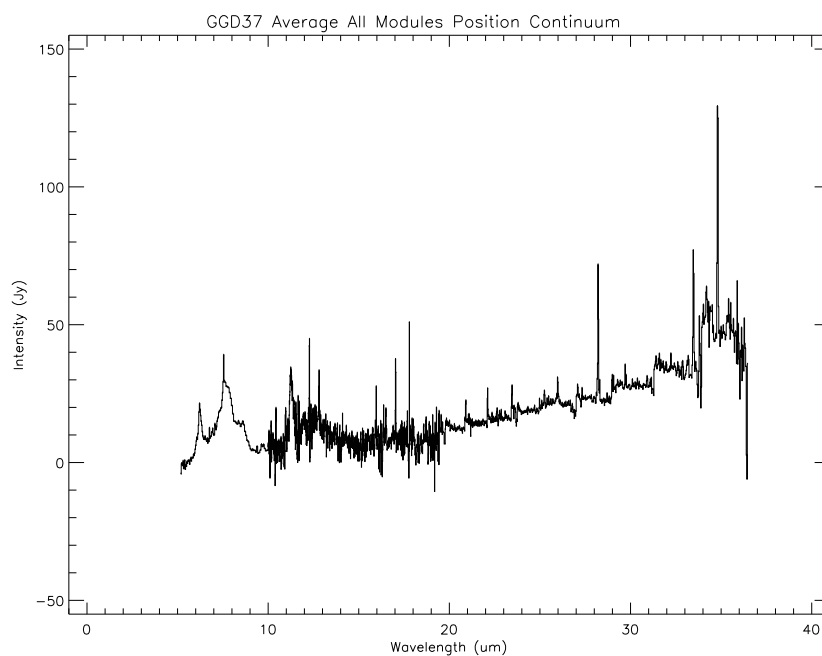**Figure 4.22**   Spectrum taken in all modules from an aperture centered in the
southwestern portion of the map where none of the atomic or fine structure emis-
sion appears. The SL has been multiplied by 1.5 to match SH. The remaining
broad features are due to PAH emission, while the line emission is from the first
few pure rotational states of molecular hydrogen.

of [Si II], [Fe III], [Ne II], [Ne III], and likely [O IV] and [Ar III] (21.83 μm), as well as possibly [Ne V]; see Table 4.3). Additionally there is a possible detection of [Ar III] (8.99 μm); the detection seems real at the position of W2 (there is a smooth gaussian line profile at the correct wavelength) and in fact the 8.99/21.83 μm ratio is ~ 25 – quite reasonable for a density of $n_e = 10^{3-4}$ cm^{-3} (Allen et al., 2008), but mapping the line revealed no structure in the emission outside of a slight peak around W2. Any expected emission from the lower ionization state [Ar II] (6.99 μm) would be lost amongst the strong H$_2$ S(5) detection at the same wavelength, which is ~ 36 times greater than the [Ar III] 8.99 μm flux, which makes a positive identification difficult for the 8.99 μm feature.

The westernmost flow, as noted by Raines (2000) Figure 3.13, does not exhibit much emission from higher excitation lines. Although the flow is not detected at [Fe II] (1.644 μm) (Raines, 2000), it does appear in [Fe II] at all *Spitzer* wavelengths (Figure 4.13), but only in ionized species requiring an excitation energy of ~ 8 eV or less, with the possible exception of [Ar III] (21.83 μm).

Other features of the fine structure emission:

- The [S III] 18.7 μm map shows a peak at W2 but very little structure outside of it, although there is a greater concentration in the eastern half of the map. The 33.4 μm line is very different in morphology, indicating a rising flux to the NE and resembling the 24 and 32 μm continuum maps.

- The [Fe II] mid-IR lines correlate extremely well with the near-IR [Fe II] line, although there are some additional sources that radiate only at longer wavelengths (see Figures 4.17, 4.18).

- The [Si II] map is closely correlated with the [Fe II] 35.3 μm map. Given that these transitions require similar levels of excitation this is unsurprising.

- The HD R(3) map roughly resembles the H$_2$ S(1)-S(7) emission but emits more in the SE corner than H$_2$.

- The [S I] map consists of four or five clusters, including the westernmost clump. Peak A is in the middle of the HH 168 flow, Peak B and C are in the continuum between HH 168 and the westernmost clump. Peak D is the westernmost clump.
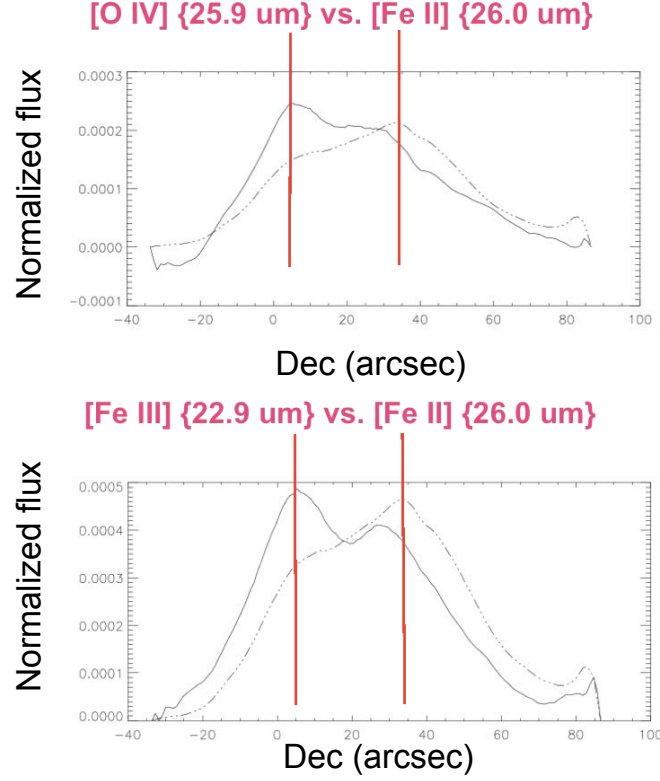
Figure 4.23 Comparison of the peak of bow shock emission in different excitation species, in terms of normalized flux (vertical axis), as a function of declination (horizontal axis), similar to the analysis in Raines (2000). In both plots the solid curve represents [Fe II]. The dashed line represents [O IV] (top) and [Fe III] (bottom). In both cases the higher excitation energy profile peaks $\sim$ 25-30 arcseconds to the east of the [Fe II] flux profile, with a secondary peak $\sim$ 5 arcseconds east of the [Fe II] profile.

4.2.3 Extremely High Excitation Lines

We report the first detection of [Ar III], [O IV] or [Ne V] in a Herbig-Haro flow (Figure 4.24). Despite its relatively weak flux, the [O IV] detection is quite solid and its emission tracks the [Fe II] emission knots extremely well. The [Ar III] map is similar structurally to the other lines, with the exception that it appears to contribute to the westernmost clump in the map, unlike the other higher excitation species.

The apparent [Ne V] emission is confined to the area around W2 and a point at the northwest end of the flow (Figure 4.25), roughly coinciding with the edge of

the lower excitation line emission from [Fe II]. Raines (2000, his figure 3.15) noted that the peak of the [Fe II] (1.644 μm) emission was shifted to the east by ~ 3 arcseconds from the peak of the H$_2$ (2.122 um) emission; we note a similar result in our maps–although the spatial resolution is considerably lower– we can clearly see that the peak emission from all of the ionized species is located east of the peak of the H$_2$ S(1) - S(7) emission. Additionally, the higher ionization species appear to be themselves shifted eastward by a further ~ 5 arcseconds compared to the lower ionization species, suggesting that we are resolving the cooling region (Figure 4.23). The aperture "Jethead" then represents the bulk of the transition region.

4.2.4   HD Emission

As reported by Neufeld et al. (2006a), the GGD 37 maps reveal evidence of HD at a few times lower than the cosmic abundance. The HD R(3) and possibly R(4) lines are detected. The R(3) line correlates well with the H$_2$ distribution, while the R(4) line does not, although it may correlate somewhat with several peaks in the [S I] (atomic sulfur) map (Figure 4.14), which is itself quite different from both the molecular hydrogen emission and the fine structure and higher excitation ionic lines.

It is unfortunate that we find the HD R(4) detection is marginal. If the detection were substantial, it would provide a sensitive density probe for the low temperature molecular gas.

4.2.5   H$_2$O Emission

We detect water vapor emission around the radio source W2, from a subset of the water lines between 30 and 36 μm detected in the Class 0 protostar NGC 2071 using IRS (Melnick et al., 2008). See Figure 4.26 and Table 4.2 for values; the typically strongest lines correlate with weak emission features in the spectrum. Water is the dominant coolant in outflows from YSOs and would be a strong indication that W2 is in fact a protostar, rather than a bullet or clump in a flow originating from HW3c.
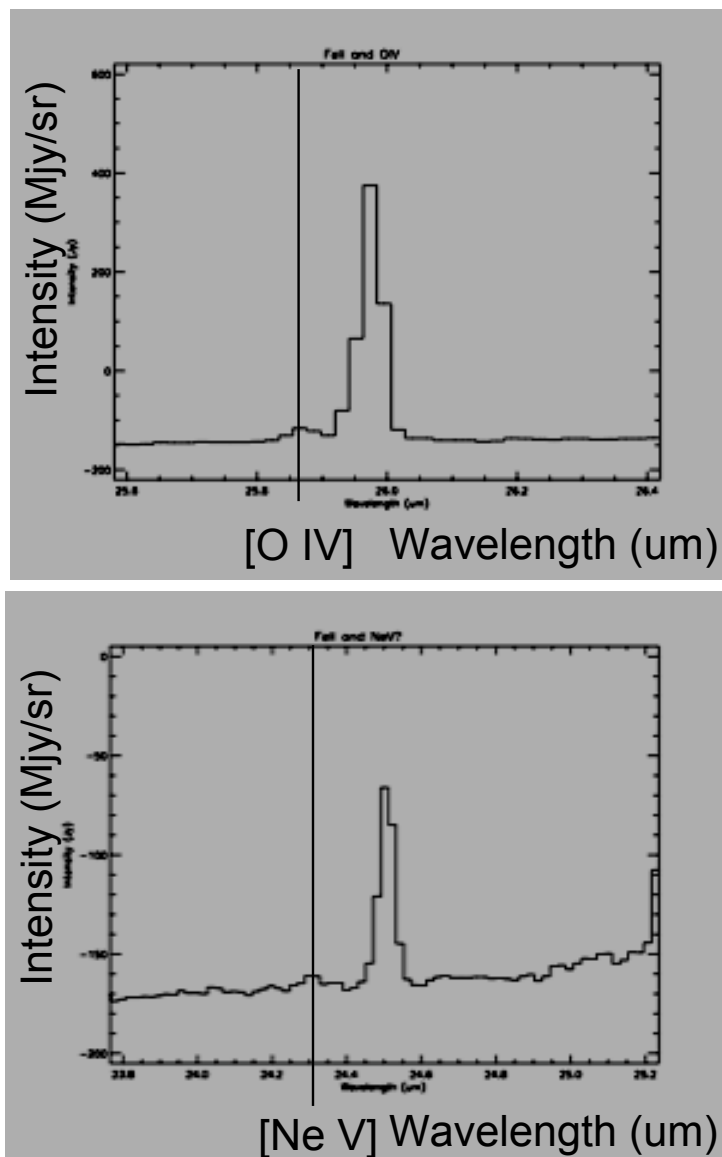
Figure 4.24 Zoomed view of spectra taken in the "W2" aperture. The dashed line indicates the centroid of [O IV] (25.9 μm) (top) and [Ne V] (24.3 μm) (bottom) emission. In both cases there is a bright [Fe II] line at slightly longer wavelengths (26.0 and 24.5 μm, respectively).
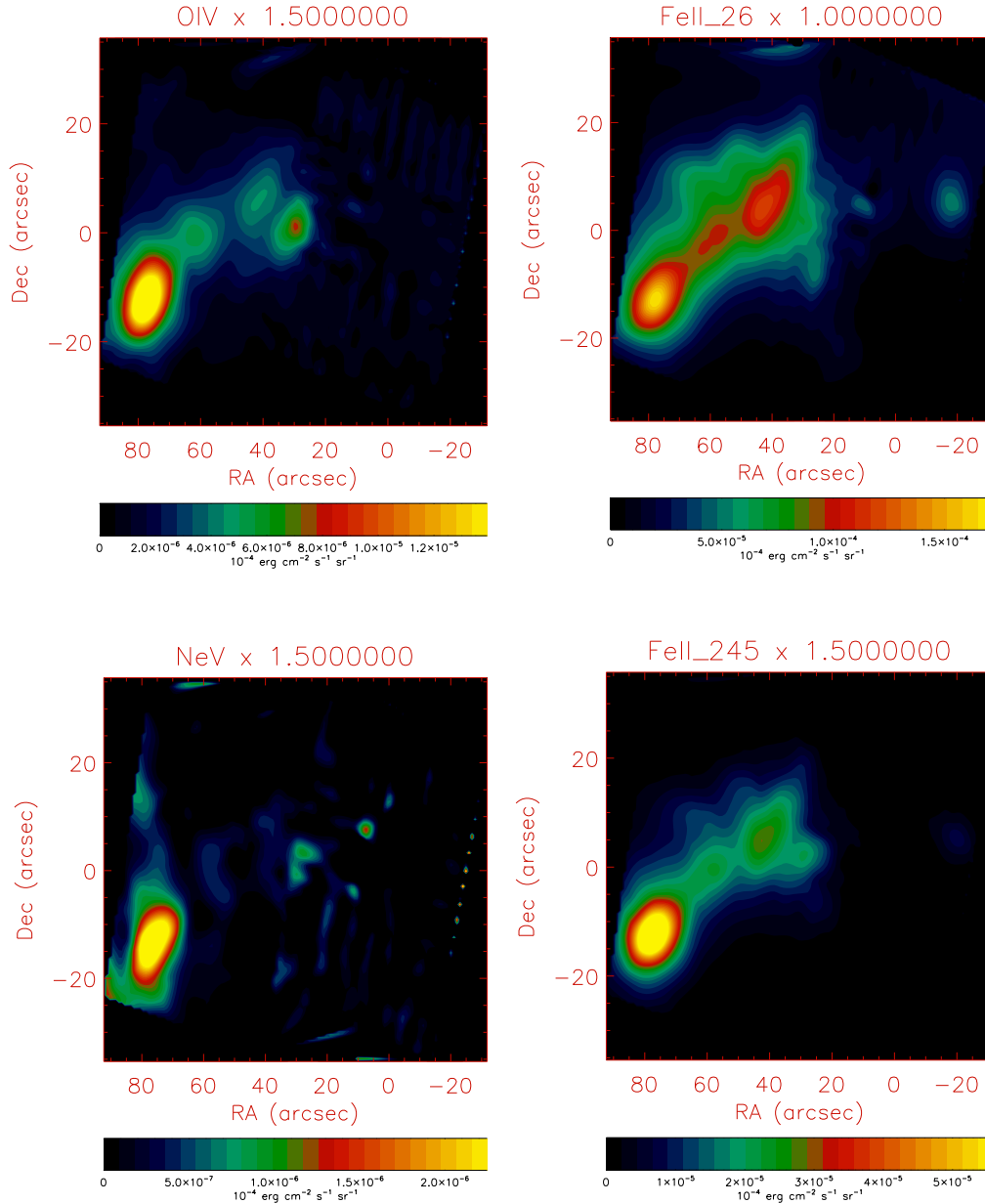
Figure 4.25 Top and Bottom Left: Zoomed view of spectra taken in the "W2" aperture. The dashed line indicates the centroid of [O IV] (25.9 μm) and [Ne V] (24.3 μm) emission. In both cases there is a bright [Fe II] line at slightly longer wavelengths (26.0 and 24.5 μm, respectively). Top Center: Map of [O IV] emission from W2 (lower left corner) to the edge of the ionized flow (upper right corner). Although the streaks angled west-east are artifacts, the emission peaks at two additional locations in the map: first, at the convergence of W1/W2/W3, and second at a point just inside the edge of the flow of lower ionization spectral lines. Top Right: The same region of sky mapped in [Fe II] 26 μm for comparison. Bottom Center: The same plot for [Ne V] emission. Bottom Right: [Fe II] 24.5 μm. Although the [Ne V] detection is weak, the spatial distribution of the emission suggests that it is real, and spatially distinct from the stronger [Fe II] emission.

Table 4.2.   Lines of Water Detected in W123 Aperture

Wavelength (um)	A-Coef	Upper State	Final State
30.8994	0.35	6 3 4	5 0 5
34.5489	1.77	7 3 4	6 2 5
35.4285	4.52	7 4 3	6 3 4
35.6694	4.24	8 4 5	7 3 4
35.9379	7.73	6 5 2	5 4 1

Note. — Assumes thermal equilibrium and a temperature of
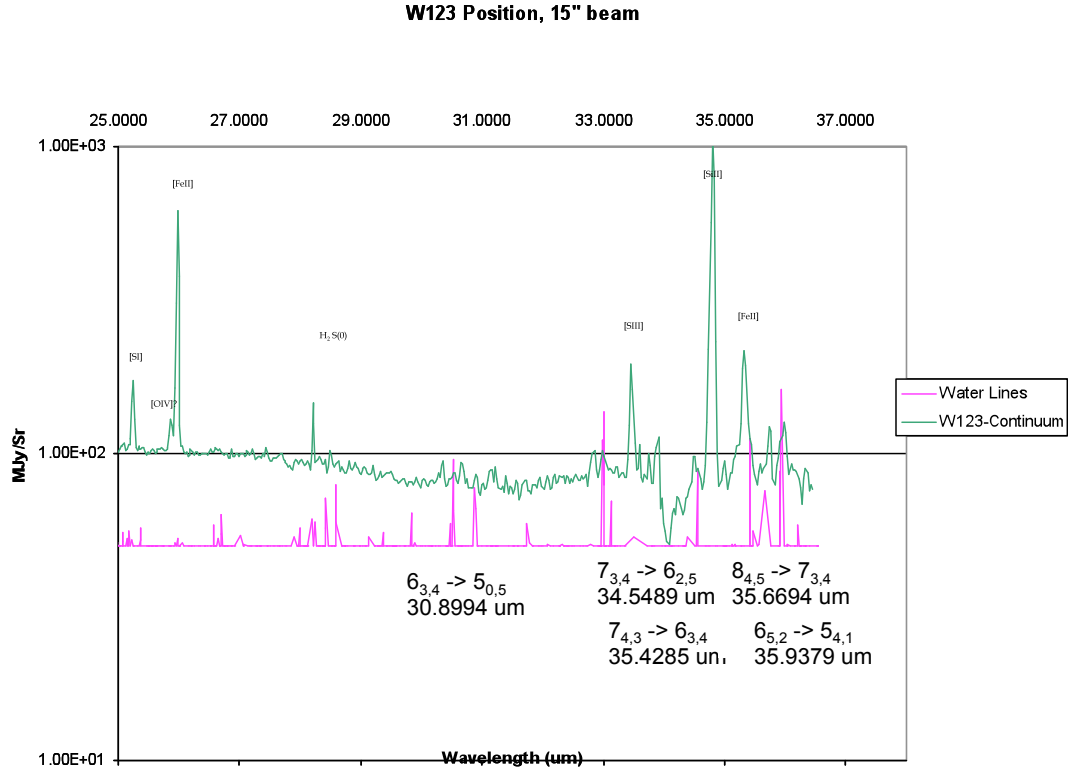300 K.

Figure 4.26   Top: continuum subtracted 25-36 μm spectrum taken from a 15"
beam centered around the W2 region, with labeled spectral lines. Bottom: a
plane-parallel slab model of water emission from the HITRAN database. Several
lines appear (weakly) in the spectrum and are identified in Table 4.2.

Table 4.3. Excitation Energies of Detected Transitions in GGD 37

Species	Centroid Wavelength (um)	Modules	Excitation Energy (eV)	Detected?
H_2 S(0) J = 2 - 0	28.23	LH	–	yes
H_2 S(1) J = 3 - 1	17.04	SH	–	yes
H_2 S(2) J = 4 - 2	12.29	SH/SL1	–	yes
H_2 S(3) J = 5 - 3	9.71	SL1	–	yes
H_2 S(4) J = 6 - 4	8.07	SL1	–	yes
H_2 S(5) J = 7 - 5	6.94	SL2	–	yes
H_2 S(6) J = 8 - 6	6.11	SL2	–	yes
H_2 S(7) J = 9 - 7	5.52	SL2	–	yes
HD R(3) J = 4 - 3	28.50	LH	–	yes
HD R(4) J = 5 - 4	23.03	LH	–	maybe
[S I]$^3P_1 -^3 P_2$	25.24	LH	–	yes
[Fe II] $^6D_{5/2} -^6 D_{7/2}$	35.35	LH	8	yes
[Fe II] $^6D_{7/2} -^6 D_{9/2}$	25.97	LH	8	yes
[Fe II] $^4F_{5/2} -^4 F_{7/2}$	24.52	LH	8	yes
[Fe II] $^4F_{7/2} -^4 F_{9/2}$	17.93	SH	8	yes
[Fe II] $^4F_{9/2} -^6 D_{9/2}$	5.34	SL2	8	yes
[Si II] $^2P^0_{3/2} -^2 P^0_{1/2}$	34.80	LH	8	yes
[Fe III] $^5D_3 -^5 D_4$	22.93	LH	16	yes
[Ne II] $^2P^0_{1/2} -^2 P^0_{3/2}$	12.81	SH/SL1	22	yes
[S III] $^3P_1 -^3 P_0$	33.48	LH	23	yes
[S III] $^3P_2 -^3 P_1$	18.71	SH	23	yes
[Ar III] $^3P_1 -^3 P_2$	8.99	SL1	28	maybe
[Ar III] $^3P_0 -^3 P_1$	21.83	LH	28	maybe
[S IV] $^2P_{3/2} -^2 P_{1/2}$	10.5	SH/SL1	35	no
[Ne III] $^3P_0 -^3 P_1$	36.0	LH	41	no
[Ne III] $^3P_1 -^3 P_2$	15.55	SH	41	yes
[O IV] $^2P_{3/2} -^2 P_{1/2}$	25.89	LH	55	maybe
[Ne V] $^3P_1 -^3 P_0$	24.30	LH	97	maybe
[Ne V] $^3P_2 -^3 P_1$	14.32	SH	97	no

Note. — Excitation energies of observed transitions in GGD 37. [S IV] is not detected, likely because of the lower abundance of sulfur in the region. The [O IV] is significant spectroscopically, but the blending of the line with [Fe II] at 26 μm may introduce difficulties in separating the emission spatially – although the principal component analysis shows a clear separation. The [Ne V] is still a several sigma detection, unblended, although the map is likely affected by artifacts and underlying continuum emission. The [Ne III] line at 36 μm is likely extinguished or lower population state.

Figure 4.27 An illustration of jump-type conditions from an F-18 breaking the
sound barrier, from the Astronomy Picture of the Day.

4.3 Analysis

The abundance of spectral lines provides us with one of the most extensive datasets
to characterize the interactions of outflows and shocks with the ambient molecular
cloud. Different species trace different portions of the shock.

For the cloud shock, H_2 S(0)-S(7) provide column density, temperature, ortho-
to-para ratio, and extinction constraints. With the HD detections we can track
the deuterium abundance across the cloud, and with HD R(4) and S I we have a
measure for some of the lowest temperature interactions. H_2O provides the total
cooling rate in the cloud.

The significance of ortho-to-para ratios is well-established from previous pa-
pers (e.g. Neufeld et al., 2006b), but I will briefly review the analysis here. The
equilibrium ratio of the ortho-H_2 emission to the para-H_2 emission is 3, for T
$\gtrsim$ 300 K. Although the gas temperature in the northwestern portion of the HH

Table 4.4.   Flux Density by Chemical Species by Aperture (10^{-5} erg/s/cm^2/sr)

Species	Module	W123 Flux	Jethead Flux	Westclump Flux	Continuum Region Flux
H$_2$ S(0)	LH	0.94	0.29	0.24	0.16
H$_2$ S(1)	SH	4.80	4.29	2.34	0.62
H$_2$ S(2)	SH	8.26	11.10	11.26	1.04
H$_2$ S(3)	L1	28.4	21.24	15.38	1.71
H$_2$ S(4)	L1	18.52	41.09	31.82	–
H$_2$ S(5)	L2	61.6	25.3	37.7	–
H$_2$ S(6)	L2	20.9	42.9	13.8	–
H$_2$ S(7)	L2	17.0	12.2	29.8	2.44
H$_2$ S(2)	L1	8.25	13.8	12.5	0.94
[Ne II]	L1	54.7	15.6	–	5.6
[Ne II]	SH	37.8	6.47	–	0.46
[Fe II] 18	SH	6.18	1.31	0.32	0.22
[Fe II] 26	LH	1.06	1.42	0.43	0.043
[S I]	LH	1.40	0.36	0.57	0.029
[Si II]	LH	17.4	3.46	1.55	0.30
HD R(3)	LH	0.025	0.048	0.031	0.0060
PAH 11.2	L1	12.8	38.2	10.39	12.9
PAH 6.2	L2	42.0	58.3	16.8	21.9
[Fe II] 5.3	L2	3.67	5.09	–	10.8
[Fe III] 22.9	LH	0.12	0.10	–	10.28
[Fe II] 24.5	LH	0.25	0.23	0.037	0.0012
[Fe II] 35.3	LH	0.17	0.33	0.14	0.019
[O IV]	LH	0.074	0.034	–	0.0036
[Ne V]	LH	0.012	0.013	–	–
[S III]	SH	1.53	0.43	0.064	0.15
[S III]	LH	1.82	0.24	0.13	0.15
[Ne III]	SH	7.89	0.98	–	0.36
[Ar III]	LH	0.089	–	–	–

Note. — Flux density in units of erg/cm^2/s/sr of all species at 15" FWHM beams of four regions of interest: the W1-W2-W3 emission complex (W123), the extreme NW end of the HH 168 flow (Jethead), the westernmost clump of molecular hydrogen and [Fe II] emission (Westclump), and a selected region devoid of structure in the southeastern corner of the map (Continuum Region). In order to integrate the different modules, we utilized the flux of the [Ne II] as a normalization constant; the SH fluxes are thus decreased by a factor of ~ 4.5 from observed values, and the SL2 spectra are decreased by 1.33 to match continuum levels with SL1. A " – " marking indicates a non-detection or failed linefit. In case of the fine structure lines, the final column if detected can be used as an alternate 1σ uncertainty value.

Table 4.5.   Fitting Parameters for LTE Model of H_2 Emission at W2

Parameter	Value (W2)	Value (Westclump)
log10(J=2)	18.9	19.2
log10(J=3)	19.1	18.7
log10(J=4)	18.4	18.5
log10(J=5)	18.3	18.0
log10(J=6)	17.6	17.8
log10(J=7)	17.7	17.5
log10(J=8)	16.9	16.7
log10(J=9)	16.5	16.7
T(warm)/K	434	648
log10(N(warm))	19.5	19.5
OPR(warm)	3.23	0.49
T(hot)/K	1038	1559
log10(N(hot))	19.3	18.6
OPR(hot)	1.98	2.98
log10(N(total)	19.7	19.6
log10(N(4-9)	18.7	18.7
T42	706	566
T53	686	720
T64	797	889
T75	1170	1257
T86	1239	824
T97	881	1364

Note. — Derived fit to a two-temperature model of H_2 rotational transitions. As in HH54 and HH7-11 the temperatures correspond to a slower 15-20 km/s C-type nondissociative shock.

168 flow, for example, is well above this value, we observe non-equilbrium (low) ortho-to-para ratios. This indicates that the molecules in this area have not equilibrated from the compression shock that has passed by them (yet not dissociated them). Using a cooling model we can determine how long ago the shock reached this material, and therefore obtain the velocity of the shock.

As in Neufeld et al. (2006b) we can calculate the timescale of the chemical clock from the ortho-to-para ratio. The derived best-fit temperatures, column densities, and ortho-to-para ratios for the W2 aperture are shown in Table 4.5. We also show the sum of the column densities of all states, and separately the smaller value from only states N(4)-N(9), which are all contained in the SL spectrum. The temperatures are quite typical of HH objects, but the ortho-to-para ratio for this aperture is unusually high in the warm component, which suggests that the model does not work well at all in this regime, or that the ortho-to-para ratio of the gas there had already been equilibrated. The flow around the westclump aperture
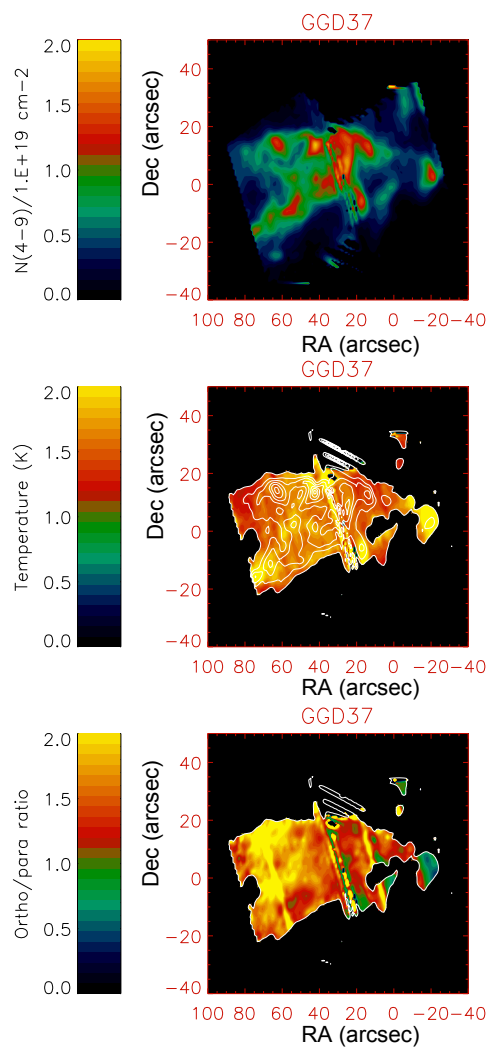
Figure 4.28 Plots of molecular hydrogen column density, temperature, and
ortho-to-para-H$_2$ ratio. The ratio decreases to along the line of the flow to the
northwest.

shows a much more typical ortho-to-para ratio for the warm and hot components. Starting from an OPR of 0.7 and moving to an OPR of 1.5 in the width of one of the bow shocks (roughly 10 arcsec, or 1.04×10^{17} cm), and assuming the slow shock is propagating at 30 km/s, we derive a dynamical timescale of ~ 1100 yr. However because of the low spatial resolution of our map this distance and timescale could be high by up to a factor of 2.

For the wind shock, our five [Fe II] lines in the mid-IR, plus 1.644 μm observed from WIRO (Raines, 2000) provide the opportunity for a multi-component density, temperature, and extinction fit. Using [Fe II] and [Si II] we can back out the total cooling rate (using them as proxies for [O I] at 63 μm). The higher excitation lines ([Fe III], [Ar III], [Ne II], [Ne III], [O IV], [Ne V] in increasing order of excitation energy) indicate the highest temperature reached in the J-shock. The two lines of [S III] trace the density of the high temperature gas.

4.4   Principal Component Analysis of the Maps

Principal component analysis is a statistical method for characterizing a dataset in terms of its strongest correlations in each dimension. By recasting the dataset in terms of its eigenvectors it is possible to isolate the scatter in each component and characterize the system in terms of a "best-fit" in each direction. In the simplest case of a two-dimensional dataset this literally results in a line of best fit along the direction of correlation, leaving only the orthogonal scatter after removing it from the data. This is done in several steps:

First, subtract the mean from each dimension of the dataset. Second, calculate the covariance matrix (the covariance of each dimension with each other dimension in every combination). Third, calculate the eigenvalues and eigenvectors of the covariance matrix. The principal components are the eigenvectors weighted by the eigenvalues of these vectors. The first eigenvalue represents the principal component of the data, the most significant direction of scatter. If we remove the principal component the remaining scatter should be dominated by the second component, and so on until we reach the full complement of eigenvectors equal to the number of dimensions of the dataset. This allows us to peel away the dominant source of the data to discover underlying secondary correlations in our

data.

The are three ways we utilize this technique with the datacube. First, we take a single map, calculate the principal component vector, and overlay it on each map. This will indicate the direction of greatest spread in our data, which should fall along the principal flow axis in most cases. We can calculate this value for each map and determine whether all of the spectral lines appear to flow in the same direction. Second, we determine which portions of the maps correlate with each other as a function of position on the sky. Each principal component is represented as a map of positive and negative correlations. Third, we correlate each map with each other in terms of their contributions to each component – species that contribute similarly to the first few components are similarly distributed. Species that diverge in lower order components are exhibiting structures superimposed on the main flow that may not be obvious from visual inspection of the maps, as we will see.

4.4.1 Analysis of the Principal Component Within Each Map

We applied a principal components analysis program [2] to the datacube, using the maps for each spectral feature. Using this technique we can determine which pixels correlate in each map, which will indicate the dominant direction of positive or negative change in the map. The principal component vector for each map is shown in Figure 4.29.

For each vector the principal component is either parallel or orthogonal to the direction of the flow. But in the case of most of the higher ionization maps, we find the principal component is much more strongly oriented on the SW-NE axis, tracing the higher energy flow running from the approximate location of W2 to a point at the edge of the bow shocks, inside the molecular hydrogen flows. The lower energy molecular hydrogen maps are much more ambiguous and generally are best fit with a directly east-west or north-south flow. The S(0) maps are complicated by the presence of diffuse emission from sources north of the map; the

---

[2]Based on the IDL function "pcomp.pro". See also the Lindsay Smith tutorial on Principal Component Analysis: mail.iiit.ac.in/m̃krishna/PrincipalComponents.pdf.
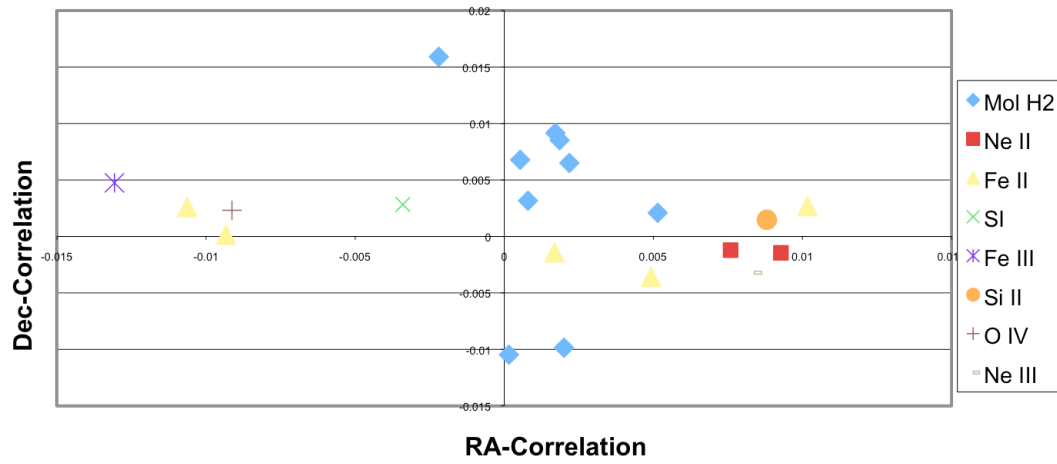
Figure 4.29 Vectors of the principal component of each map; physically this may represent the primary flow direction, as it will track the shallowest gradient. It also may run perpendicular to the flow direction, if the flow is only gently collimated. The molecular lines all show relatively strong positive or negative correlations with declination and only weak correlations with right ascension, while the ionic lines all exhibit strong positive or negative correlations with right ascension and only weak correlations with declination. This immediately suggests that they are morphologically distinct groups.

S(1) - S(7) components consistently exhibit generally westward flows, especially
in comparison to the Fe, Ne, S, and O ionic flows.

4.4.2 Principal Component Analysis of the Correlation Between Maps

The second way to use this technique is to reconstruct the maps by analyzing which
portions of the maps dominate the entire datacube. We can calculate a series of
images of positive and negative "flux", each of which represents the positive and
negative correlations within a given component, and the relative contribution of
each component to the datacube. Thus within each component negative features
correlate with other negative features, and positive features correlate with other
positive features; we learn what portions of the map correlate spatially with each
other. The relative proportions of each component are shown in Figure 4.40. In
these figures, the magnitude of the correlation is less important than the sign;
green and blue regions anti-correlate with red and orange regions.

- In Figures 4.30 and 4.31 we show the correlation analysis run on the entire
  dataset. The dominant correlations all resemble the 32 μm continuum flux.

- In Figures 4.32 and 4.33 we show the correlation of all components observed
  in SH or LH. The first component is an interesting mix. The region around
  W2 is positively correlated with several other locations in the HH 168 flow
  and weakly correlated with the westernmost clump. The split in the flow
  between the SE-NW and the E-W component is clear. The second com-
  ponent shows that the H2 flow is self-correlated and correlated with the
  westernmost clump, but is anti-correlated with the W2 emission.

- in Figures 4.34 and 4.35 we show the correlation amongst the five [Fe II]
  lines. The first and second and fourth components are dominated by the
  5.3 μm map, although they also resemble 35.3 μm. The third component
  shows the strong contrast between the W2 position peak and the rest of the
  SW-NE flow. The fifth component resembles the 35.3 map– it reveals the
  concentric rings of emission spreading out to the sides of the HH 168 flow,
  and indicates that the westernmost clump correlates most closely with the
  outer rings rather than the center of the flow.

- In Figures 4.36 and 4.37 we show the correlation between the SL H$_2$ lines, although the SL artifact is prominent once again. Although most components are similar in appearance, we can begin to see the knotted emission substructure underlying what appears to be a continuous flow, resembling in generality the [S I] map, which is not included in this correlation. The lesser components begin to emphasize the HH 168 flow and show some level of anti-correlation with the upper flow, while in the first few components the two flows are essentially indistinguishable.

- In Figures 4.38 and 4.39 we show the correlation between the higher excitation fine structure lines – those with excitation energies above 16 eV, including [Fe III], [Ne II], [O IV], [Ar III], and [Ne III] (15.5 μm). The components show the anti-correlation of the main W2 peak with the rest of the flow, as well as a weaker series of peaks along the flow. The fifth component indicates an east-west split in the W2 peak.

4.4.3 Ratio of the Principal Components By Chemical Species

Finally we can compare the maps to each other component by component. Figure 4.41 shows the contributions of each species, categorized by broad type (continuum/PAH feature, rotational lines for H$_2$, HD and [S I], lower excitation fine structure lines for Fe and Si, and higher excitation lines for Fe, Ar, Ne, O, and S), for components 1 and 2. Data points that are near each other correlate well with each other in these components. We can see that in components 1 and 2, the rotational line emission and atomic sulfur is quite different than the fine structure lines but there are some notable outliers in detail:

The H$_2$ S(0) line and the [S III] 33.4 μm lines correlate much more closely with the continuum emission rather than with their own groups, which may reflect their origin in the cloud itself rather than tracing the shock. HD R(4) is likely a non-detection, as evidenced here. [Ne V] correlates with the other highly ionized species only in the first component; again the detection may be somewhat suspect. [Fe II] 5.3 μm correlates with the rotational lines; this is probably due to the noisy detection and rising continuum at the short wavelength end of the IRS. [S III] 18.7 μm seems morphologically distinct as well, correlating more closely with the
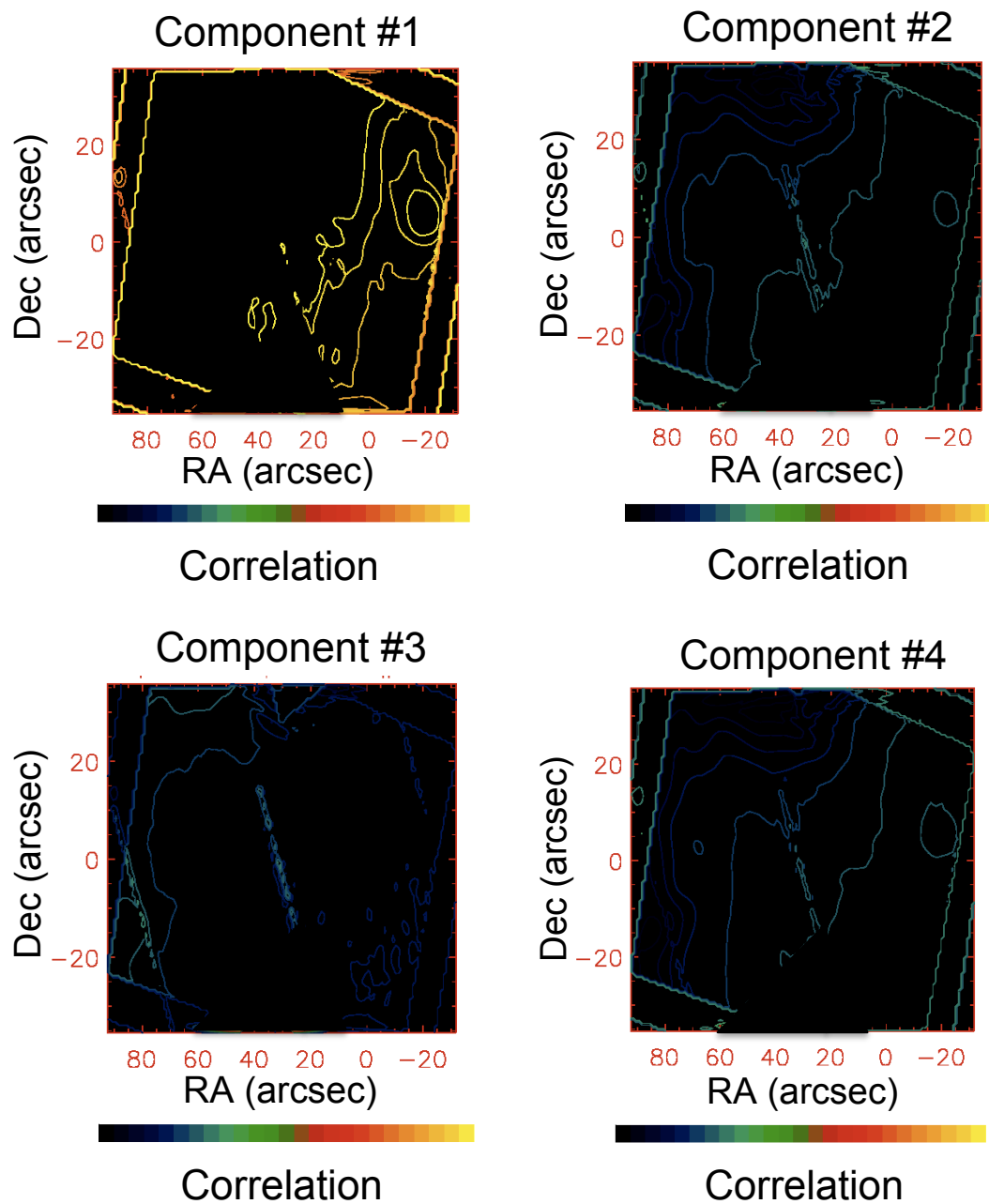
Figure 4.30 Principal components 1-4 using the entire dataset; see next figure for a description.
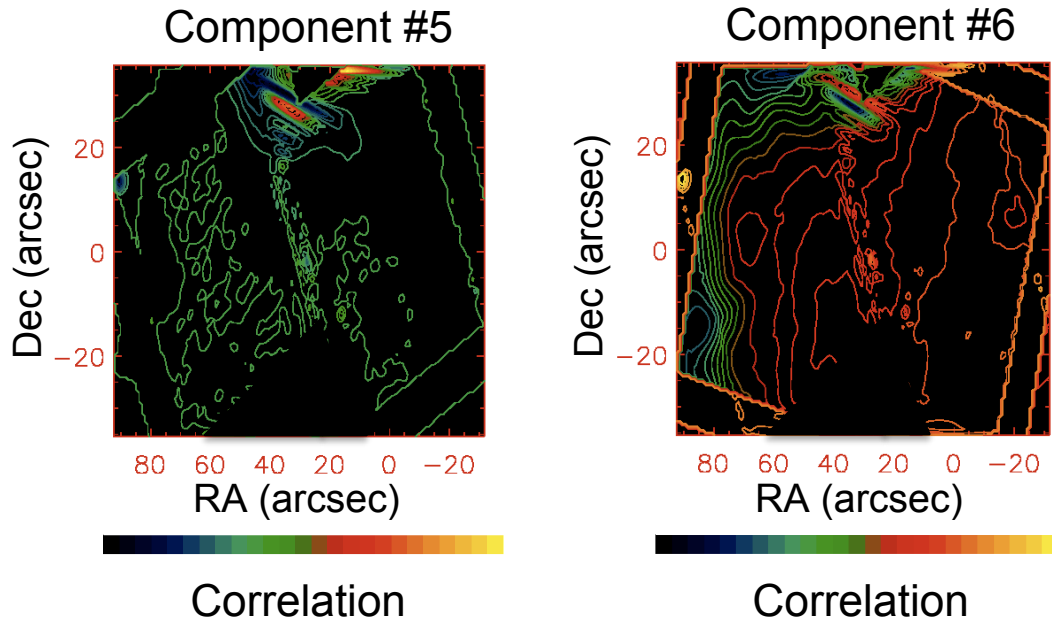
Figure 4.31   Principal component analysis using the entire dataset; components
5 and 6 are displayed in this figure. The components 1-6 are, in descending
order of significance: upper left, upper right, middle left, middle right, lower left,
lower right. SL artifacts dominate many of the principal components; the line of
emission running from (40,20) to (20,-20) is an artifact of the two SL maps pieced
together, and is caused by the S(2)-S(7) line maps. The dominant correlations
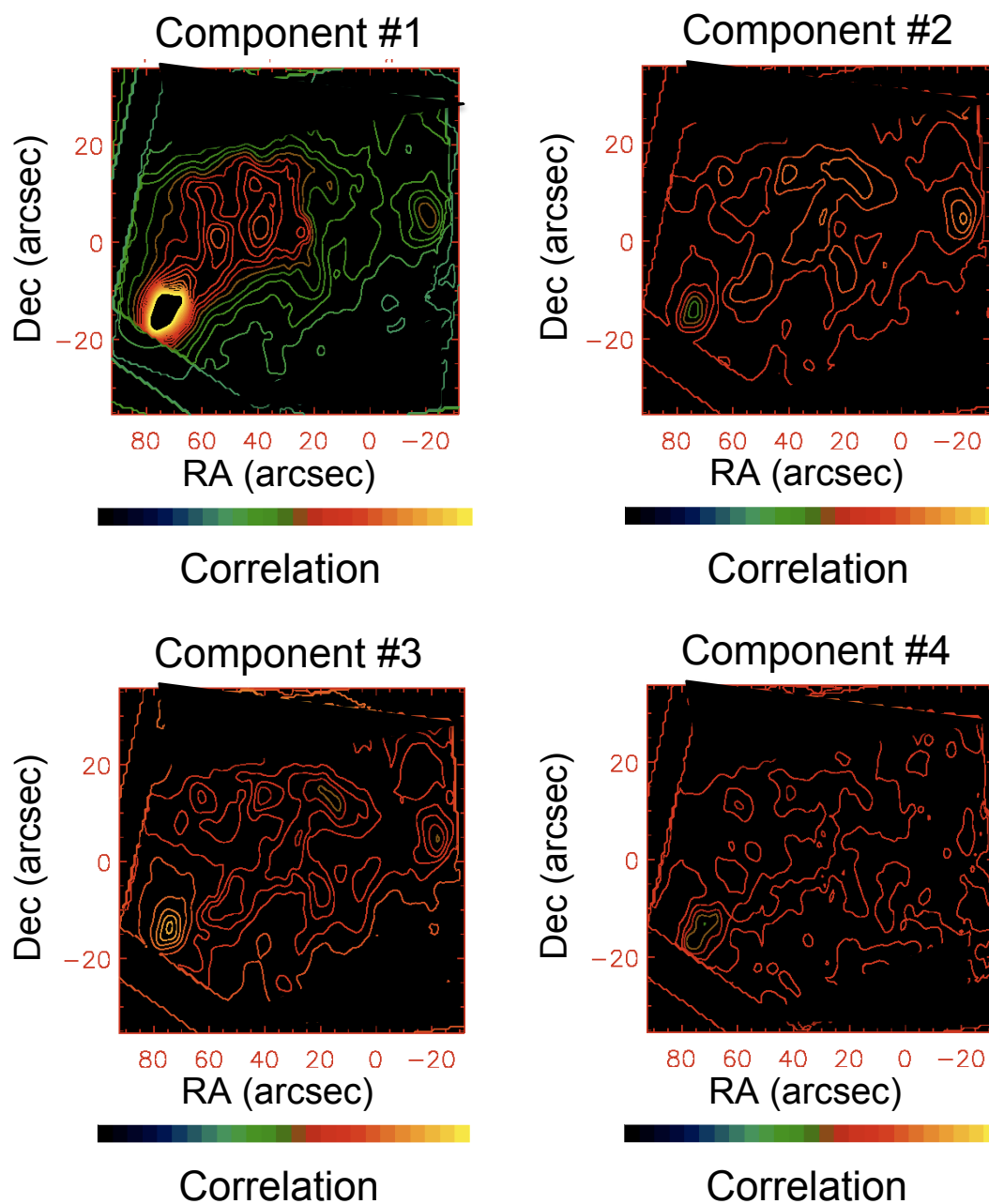all resemble the 32 μm continuum flux.

Figure 4.32   Principal components 1-4 using only the high resolution maps; see next figure for a description.
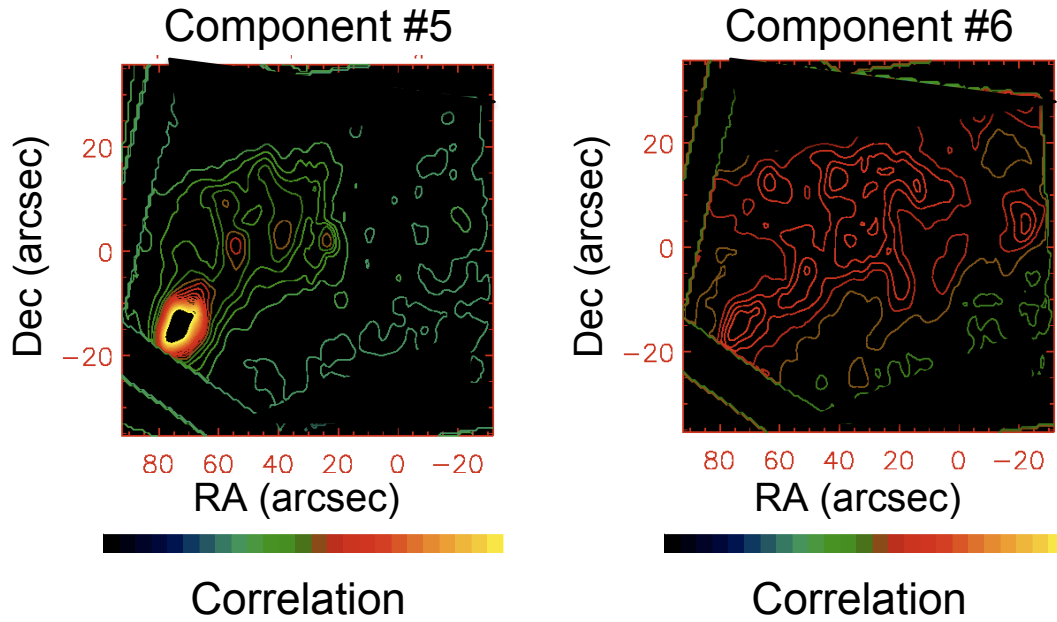
Figure 4.33 Principal component analysis of the high resolution maps; components 5 and 6 are displayed in this figure. The green and blue regions anti-correlate with red and orange regions. The region around W2 is positively correlated with several other locations in the HH 168 flow and weakly correlated with the westernmost clump. The split in the flow between the SE-NW and the E-W component is clear. The second component shows that the H2 flow is self-correlated and correlated with the westernmost clump, but is anti-correlated with the W2 emission.
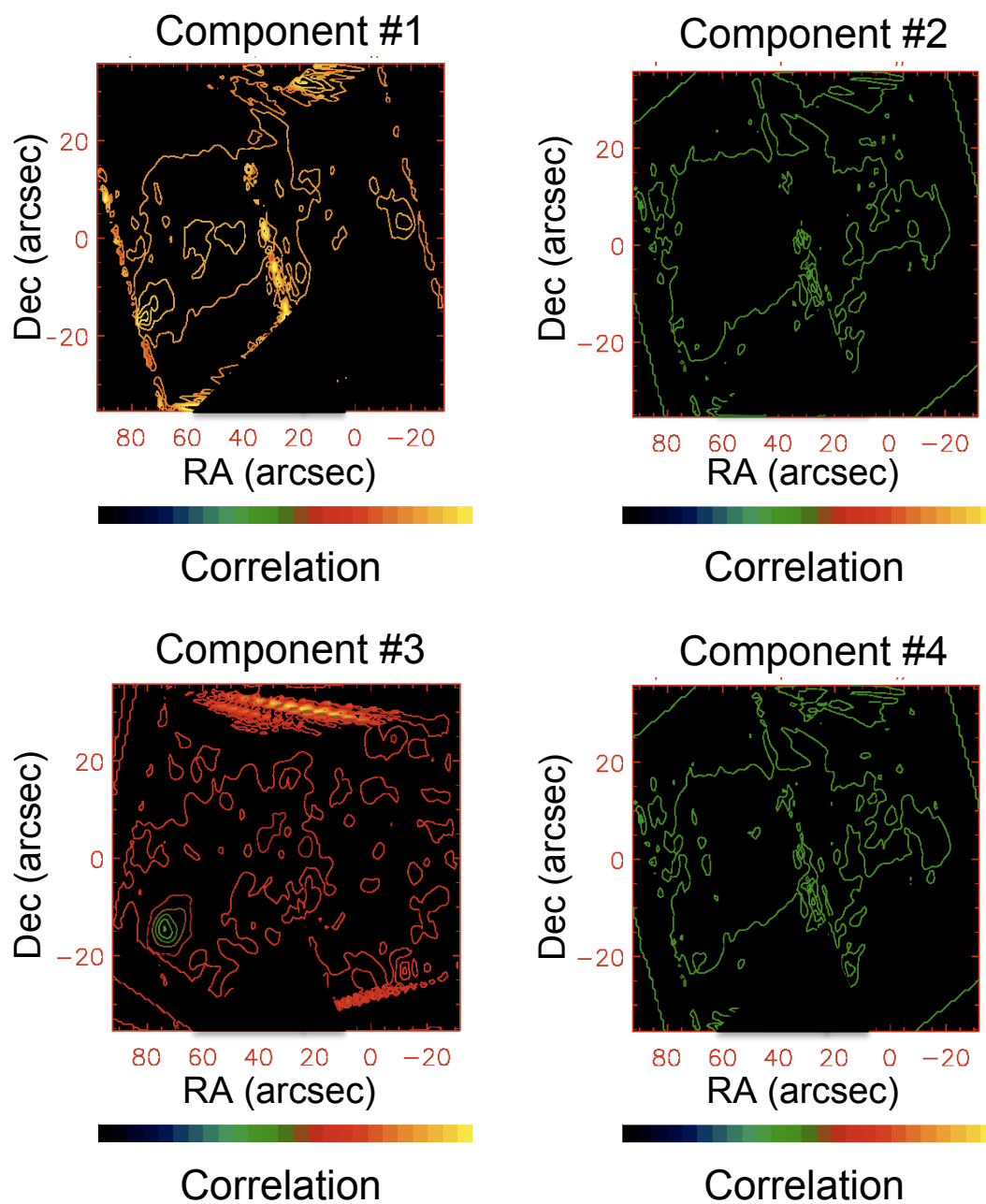
Figure 4.34 Principal components 1-4 using only the Fe II line maps; see next figure for a description.
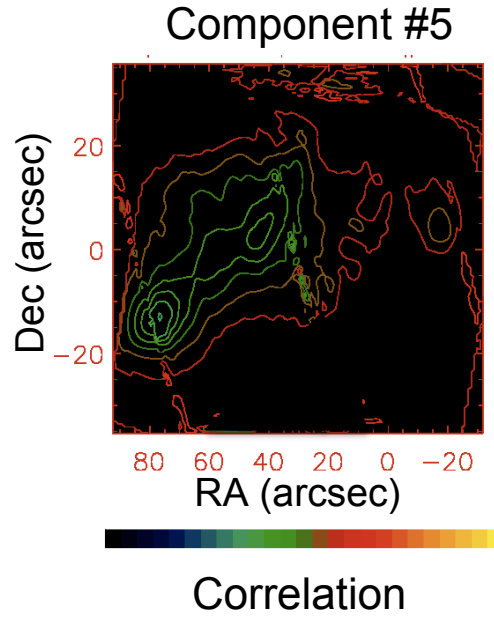
Figure 4.35 Principal component analysis of the [Fe II] lines; component 5 is displayed in this figure. The green and blue regions anti-correlate with red and orange regions. The line of emission running from (40,20) to (20,-20) is an artifact of the two SL maps pieced together, and is caused purely by the [Fe II] 5.3 μm map. The first and second and fourth components are dominated by the 5.3 μm map, although they also resemble 35.3 μm. The third component shows the strong contrast between the W2 position peak and the rest of the SW-NE flow. The fifth component resembles the 35.3 map– it reveals the concentric rings of emission spreading out to the sides of the HH 168 flow, and indicates that the westernmost clump correlates most closely with the outer rings rather than the center of the flow.
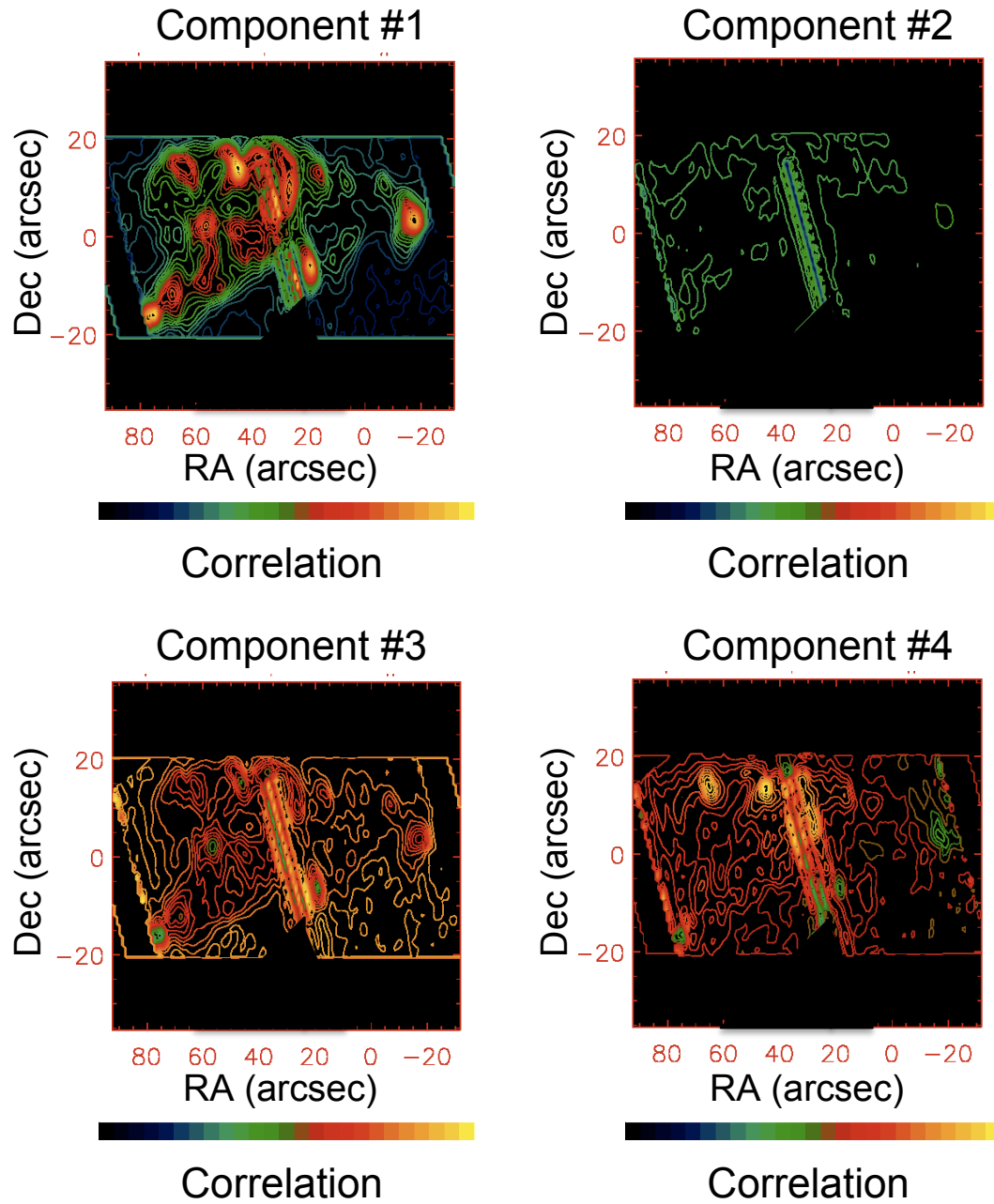
Figure 4.36 Principal components 1-4 using only the molecular line maps; see next figure for a description.
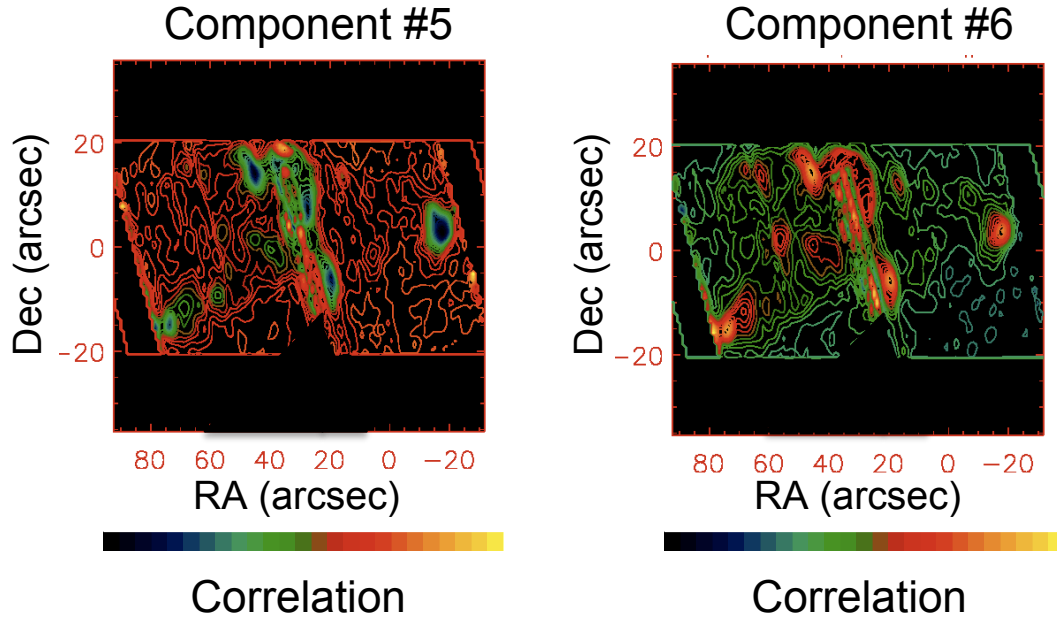
Figure 4.37   Principal component analysis of the H$_2$ lines; components 5 and 6
are displayed in this figure. The top and bottom 20" are masked out to improve
the fit and avoid artifacts, although the SL artifact is prominent once again.
Although most components are similar, we can begin to see the knotted emission
substructure underlying what appears to be a continuous flow, resembling in
generality the [S I] map, which is not included in this correlation. The lesser
components begin to emphasize the HH 168 flow and show some level of anti-
correlation with the upper flow, while in the first few components the two flows
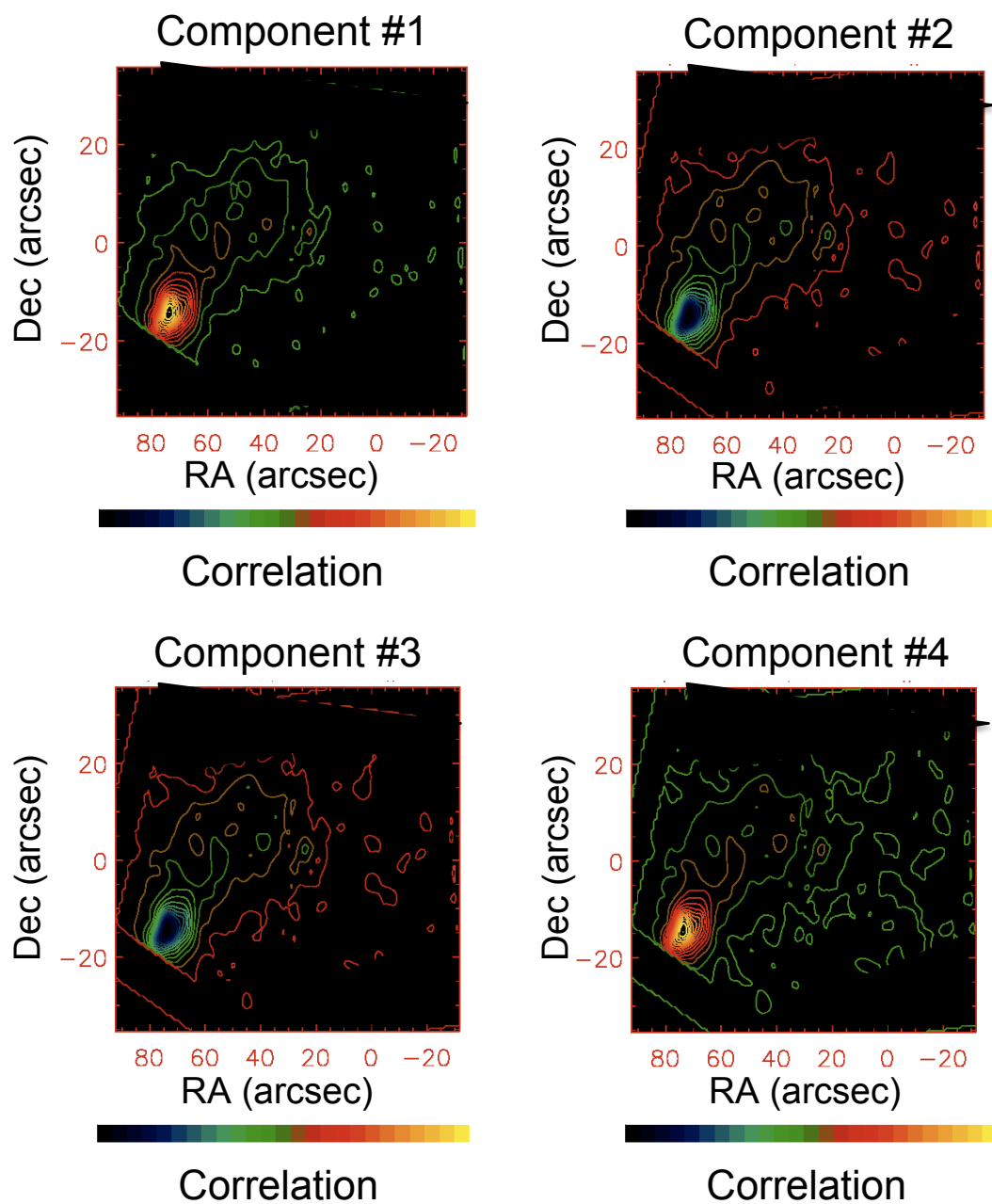are essentially indistinguishable.

Figure 4.38 Principal components 1-4 using only the high excitation line maps; see next figure for a description.
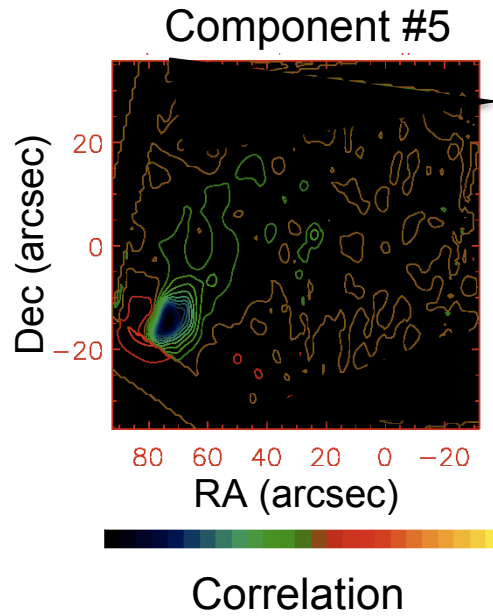
Figure 4.39 Principal component analysis of the high excitation fine structure lines; component 5 is displayed in this figure. The green and blue regions anti-correlate with red and orange regions. In this correlation we only include those lines clearly detected and requiring excitation energies greater than 16 eV, including [Fe III], [Ne II], [O IV], [Ar III], and [Ne III] (15.5 μm). The components show the anti-correlation of the main W2 peak with the rest of the flow, as well as a weaker series of peaks along the flow. The fifth component indicates an east-west split in the W2 peak.

rotational lines than with the ionic lines. [Fe II] 18 μm and [Ar III] appear to be nearly identical in these components.

When we move to a comparison of components 2 and 3, we now more clearly separate out the higher ionization potential lines from the lower, although much of the [Fe II] is still intermingled with the more powerful lines. [Ne V] remains an outlier. The S(5) - S(7) lines now diverge (in different directions) from the S(1)-S(4)/HD/[S I] cluster.

Finally, in a comparison of components 3 and 4, we see clear differentiation between the different groups, except for S(5) - S(7) which remain separate from the rotational lines, and [S III] 18.7 μm, which looks like a lower ionization line.

In summary, we can group the lines into several morphological groups. Group 1 consists of long wavelength continuum samples and PAH emission at 11.3 μm, as a baseline for the molecular cloud itself. Group 2 consists of H_2 S(0) and [S III] 33.4 μm, which closely track the continuum except for component 4 of S(0). Group 3 includes H_2 S(1) - S(4), HD R(3), and [S I], which closely correlate. Group 4 includes H_2 S(5) - S(7), which diverge from the other rotational lines in components 3 and 4. Group 5 consists of [Fe II], [Si II], and [S III] 18.7 μm. Group 6 is the highest ionization potential lines of [Ar III], [Fe III], [Ne II], [Ne III] 15.5 μm, and [O IV]. The [Ne V] detection may be unreliable outside of the first component, and HD R(4) does not seem to be a real detection.

Apparently [S I] does not vary enough to distinguish itself molecular hydrogen in the first four components despite appearing quite different morphologically, very tightly tracking the S(1) emission better than even the other rotational lines do. Because of this correlation, we attribute the [S I] emission in this region to the same exciting source as the molecular (non-dissociative) C-shock, which was also noted in Melnick et al. (2008). Although there are definite differences in the appearance of the [S I] and H_2 maps, we attribute these to density difference rather than a difference in exciting source; the H_2 lines we model in LTE, while the [S I] is not thermalized. Although the critical densities for the H_2 line are 10^4 cm^{-3}, the critical density for electron collisions is 10^6 cm^{-3}, and is sub-thermal. It may be that [S I] is a useful density tracer of low temperature gas, in the absence of the HD R(4) line.
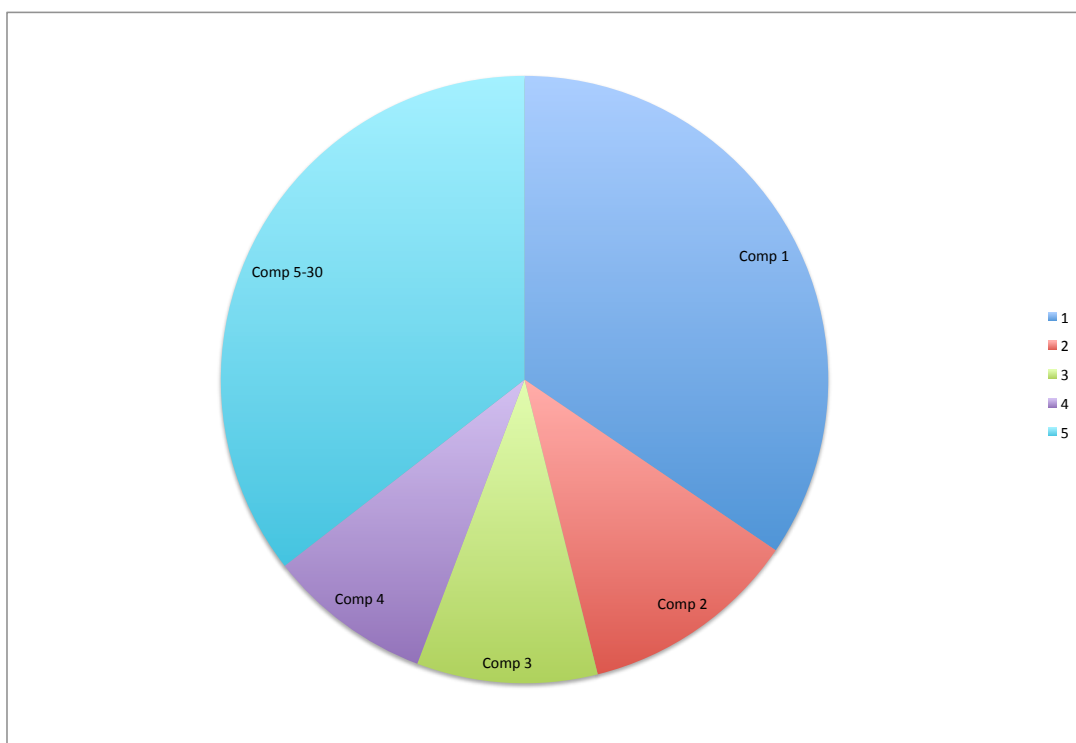
Figure 4.40 A pie chart showing the weighting of the top four principal components.
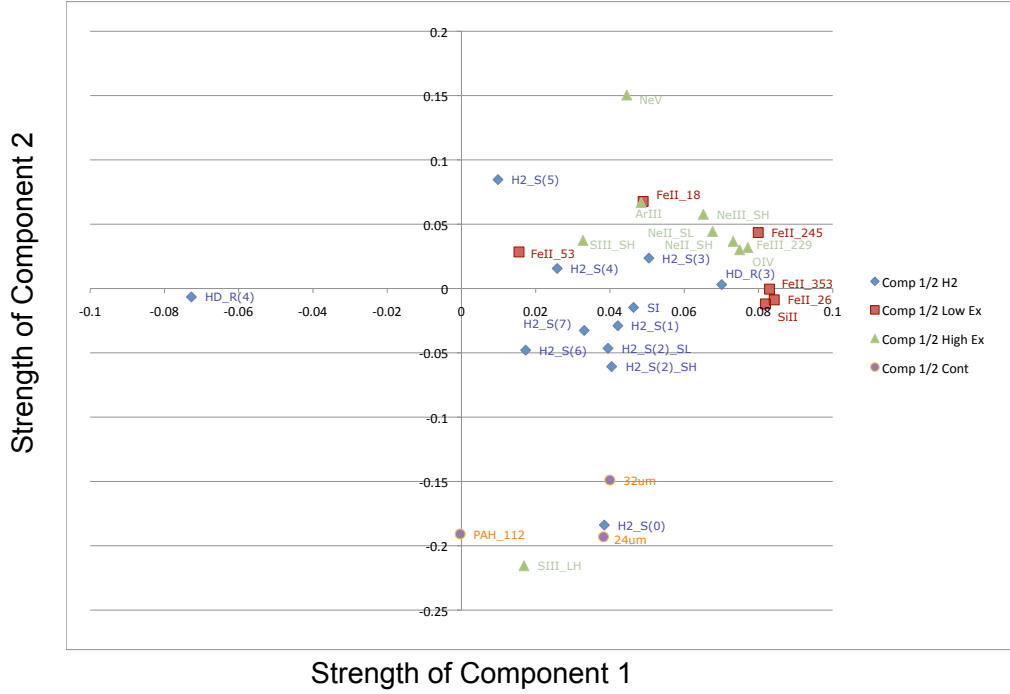
Figure 4.41   Principal component analysis showing the relationship of Component 1 (plotted on the horizontal axis) to Component 2 (plotted on the vertical axis) for every species, grouped broadly by excitation energy and labeled by chemical species. The scale of the axes is the normalized eigenvalue for each line, representing the contribution of each line to the components.

4.4.4   Emission from Singly-Ionized Iron

We applied our temperature/density/extinction model as described earlier to the five mid-IR lines of [Fe II] and the 1.644 μm line observed by Raines (2000), using the Pradhan & Zhang (1993) model. The fits are reproduced in Figures 4.47, 4.48, and 4.49.

We began by fitting only the temperature and electron number density with no extinction, then varied the extinction as a fixed parameter with $A_V = 0$, 1.55, 3, 5, and 10. Fits for $A_V \gtrsim 3$ were unable to achieve fits with low χ^2 values for number density, and a constant value of A_V between 0 and 3 produced similar morphologies for temperature and density within the region of detectable [Fe II]

Figure 4.42 Principal component analysis showing the relationship of Component 2 (plotted on the horizontal axis) to Component 3 (plotted on the vertical axis) for every species, grouped broadly by excitation energy and labeled by chemical species. The scale of the axes is the normalized eigenvalue for each line, representing the contribution of each line to the components.

Figure 4.43 Principal component analysis showing the relationship of Component 3 (plotted on the horizontal axis) to Component 4 (plotted on the vertical axis) for every species, grouped broadly by excitation energy and labeled by chemical species. The scale of the axes is the normalized eigenvalue for each line, representing the contribution of each line to the components.

Figure 4.44 Principal component analysis showing the relationship of Component 1 (plotted on the horizontal axis) to Component 2 (plotted on the vertical axis) for every species, grouped broadly by excitation energy. The scale of the axes is the normalized eigenvalue for each line, representing the contribution of each line to the components.
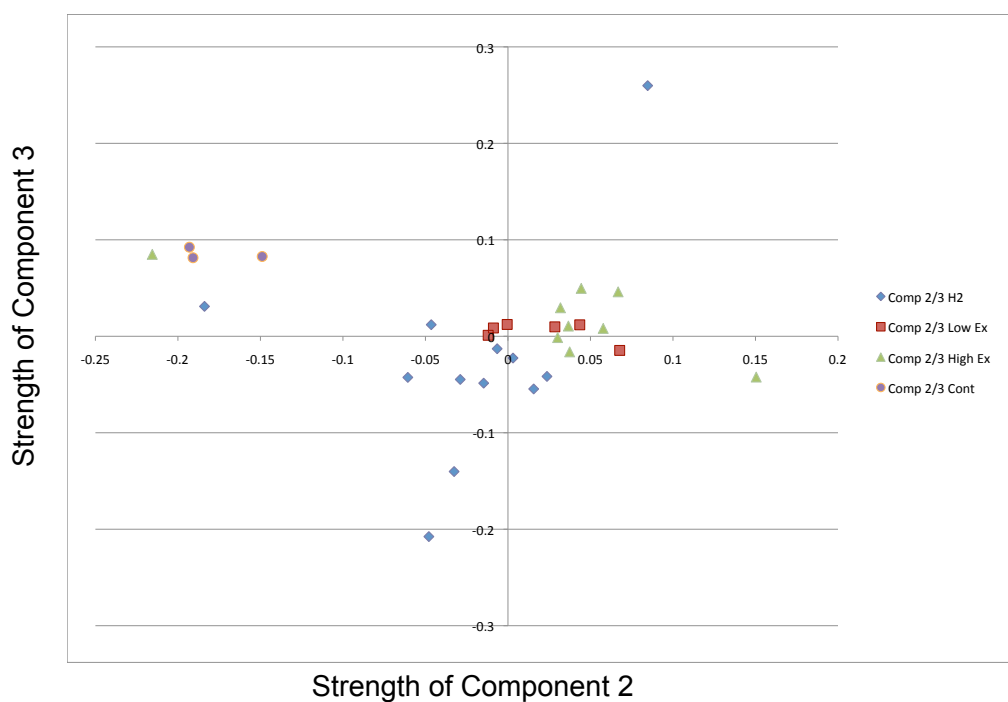
Figure 4.45   Principal component analysis showing the relationship of Component 2 (plotted on the horizontal axis) to Component 3 (plotted on the vertical axis) for every species, grouped broadly by excitation energy. The scale of the axes is the normalized eigenvalue for each line, representing the contribution of each line to the components.
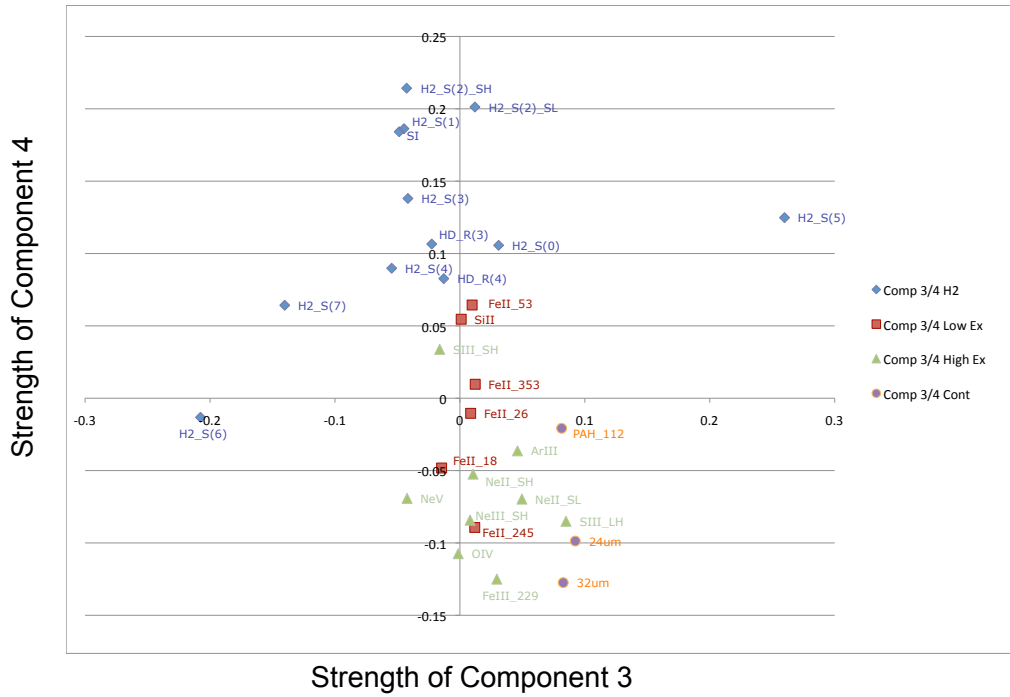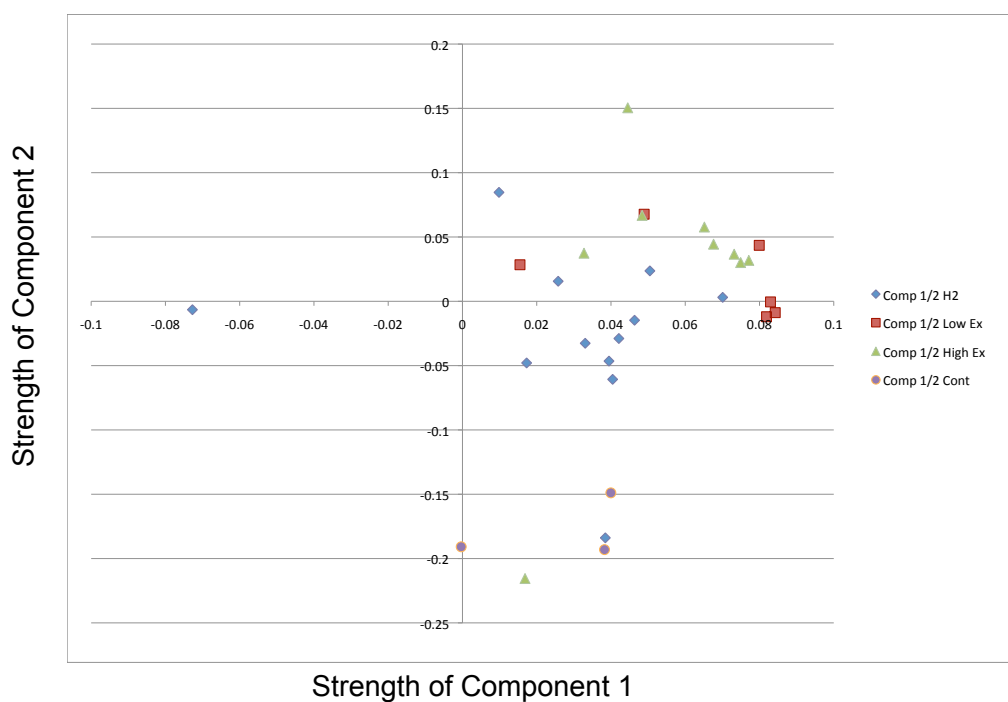
Figure 4.46 Principal component analysis showing the relationship of Component 3 (plotted on the horizontal axis) to Component 4 (plotted on the vertical axis) for every species, grouped broadly by excitation energy. The scale of the axes is the normalized eigenvalue for each line, representing the contribution of each line to the components.
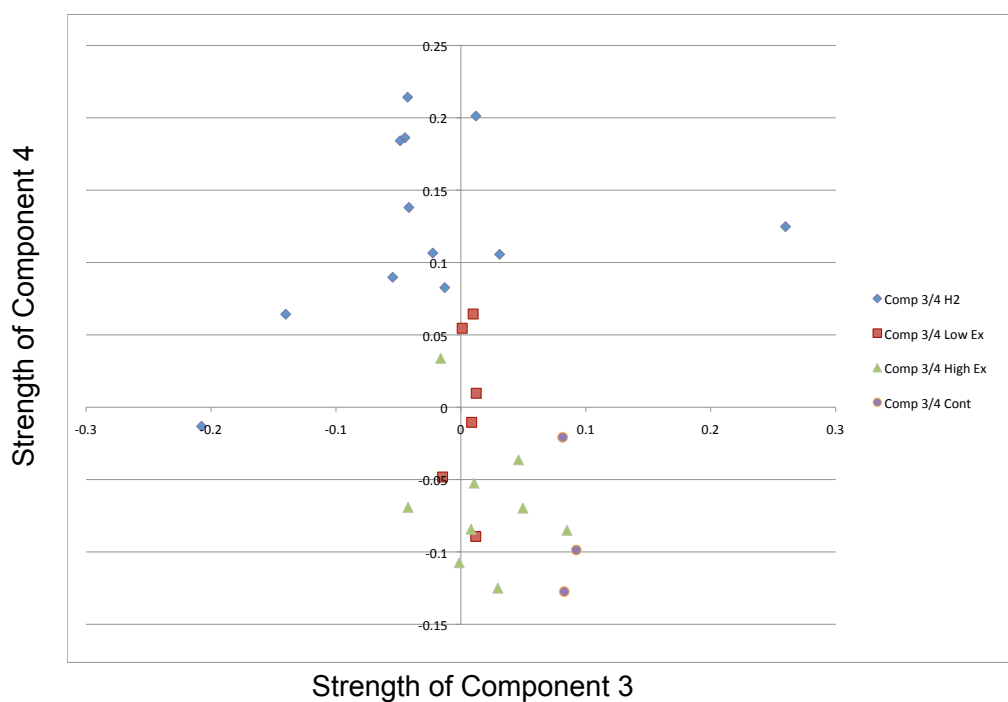
emission (as shown in the figures). Finally we produced a fit varying all three parameters. The results are shown in Figures 4.47, 4.48, and 4.49.

The temperature, number density, and extinction are unsurprisingly highest at the region around W2, with a secondary peak near the shockfront region. We found that the extinction was quite low, ranging from 0 to 1.5 visual magnitudes. As a result we decided to run fits with $A_V = 1.5$ as a fixed value, in order to narrow the parameter space. The extinction plot was gained by varying all three parameters, while the temperature and density plots are the result of the two-parameter fits. The outlier in most of our fits was [Fe II] at 5.3 μm; as we are unsure of blending with the S(7) line, we excluded this line from the final fit.

4.4.5 Emission from Doubly-Ionized Sulfur

We can perform a similar fit to the two lines of [S III] and the two lines of [Ne III]. There are significant morphological differences in these maps. The [S III] 18.7 μm map shows a peak at W2 but very little structure outside of it, although there is a greater concentration in the eastern half of the map. By contrast the 33.4 μm line exhibits a rising flux to the NE and more closely resembles the 24 and 32 μm continuum maps. This suggests that that the 18.7 μm emission originates from the high velocity flow while the 33.4 μm emission traces something in the cloud material. The ratio of these maps is shown in figure 4.50. [Ne III] is not clearly detected at 36 μm and the map is dominated by noise; as such we have not fitted this pairing.

Using A-coefficients derived from Watson (1985, and sources therein) and collision strengths from Galavis et al. (1995) we can calculate the same temperature and density plots for the higher excitation gas. The flux ratio is highly insensitive to temperature (the spontaneous emission is constant to within a factor of ~ 2 over the range of temperatures from 5000 - 15000 K). As such we fit only for number density, holding the temperature at a constant 10000 K, and the result is shown in 4.51. The highest concentration is once again located over W2, but this high excitation gas follows a track quite different from the high excitation flow we have been suggesting. Instead it is densest on the eastern half of the map, as we might expect given the morphological differences between the two [S III] lines that we noted earlier. Although the [S IV] line at 10.5 μm is undetected, it is
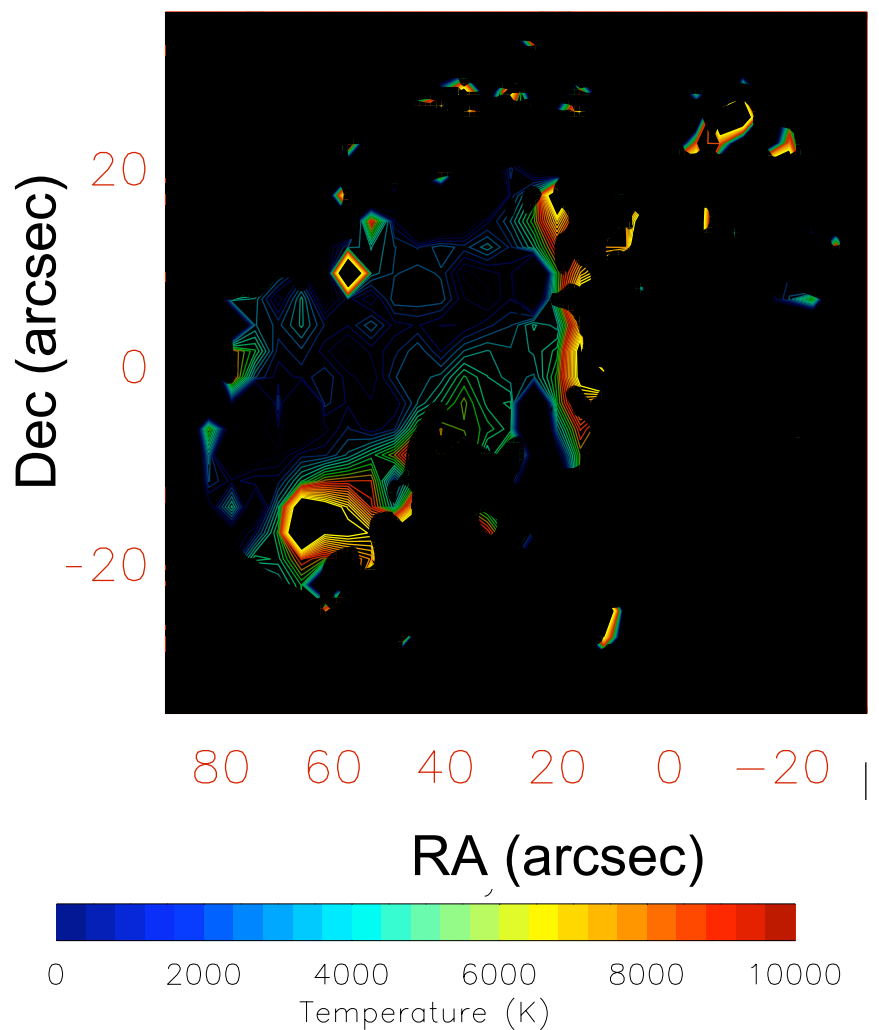
Figure 4.47 Temperature fit to the flux ratios of the five mid-IR [Fe II] lines plus the H-band line. The unmasked area is the section of the map with the best signal in [Fe II]. The temperature peaks at 20000 K near W2, and the flow temperatures are a few thousand K along the principal axis of HH 168, falling off to colder values to the north of the flow.
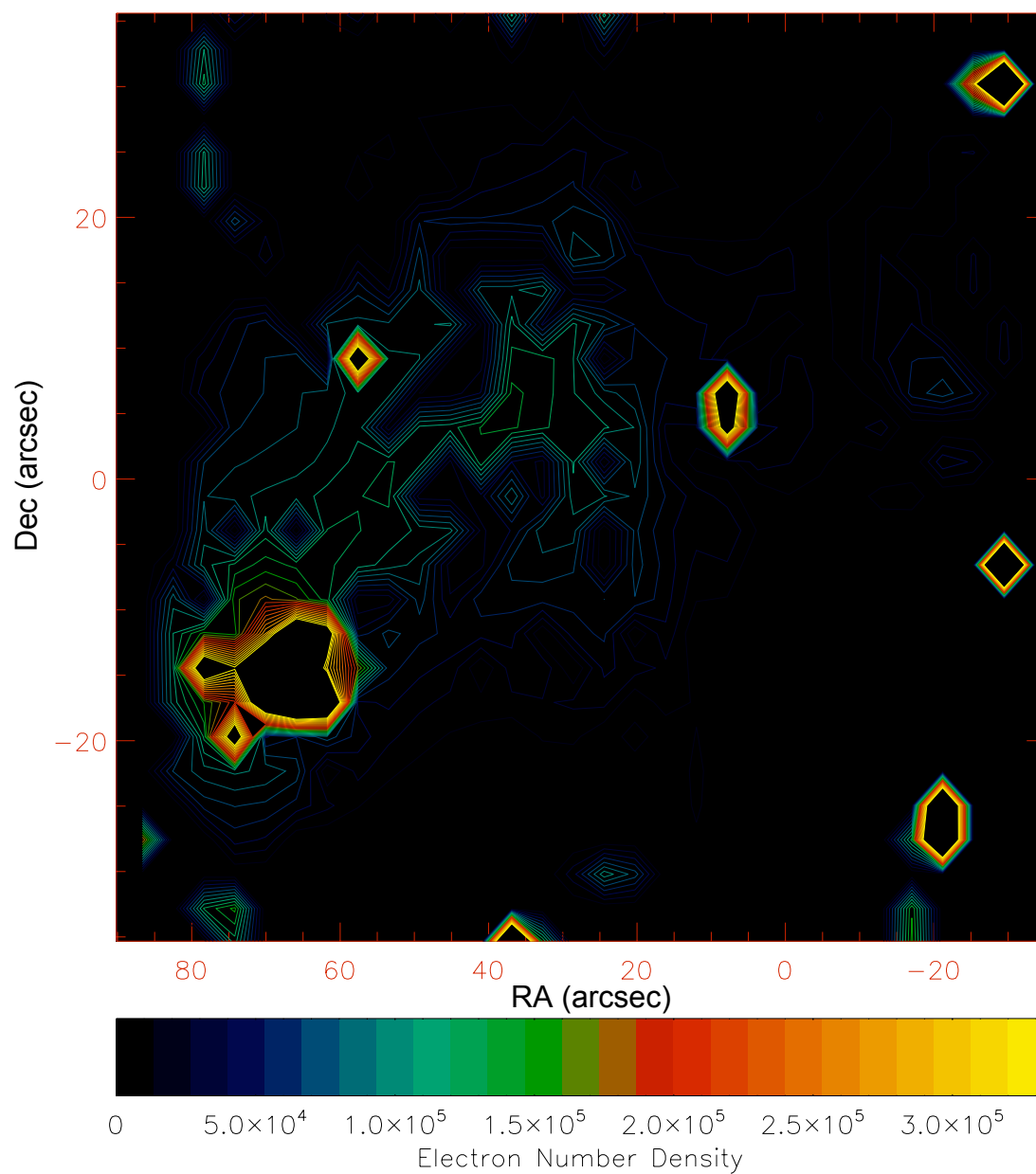
Figure 4.48 Number density fit to the flux ratios of the five mid-IR [Fe II] lines plus the H-band line. The number density peaks strongly around W2; the other regions of high density are spatially coincident with the ionized flow.
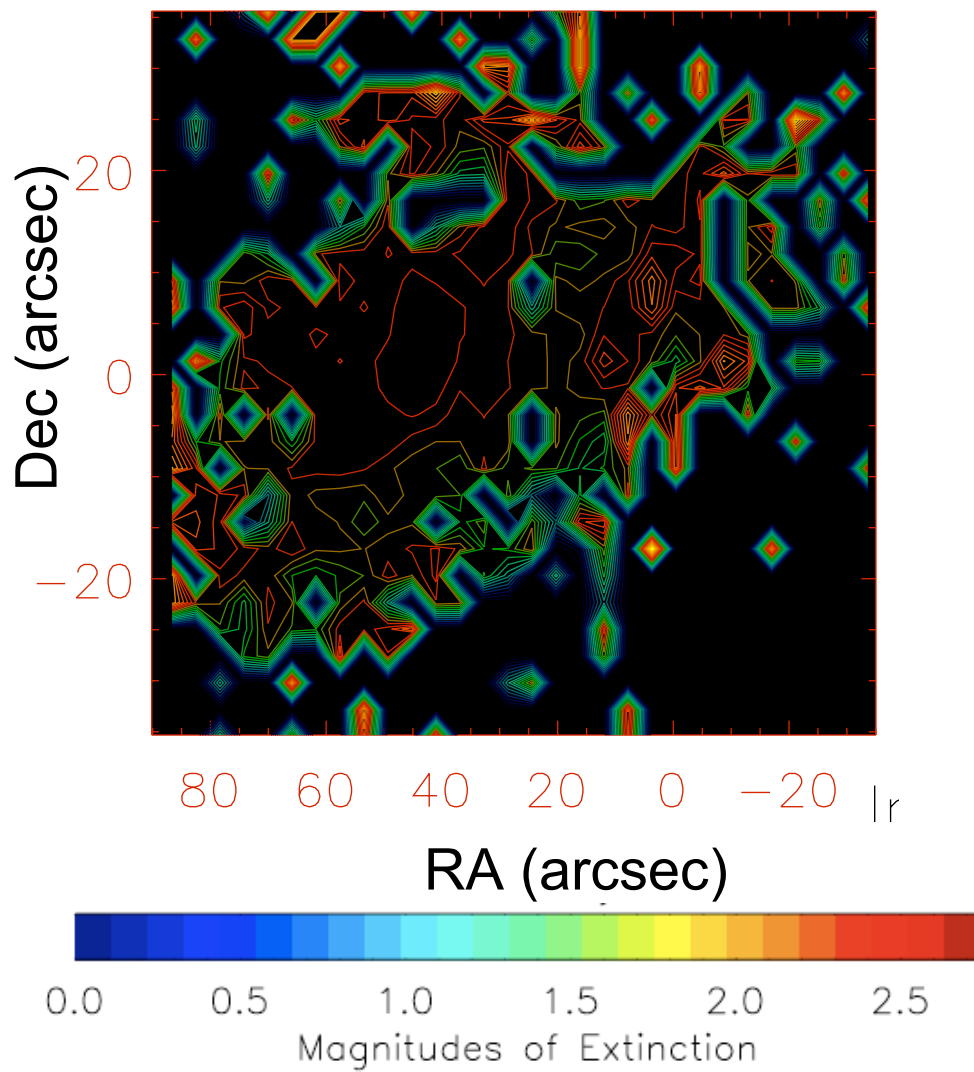
Figure 4.49   Visual extinction fit to the flux ratios of the five mid-IR [Fe II] lines plus the H-band line. The extinction varies between 0.5 and 2 magnitudes, highest to the north of the main flow.
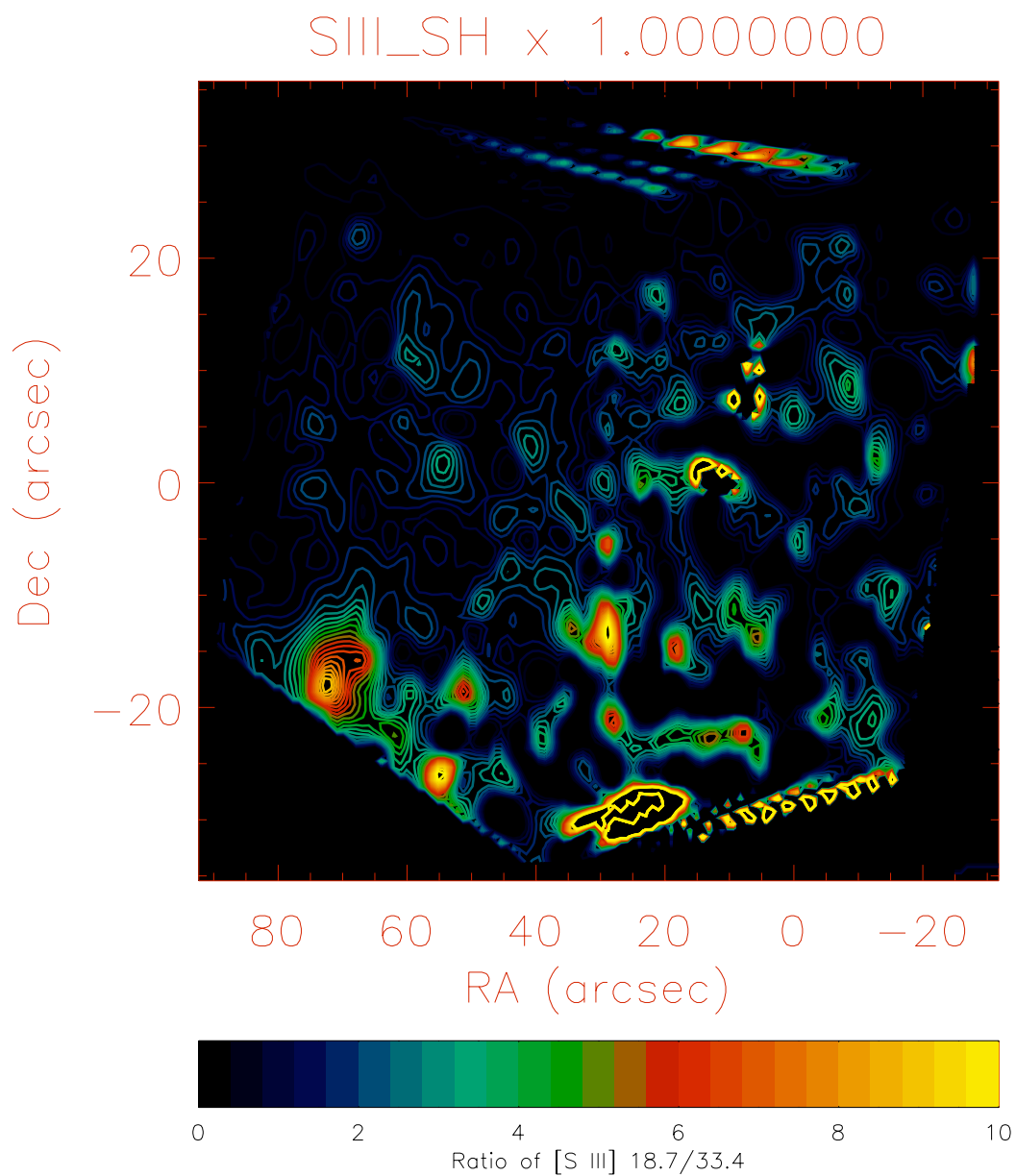
Figure 4.50   Ratio of [S III] 18.7/33.4 μm.

predicted to appear at 5-15% of the flux of the [S III] line at 18.7 μm (Groves
et al., 2008) for the observed [Ne III]/[Ne II] flux ratio of 0.2-0.5. In this survey
AGN typically exhibit much higher [S IV]/[S III] ratios; although the [S IV] is
undetected, the [Ne III]/[Ne II] ratio appears typical of a photoionized galactic
HII region in their figure 1a.

The derived number density n_e is $\sim 2.5 \times 10^4$ cm^{-3} in the dense region around
W2. The [Fe II] μm is very similar to the [Si II], which is expected in all J-shock
models. Over the range of the Hollenbach & McKee (1989), both [Fe II] and [Si
II] can be good proxies for the true cooling line, [O I]. Nonetheless the presence
of [Si II] and [Fe II] ground-state fine-structure lines are signatures of J-shocks.

4.4.6   Shock Models

The type of shock (C- or J-type) depends critically on shock speed, preshock
density, preshock ionization, and the magnetic field strength in the region. The
preshock gas may be irradiated by photons from hot shocked gas on the far side
of the interface, or by ions that run ahead of the shock (if the ions and neutrals
are not coupled); in this case the shock is preceded by a radiative or magnetic
precursor, respectively. This may heat and even ionize the preshock gas, exciting
molecular hydrogen emission. The J-shock front will be characterized in any case
as the area of highest excitation– tracked in this case by the presence of the Group
6 lines: [Ne II], [Ne III], [Ar III], [O IV], and [Ne V], although the lower excitation
lines of Group 5 likely also trace the J-shock boundary.

In the shock transition itself, the material is compressed by a factor of $\sim$ 4-8,
and the flow velocity is decreased by a factor of $\sim$ 4 as well. This is followed
by a radiative zone, where the hot postshock gas radiates and cools, compressing
further (PV $\sim$ T, and at constant pressure).

As in Maret et al. (2009) we can determine whether a typical cloud core would
be unbound by the passage of such a powerful shock. For a typical core mass of
$\sim$ 300 M$_\odot$ and a radius of 0.27 pc, the binding energy is $\sim 1.4 \times 10^{46}$ ergs.

If the cooling were accomplished purely by the non-dissociative C-shock , we
would calculate the total cooling luminosity from the sum of the H$_2$ rotational
modes, as the lines are optically thin. This is shown in Table 4.6; we derive a
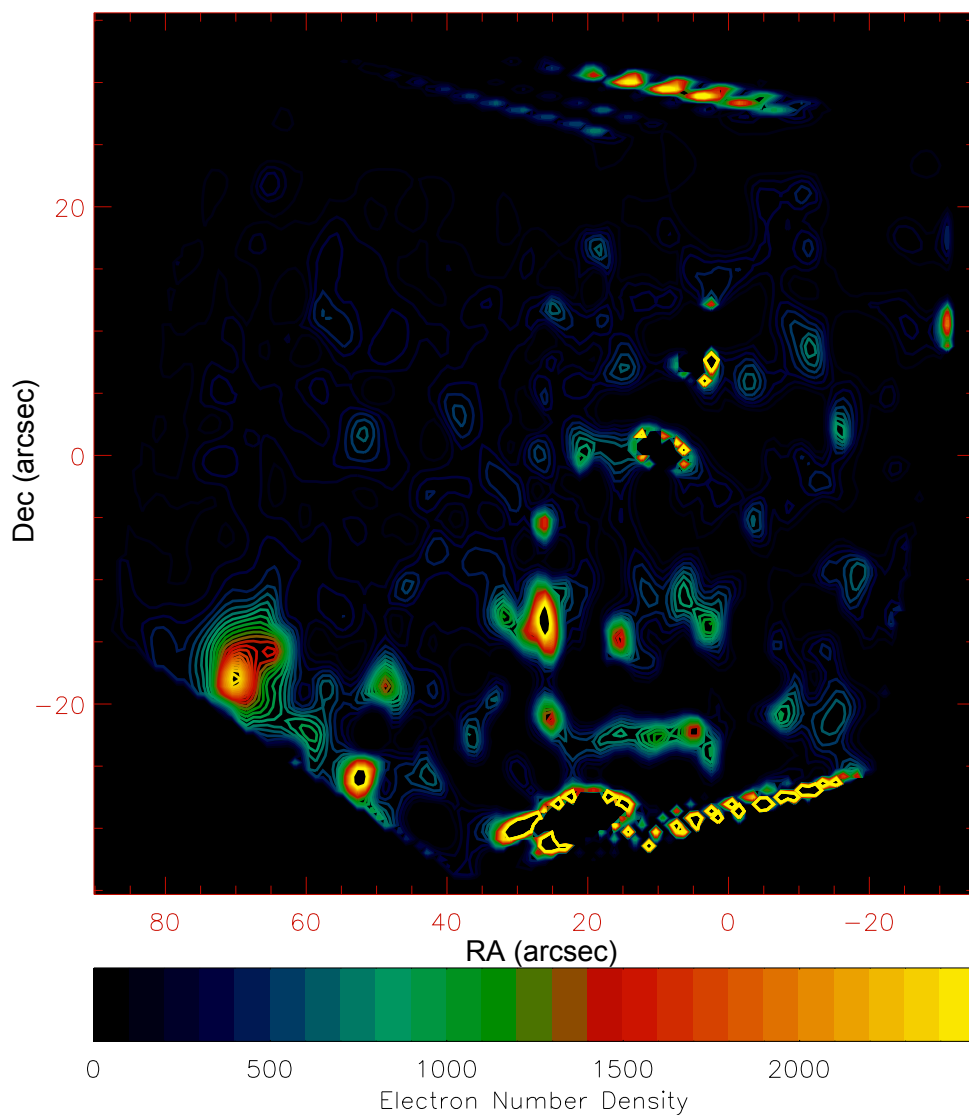total luminosity of 1.8 L$_\odot$ from H$_2$.

Figure 4.51 Density fit to the flux ratio of the 18.7 and 33.4 μm [S III] lines, representing the higher excitation gas. Most of the structure to the southwest lies at peaks in the [S III] 18.7 μm map, which does not appear to be as well calibrated as the 33.4 μm map.

Table 4.6.   Luminosity from H_2

Wavelength of H_2 (μm)	Luminosity ($L_\odot \times 10^{-2}$)
H_2 S(0)	1.32
H_2 S(1)	3.16
H_2 S(2)	9.15
H_2 S(3)	34.79
H_2 S(4)	25.62
H_2 S(5)	61.27
H_2 S(6)	19.07
H_2 S(7)	25.08
H_2 Total	179.48

Note. — Luminosity from cooling via molecular emission.

This is a very luminous flow compared to, for example, the flows in NGC 1333, the brightest of which is HH 7, at 0.111 $L_\odot$. (Although GGD 37 emits only slightly more flux, it is estimated to be over three times more distant.)

This would indicate a mass loss rate, via the kinetic energy:

$$L_{tot} \; = \; \frac{1}{2}\dot{M}v_s^2 \tag{4.12}$$

and therefore

$$\dot{M} \; \sim \; 10^{-6}\frac{1}{f_c}(\frac{L_{H_2}}{0.01 \; L_\odot})(\frac{v_s}{10 \; km/s})^{-2} \; M_\odot \, yr^{-1} \tag{4.13}$$

Assuming a shock velocity of 30 km/s (Hartigan et al., 2000), the mass flow for HH 168 is then $\sim 2.4 \times 10^{-5}$ $M_\odot$ yr^{-1}, yielding a momentum driving rate of 7.2 $\times 10^{-4}$ km/s $M_\odot$ yr^{-1}. The infall rate for the driving source would be 2.4×10^{-4} $M_\odot$ yr^{-1} assuming the canonical factor of ten difference between infall and outflow (e.g. Kurosawa et al., 2006), very high but still within the realm of possibility for an intermediate mass protostar like HW3c, which exhibits a luminosity in excess of 10000 $L_\odot$.

We can check this value with an independent diagnostic from the shock models in Hollenbach & McKee (1989). In the absence of [O I] 63 μm fine structure emission lines (which can be observed in the near future using Herschel-PACS), we can use the [Fe II] lines (which are also optically thin) as a proxy for the

Table 4.7. Luminosity from [Fe II]

Wavelength (μm)	Luminosity (L$_\odot$ $\times$ 10^{-2})
[Fe II] 1.644	18.89
[Fe II] 5.3	14.18
[Fe II] 17.9	3.15
[Fe II] 24.5	0.70
[Fe II] 26.0	5.19
[Fe II] 35.3	1.06
[Fe II] Total	43.20

Note. — Luminosity from cooling via [Fe II] fine structure emission.

total cooling rate. [O I] is proportional to the total mass flow through the shock boundary ($n_0 v_s$) by a factor of 10^{-13} in cgs units, and for fast shocks the [Fe II] (26 μm) / [O I] (63 μm) ratio is $\sim$ 0.05. Using the aperture around W2 the expected flux density of [O I] would be $\sim 2 \times 10^{-4}$ erg/s/cm^2/sr, and the resulting mass flow rate is 10^9 n_0 v_s. Assuming a fast shock velocity of 100 km/s, and a density of 2×10^4 /cm^3, the mass flow rate is 2×10^{18} grams/second, or 3.3×10^{-8} M$_\odot$ yr^{-1}.

If instead we perform the same calculation with [Si II] (34.8 μm), we assume the ratio of [Si II]/[O I] $\sim$ 0.05, and the mass flow is 5.4×10^{-7} M$_\odot$ yr^{-1}. The models predict that [Fe II] and [Si II] should exhibit similar flux at densities of 10^4 /cm^3, but while they are morphologically similar as indicated in the PCA analysis, the [Si II] flux is a factor of 3-20 times higher. This may reflect the differing critical densities, or that the shocked medium contains a high ratio of Si to Fe.

We can calculate the total luminosity from the [Fe II] lines (see Table 4.7). We derive a total flow luminosity of $\sim$ 0.43 L$_\odot$. Interestingly we derive a similar luminosity from H$_2$ and from [Fe II] in this case. In order to unbind a core, the flow would need to remain at this level of intensity for $\sim$ 200 yr.

We can calculate the total momentum injected into the medium as a result of the flow:

$$p = \frac{dp}{dt} t_{dyn} = 0.44 \text{ M}_\odot \text{km/s} \tag{4.14}$$

where t_{dyn} is the dynamical time. We can estimate t_{dyn} by assuming a shock velocity of $\sim$ 100 km/s. If we assume the W1-W2-W3 complex is the progenitor of the shock, then the shocked region spans $\sim$ 80 arcsec, or 0.27 pc; thus the dynamical time is $\sim$ 3000 yr. This yields 0.41 $M_{\odot}$ km/s. If we assume the driving source is HW3c, then the dynamical timescale is closer to 8000 yr, and our estimate adjusts to 1.1 $M_{\odot}$ km/s. Therefore by the time the shock dissipates to the sound speed of the medium (a few km/s), if sustained at this level for 10^4 years, it will have entrained $\sim$ 43 (or 110, if the driving source is HW3c) $M_{\odot}$. The total energy dissipated of the lifetime of the flow to this point is then 8.2 $\times$ 10^{44} erg, which could dissipate a cloud core of up to 30 $M_{\odot}$; the flow appears to be just slightly too weak to dissipate its natal cloud, as it has entrained slightly more material (43 $M_{\odot}$) than this already.

This outflow is consistent with those in NGC 1333 – Maret et al. (2009) derived values of P $\sim$ 0.1 - 0.6 $M_{\odot}$ km/s. The total energy of the flow is L_{H_2} + L_{FeII} / f_c $\sim 5 \times 10^{45}$ ergs. Thus if the progenitor core contains 300 $M_{\odot}$ of material and the outflow lasts for 10^4 yr at this high rate, the binding energy of the stellar core ($\sim$ 1.4×10^{46} ergs) is marginally greater than the energy from this flow.

If a cloud core is gravitationally bound and in hydrostatic equilibrium (ie. without turbulence), it must overcome the thermal pressure in order to collapse. The relationship between the mass and radius of the cloud is (e.g. Hartmann, 1998):

$$\frac{GM_{cl}}{R_{cl}} = \frac{kT}{m_H} \qquad (4.15)$$

For a temperature T of $\sim$ 50 K, a 300 $M_{\odot}$ core would have a radius of 3.1 pc. The binding energy would then be 2.2 $\times$ 10^{52} erg, safely out of the range of disruption by this flow.

4.4.7   Is W2 the driving source for HH 168?

The southern flow of HH 168 is markedly different than the northern flow; the higher excitation species appear only in the southern flow (Figure 4.15). This suggests that the flows may originate from different sources. The northern flow is pointed away from the region of HW2, while the southern flow (traveling to the

northwest) is angled more toward HW3c. As suggested by (Hartigan et al., 1986), the driving source for the HH 168 flow must be located to the east in order to account for the polarization of the reflection nebulae.

The continuum spectrum rises at long wavelengths in the region around W2; at first glance this would seem to be evidence for the presence of a local drive source for the HH 168 flow, suggested to be HW3c by Cunningham (2006); Rodríguez et al. (2005). Upon closer inspection the excess continuum emission at long wavelengths is an extended feature of the map as well, so although a protostar could be contributing to this flux, the excess and longer wavelengths appears to be dominated by the dust, heated externally and re-radiating at longer wavelengths.

4.4.8   On the Nature of W2

Originally detected as a radio emitter by Hughes & Wouterloot (1982) and resolved into three separate components (W1, W2, and W3) by Hughes (1989) using VLA data, W2 is a prime candidate for a high mass protostellar object driving a northwest outflow (Garay et al., 1996). The edge of the HH 168 flow is approximately located at Source S as defined in Hartigan & Lada (1985), and the W2 and S locations coincide with a line of soft x-ray emission (Pravdo & Tsuboi, 2005), as well as velocity-resolved [O III] (5007 nm) emission in the case of Source S (Hartigan et al., 1986). (Pravdo & Tsuboi, 2005) identify W2 and S as separate exciting sources for soft x-rays, although they observe significant emission from the line connecting the two as well, and the [O III] is resolved to be moving at speeds of ~ 420 km/s.

This region exhibits extremely high excitation spectral lines, in excess of 97 eV. The ratio of [Ne II]/[Fe II] peaks in vicinity of W2 at 10-20 – which is extreme by comparison to other flows such as HH 54, which exhibits ratios of ~ 0.6, or HH 7-11, which does not have any detectable [Ne II] emission (e.g. Neufeld et al., 2006b) – although the ratio falls to ~ 1 - 5 away from W2 along the flow. The [Ne III]/[Ne II] ratio is ~ 0.2-0.5 in this region, gradually falling off to the west before peaking slightly again at the edge of the flow, although it should be noted that this may be confused by separate excitation mechanisms. Ne ions are produced in T-Tauri disks by X-ray absorption in the warm disk, and the recombination of Ne ions is slow: in the case of [Ne III] because of weak charge transfer with

HI, and in the case of [Ne II] because of virtually nonexistent charge transfer (Glassgold et al., 2007). This is of considerable importance in analyzing [Ne II] in protoplanetary disks; in this case because we observed that the [Ne III] and [Ne II] morphology are so similar, they are likely from the same exciting source.

The shock that produced this emission must be travelling *considerably in excess of* 80 km/s (Hollenbach & McKee, 1989) in order to ionize neon. The spectra more closely resemble that of a supernova remnant, although there are several differences – the lack of certain lines (e.g. [P II] 32.5 μm) and the lack of detection of [Ne III] at 36 μm (Neufeld et al., 2007), although the latter is probably too faint to be detected in this case. The ratio of [S III] 18.7/33.4 μm varies widely across the flow, but is generally between 1.5-3, suggesting a temperature well in excess of 2×10^4 K and a substantially higher electron density of 10^3, similar to that found in Seyfert galaxies (Alexander et al., 1999). However as noted in the PCA analysis, the [S III] ratio may be indicative of something other than the higher temperature shocked gas, but instead of a density gradient to the northeast, related to illumination from objects like HW2 in Cep A East.

Additionally, the region around W1-W2-W3 features a rising continuum at longer IRS wavelengths, which might suggest the infrared excess of an embedded protostar, were it not for the extended nature of the excess emission, which is found throughout the high excitation flow.

If the very large proper motion included a significant component along our line of sight, it might have been detected, as we can resolve 500 km/s velocities with high resolution; no such shift is noted, consistent with past observations.

4.5   Conclusions

Do outflows from young stellar objects significantly influence their environment? What effects do they exert on the surrounding medium? Do they compress it into filamentary structures, or fragment the medium?

We have observed an extremely powerful shock in the context of Herbig-Haro flows; it appears to fall in between HH 54/ HH7-11, and supernova remnant IC 443 in strength. If shocks this strongly dissociative are common in molecular clouds, then we can expect the cloud chemistry to be altered significantly. The extended

emission of very high excitation lines suggests that the ambient medium is exposed to temperatures of $\sim$ 100,000 K, indicating powerful UV irradiation and mixing; along with the detection of gas-phase water vapor, we may see extended maser emission. Furthermore, the stark morphological and chemical differences suggest that the HH 168 flow has a different origin than the flow above. We suggest, as did Raines (2000) and others, that the east-west flow origin is HW2, while the strong peak of emission at W2 indicates the hidden presence of a protostar at this position driving the HH 168 flow. If the flow instead originates from HW3c, we might expect to see even more powerful emission knots in high excitation mid-IR lines or in x-rays to the southeast of W2, semi-periodically spaced; furthermore this would seemingly be visible from the ground in [Fe II] 1.644 μm.

We have grouped together the largest collection of fine structure and rotational emission lines for a Herbig-Haro flow to date, including the first detections of [Ar III], [O IV], and possibly [Ne V], as well as gas-phase water vapor emission from an extended galactic source other than a supernova remnant. Spectral mapping has allowed us to determine which lines are spatially coincident and clearly show distinctions between [S III] 18.7 and 33.4 μm, and the lines with excitation energies above 13.6 eV (the energy required to ionize atomic hydrogen) trail the lines with lower excitation by several arcseconds, clearly resolving the working surface where the flow meets the ambient medium, allowing us to calculate in detail the shock dynamics.

We have noted that the region surrounding W2 is very hot, high density, and that this emission is extended a considerable distance to the northwest, roughly along the line of the HH 168 flow. This region marks a boundary between the irradiated gas to the northeast of the flow, and the cool cloud continuum to the southwest. The flow lies approximately but not precisely along a line tracing back to the protostar HW3c, to the southeast. Furthermore the [Fe II] emission knots are observed to be moving in excess of 800 km/s to the northwest (Raines et al., 2000). This suggests one of two possibilities:

First, that HW3c is the driving source of the flow, and these are knots of emission along the path. If this is true, then we must explain why the flow is not even stronger to the southeast, closer to HW3c. This could be due to increased extinction in that direction, or it is possible that the gas in the region of W2 was already heavily clumped and the shock is merely illuminating this fact.

Furthermore, HW3c is substantially less massive than HW2, which appears to be driving the east-west flow; if the outflow rate is directly related to the infall rate, and the infall rate is suggestive of the final mass of the protostar, then we might expect HW2 to drive a more energetic outflow than HW3c, which is clearly not seen. Finally, we do not observe a flow in the opposite direction emanating from HW3c, which suggests that either extinction and an unfavorable orientation veil that side of the flow from our view, or that it is quite a bit weaker than the HH 168 flow.

Second, we might conclude that the driving source is a heavily embedded protostar behind the dense gas at the position of W2. If we conclude that the W2 source is driving a jet to the northwest, and that all of the high excitation emission along the line is due to this jet, we must explain why the [Fe II] knots are traveling so quickly in the same direction as the flow.

A third possibility is that we are viewing an overlay of several flows – we already can see that the flow from HW2 and HH 168 are starkly different from each other in terms of chemistry, so it is quite possible that another superposition is occurring over HH 168.

This giant collection of diagnostics will be released in a series of papers: one focusing on the H_2 emission, one on the fine structure data, and one on potential water and HD detections. Furthermore Herschel-PACS will provide high spectral, but lower spatial resolution spectroscopy of the primary cooling line, [O I] 63 μm. We have used [Si II] and [Fe II] as proxies for [O I], but the derived fluxes predict different values for the flux of [O I], the mass flow rate may be better determined following direct observation of this line.

5   Summary and Conclusions

In this thesis I have highlighted some of the newest results in star formation and the kinematics of shocks that directly follow from the IRS_Disks and Outflows *Spitzer* programs. In Chapter 1, I reviewed the understanding of star formation and development prior to the launch of *Spitzer* and in Chapter 2 I discussed the diagnostics Spitzer-IRS was well-suited to detect. In Chapter 3, I presented new evidence that accretion is episodic and violent, suggesting that in the high states accretion may drive outflows powerful enough to blow out the circumstellar envelope of even low mass young stars. In Chapter 4, I traced and analyzed Spitzer-IRS maps of the jets and outflows from high mass stars in the Cepheus A complex to determine whether they were sufficiently powerful to disperse their natal clouds.

GGD 37 is a exemplary region for the study of YSO outflows that originate for intermediate or high-mass stars. The HH 168 flow is a paradigm of the interaction of outflows with the surrounding ambient medium for several reasons: first, it is one of the closer regions threaded with shocks; second, very low extinction toward it is indicated; third, the number and variable strength of the resolvable shocks within its confines. The Cepheus A region harbors molecular outflows, dense cores, compact radio emission sources, water masers, compact hard x-ray sources, potentially extended soft x-ray sources, circumstellar disks, precessing high mass protostars, and shocked molecular, atomic, and ionized gas.

The most important results from the outflow study are as follows:

- We present Spitzer-IRS 5.3-36 μm datacubes taken in spectral mapping mode of a 2' x 2' region of GGD 37, produced using software I developed by

modifying the SMART data reduction package, as well as post-processing routines.

- We confirm the result from Raines (2000) that the upper half of the GGD 37 region is distinct in terms of temperature and density from the lower HH 168 flow, and concur while that the driving source of the upper flow may be the Cep A East protostar HW2, the HH 168 flow is likely driven by another source. We confirm the spatial separation between the ionized gas in [Fe II] and the molecular hydrogen in the HH 168 flow; in addition we appear to resolve the shocked boundary by observing a further spatial separation between the higher excitation and the lower excitation ionized gas in the flow.

- We detect gas-phase water emission from the region around the radio source W2, and suggest that this region may contain the protostar that is driving the HH 168 flow, decreasing the potential length of the flow by over 50%.

- We present the first detection of [Ar III], [O IV], and [Ne V] fine structure lines, the highest excitation energy lines ever seen in the vicinity of a Herbig-Haro flow. Considering this data along with 0.2 keV X-ray maps of the flow, we suggest that HH 168 is the hottest HH object detected so far.

- We note the strong detections of higher ionization states [S III], [O IV], [Ne III], and [Fe III], which may impact physical models utilizing primarily lower ionization state optical/near-IR lines (e.g. Hartigan & Morse, 2007).

- We derive a strong statistical correlation between [S I] and H_2 S(1), indicating that [S I] is a strong diagnostic tool for determining the electron number density of low temperature material. The ratio of HD R(3)/HD R(4) is a complementary measure for the density of hydrogen at temperatures too low to excite the rotational modes of H_2. The lack of a clear HD R(4) detection prevents us from calculating the density of HD for GGD 37, although this line is detected in several other flows in our Spitzer-IRS outflow mapping sample.

- We measure and map the molecular hydrogen column density, temperature, ortho-to-para ratio, and extinction of the region, as well as the number

density of H_2, and the electron number density in the moderate temperature regime ($\sim$ 10000 K) using five lines of [Fe II], and the high temperature regime ($\sim$ 15000 K) using two lines of [S III].

- We determine the kinematics of the HH 168 flow using both the cooling in molecular hydrogen, and in [O I], using the five mid-IR lines of [Fe II] as a proxy, and determine that the energy of the HH 168 flow is comparable to or slightly less than the estimated binding energy of the GGD 37 molecular cloud. We suggest that the silicon abundance may be depleted compared to the iron abundance in this region.

Negative feedback in molecular clouds *must play an important role in star formation*; the derived star formation efficiency in molecular clouds in our galaxy and others is on the order of 1% (e.g. Evans et al., 2009). That is to say that the observed average star formation timescale is $\sim$ two orders of magnitude longer than the free-fall time from gravitational collapse (e.g. McKee & Ostriker, 2007). There must therefore be mechanisms that hinder the process of star formation to a large degree, supporting the cloud cores against final collapse at some size scale.

Star formation does not occur in isolation. Protostars and their environment engage in a continual feedback loop that may drive turbulence in the cloud (Carroll et al., 2008). From this dataset we have the ability to measure directly the impact of an outflow upon the surrounding medium. What is the propensity of a flow like GGD 37 to disrupt a cloud core? The initial properties of the medium have a strong impact upon the final composition of the protoplanetary disk, and the planets that form in it. High mass stars may drive or disrupt the formation of smaller systems either through supernova or through their massive extended jets, sweeping massive cavities and causing density clumps that may seed star formation on a smaller scale. Intermediate protostars can still influence their environment by driving powerful outflows like HH 168. Even the far more numerous low mass protostars can drive considerable outflows following cataclysmic events that temporarily drive high accretion rates powerful enough to dissipate their protostellar envelopes.

In any case this multiplicity of flows suggests that shocks and jets thread molecular clouds quite commonly, and the details of their interactions may prove important in determining the final filamentary structure of the cloud itself, and

select the areas of protostellar formation. Furthermore there may be two epochs of star formation; one in which the initial protostars drive jets through the cloud, and one in which these jets help determine where the second generation forms.

The simplest way to resolve this dilemma is to measure very accurately the proper motions of the gas using an instrument like WFPC3 on the Hubble Space Telescope, which can achieve a velocity resolution down to 10 km/s. to combine with earlier observations by Hartigan et al. (2000) from WFPC2 in 1988; it would be possible to determine in detail the vector of the motions away from the driving source of the flow, which would point either toward HW3c or W2. There are a number of questions that we cannot answer without higher resolution proper motion data and testing through numerical simulations. Where does the clumpiness of Herbig Haro flows come from? Is it inhomogeneities in the ambient medium pre-shock? Or is it periodic spikes in the accretion rate? Or turbulent instabilities that form within the flow itself? From the extended nature of even the highest ionization emission lines in our sample, we suggest that this high outflow rate is sustained in the veiled intermediate mass protostar that is driving the HH 168 flow.

Bibliography

Adams, F. C., Lada, C. J., & Shu, F. H. 1987, ApJ, 312, 788

Adams, F. C., & Shu, F. H. 1986, ApJ, 308, 836

Adams, F. C., Shu, F. H., & Lada, C. J. 1988, ApJ, 326, 865

Alexander, T., Sturm, E., Lutz, D., Sternberg, A., Netzer, H., & Genzel, R. 1999, ApJ, 512, 204

Allard, F., Hauschildt, P. H., & Schweitzer, A. 2000, ApJ, 539, 366

Allen, M. G., Groves, B. A., Dopita, M. A., Sutherland, R. S., & Kewley, L. J. 2008, ApJS, 178, 20

Bachiller, R. 1996, ARA&A, 34, 111

Bally, J., Feigelson, E., & Reipurth, B. 2003, ApJ, 584, 843

Bally, J., & Lane, A. P. 1991, in Astronomical Society of the Pacific Conference Series, Vol. 14, Astronomical Society of the Pacific Conference Series, ed. R. Elston, 273–278

Begemann, B., Dorschner, J., Henning, T., Mutschke, H., & Thamm, E. 1994, ApJ, 423, L71

Bell, K. R., Cassen, P. M., Klahr, H. H., & Henning, T. 1997, ApJ, 486, 372

Bell, K. R., & Lin, D. N. C. 1994, ApJ, 427, 987

Bell, K. R., Lin, D. N. C., Hartmann, L. W., & Kenyon, S. J. 1995, ApJ, 444, 376

Boogert, A. C. A., Pontoppidan, K. M., Knez, C., Lahuis, F., Kessler-Silacci, J., van Dishoeck, E. F., Blake, G. A., Augereau, J.-C., Bisschop, S. E., Bottinelli, S., Brooke, T. Y., Brown, J., Crapsi, A., Evans, II, N. J., Fraser, H. J., Geers, V., Huard, T. L., Jørgensen, J. K., Öberg, K. I., Allen, L. E., Harvey, P. M., Koerner, D. W., Mundy, L. G., Padgett, D. L., Sargent, A. I., & Stapelfeldt, K. R. 2008, ApJ, 678, 985

Calvet, N. 1998, in American Institute of Physics Conference Series, Vol. 431, American Institute of Physics Conference Series, ed. S. S. Holt & T. R. Kallman, 495–+

Calvet, N., Hartmann, L., & Kenyon, S. J. 1991, ApJ, 383, 752

Calvet, N., Magris, G. C., Patino, A., & D'Alessio, P. 1992, Revista Mexicana de Astronomia y Astrofisica, 24, 27

Calvet, N., Muzerolle, J., Briceño, C., Hernández, J., Hartmann, L., Saucedo, J. L., & Gordon, K. D. 2004, AJ, 128, 1294

Carroll, J. J., Frank, A., Blackman, E. G., Cunningham, A. J., & Quillen, A. C. 2008, ArXiv e-prints

Chiang, E. I., & Goldreich, P. 1997, ApJ, 490, 368

Chiar, J. E., Ennico, K., Pendleton, Y. J., Boogert, A. C. A., Greene, T., Knez, C., Lada, C., Roellig, T., Tielens, A. G. G. M., Werner, M., & Whittet, D. C. B. 2007, ApJ, 666, L73

Clarke, C., Lodato, G., Melnikov, S. Y., & Ibrahimov, M. A. 2005, MNRAS, 361, 942

Cohen, M., & Kuhi, L. V. 1979, ApJS, 41, 743

Cohen, M., Megeath, S. T., Hammersley, P. L., Martín-Luis, F., & Stauffer, J. 2003, AJ, 125, 2645

Cohen, M., & Woolf, N. J. 1971, ApJ, 169, 543

Comerón, F., Neuhäuser, R., & Kaas, A. A. 2000, A&A, 359, 269

Comeron, F., Rieke, G. H., Claes, P., Torra, J., & Laureijs, R. J. 1998, A&A, 335, 522

Croswell, K., Hartmann, L., & Avrett, E. H. 1987, ApJ, 312, 227

Cunningham, N. J. 2006, PhD thesis, AA(UNIVERSITY OF COLORADO AT BOULDER)

Curiel, S., Trinidad, M. A., Cantó, J., Rodríguez, L. F., Torrelles, J. M., Ho, P. T. P., Patel, N. A., Greenhill, L., Gómez, J. F., Garay, G., Hernández, L., Contreras, M. E., & Anglada, G. 2002, ApJ, 564, L35

D'Alessio, P. 1996, PhD thesis, AA(Instituto de Astronomía, UNAM, Apartado Postal 70-264, Ciudad Univesitaria, CP. 04510, México 20, D. F., México EMAIL: dalessio@astroscu.unam.mx)

D'Alessio, P., Calvet, N., & Hartmann, L. 1997, ApJ, 474, 397

D'Alessio, P., Calvet, N., Hartmann, L., Lizano, S., & Cantó, J. 1999, ApJ, 527, 893

Demyk, K., Dartois, E., Wiesemeyer, H., Jones, A., D'Hendecourt, L., Jourdain de Muizon, M., & Heras, A. M. 2000, in ESA Special Publication, Vol. 456, ISO Beyond the Peaks: The 2nd ISO Workshop on Analytical Spectroscopy, ed. A. Salama, M. F. Kessler, K. Leech, & B. Schulz, 183–+

Di Francesco, J., Myers, P. C., Wilner, D. J., Ohashi, N., & Mardones, D. 2001, ApJ, 562, 770

Draine, B. T. 1980, ApJ, 241, 1021

—. 2003, ARA&A, 41, 241

Draine, B. T., & Lee, H. M. 1984, ApJ, 285, 89

Draine, B. T., & McKee, C. F. 1993, ARA&A, 31, 373

Drew, J. E., Proga, D., & Stone, J. M. 1998, MNRAS, 296, L6+

Evans, N. J., Dunham, M. M., Jørgensen, J. K., Enoch, M. L., Merín, B., van Dishoeck, E. F., Alcalá, J. M., Myers, P. C., Stapelfeldt, K. R., Huard, T. L., Allen, L. E., Harvey, P. M., van Kempen, T., Blake, G. A., Koerner, D. W., Mundy, L. G., Padgett, D. L., & Sargent, A. I. 2009, ApJS, 181, 321

Favata, F., Fridlund, C. V. M., Micela, G., Sciortino, S., & Kaas, A. A. 2002, A&A, 386, 204

Fazio, G. G., Hora, J. L., Allen, L. E., Ashby, M. L. N., Barmby, P., Deutsch, L. K., Huang, J.-S., Kleiner, S., Marengo, M., Megeath, S. T., Melnick, G. J., Pahre, M. A., Patten, B. M., Polizotti, J., Smith, H. A., Taylor, R. S., Wang, Z., Willner, S. P., Hoffmann, W. F., Pipher, J. L., Forrest, W. J., McMurty, C. W., McCreight, C. R., McKelvey, M. E., McMurray, R. E., Koch, D. G., Moseley, S. H., Arendt, R. G., Mentzell, J. E., Marx, C. T., Losch, P., Mayman, P., Eichhorn, W., Krebs, D., Jhabvala, M., Gezari, D. Y., Fixsen, D. J., Flores, J., Shakoorzadeh, K., Jungo, R., Hakun, C., Workman, L., Karpati, G., Kichak, R., Whitley, R., Mann, S., Tollestrup, E. V., Eisenhardt, P., Stern, D., Gorjian, V., Bhattacharya, B., Carey, S., Nelson, B. O., Glaccum, W. J., Lacy, M., Lowrance, P. J., Laine, S., Reach, W. T., Stauffer, J. A., Surace, J. A., Wilson, G., Wright, E. L., Hoffman, A., Domingo, G., & Cohen, M. 2004, ApJS, 154, 10

Flaherty, K. M., Pipher, J. L., Megeath, S. T., Winston, E. M., Gutermuth, R. A., Muzerolle, J., Allen, L. E., & Fazio, G. G. 2007, ApJ, 663, 1069

Furlan, E. 2006, PhD thesis, Cornell University, United States – New York

Galavis, M. E., Mendoza, C., & Zeippen, C. J. 1995, A&AS, 111, 347

Garay, G., Ramirez, S., Rodriguez, L. F., Curiel, S., & Torrelles, J. M. 1996, ApJ, 459, 193

Glassgold, A. E., Najita, J. R., & Igea, J. 2007, ApJ, 656, 515

Goodrich, R. W. 1987, PASP, 99, 116

Graham, J. A., & Frogel, J. A. 1985, ApJ, 289, 331

Grasdalen, G. L. 1973, ApJ, 182, 781

Greenberg, L. T., Dyal, P., & Geballe, T. R. 1977, ApJ, 213, L71

Groves, B., Nefs, B., & Brandl, B. 2008, MNRAS, 391, L113

Güdel, M., Briggs, K. R., Arzner, K., Audard, M., Bouvier, J., Feigelson, E. D., Franciosini, E., Glauser, A., Grosso, N., Micela, G., Monin, J.-L., Montmerle, T., Padgett, D. L., Palla, F., Pillitteri, I., Rebull, L., Scelsi, L., Silva, B., Skinner, S. L., Stelzer, B., & Telleschi, A. 2007, A&A, 468, 353

Gutermuth, R. A., Myers, P. C., Megeath, S. T., Allen, L. E., Pipher, J. L., Muzerolle, J., Porras, A., Winston, E., & Fazio, G. 2008, ApJ, 674, 336

Gyulbudaghian, A. L., Glushkov, Y. I., & Denisyuk, E. K. 1978, ApJ, 224, L137+

Hartigan, P., & Lada, C. J. 1985, ApJS, 59, 383

Hartigan, P., Lada, C. J., Tapia, S., & Stocke, J. 1986, AJ, 92, 1155

Hartigan, P., & Morse, J. 2007, ApJ, 660, 426

Hartigan, P., Morse, J., & Bally, J. 2000, AJ, 120, 1436

Hartmann, L. 1998, Accretion Processes in Star Formation (Accretion processes in star formation / Lee Hartmann. Cambridge, UK ; New York : Cambridge University Press, 1998. (Cambridge astrophysics series ; 32) ISBN 0521435072.)

Hartmann, L., Boss, A., Calvet, N., & Whitney, B. 1994, ApJ, 430, L49

Hartmann, L., Calvet, N., & Boss, A. 1996, ApJ, 464, 387

Hartmann, L., & Kenyon, S. J. 1985, ApJ, 299, 462

—. 1987a, ApJ, 312, 243

—. 1987b, ApJ, 322, 393

—. 1996, ARA&A, 34, 207

Herbig, G. H. 1952, JRASC, 46, 222

—. 1977, ApJ, 217, 693

Higdon, S. J. U., Devost, D., Higdon, J. L., Brandl, B. R., Houck, J. R., Hall, P., Barry, D., Charmandaris, V., Smith, J. D. T., Sloan, G. C., & Green, J. 2004, PASP, 116, 975

Hiriart, D., Salas, L., & Cruz-González, I. 2004, AJ, 128, 2917

Hollenbach, D., Johnstone, D., Lizano, S., & Shu, F. 1994, ApJ, 428, 654

Hollenbach, D., & McKee, C. F. 1989, ApJ, 342, 306

Houck, J. R., Roellig, T. L., van Cleve, J., Forrest, W. J., Herter, T., Lawrence, C. R., Matthews, K., Reitsema, H. J., Soifer, B. T., Watson, D. M., Weedman, D., Huisjen, M., Troeltzsch, J., Barry, D. J., Bernard-Salas, J., Blacken, C. E., Brandl, B. R., Charmandaris, V., Devost, D., Gull, G. E., Hall, P., Henderson, C. P., Higdon, S. J. U., Pirger, B. E., Schoenwald, J., Sloan, G. C., Uchida, K. I., Appleton, P. N., Armus, L., Burgdorf, M. J., Fajardo-Acosta, S. B., Grillmair, C. J., Ingalls, J. G., Morris, P. W., & Teplitz, H. I. 2004, ApJS, 154, 18

Hughes, V. A. 1989, AJ, 97, 1114

Hughes, V. A., & Wouterloot, J. G. A. 1982, A&A, 106, 171

Ibrahimov, M. A. 1996, Information Bulletin on Variable Stars, 4285, 1

—. 1999, Information Bulletin on Variable Stars, 4691, 1

Joy, A. H. 1945, ApJ, 102, 168

—. 1949, ApJ, 110, 424

Kenyon, S. J., Calvet, N., & Hartmann, L. 1993, ApJ, 414, 676

Kenyon, S. J., & Hartmann, L. 1987, ApJ, 323, 714

—. 1995, ApJS, 101, 117

Kenyon, S. J., Hartmann, L., & Hewett, R. 1988, ApJ, 325, 231

Kenyon, S. J., & Hartmann, L. W. 1991, ApJ, 383, 664

Kurosawa, R., Harries, T. J., & Symington, N. H. 2006, MNRAS, 370, 580

Lada, C. J. 1985, ARA&A, 23, 267

Larson, R. B. 1969, MNRAS, 145, 271

—. 1972, MNRAS, 157, 121

Lin, D. N. C., & Papaloizou, J. 1985, in Protostars and Planets II, ed. D. C. Black & M. S. Matthews, 981–1072

Luhman, K. L. 1999, ApJ, 525, 466

Malbet, F., Lachaume, R., Berger, J.-P., Colavita, M. M., di Folco, E., Eisner, J. A., Lane, B. F., Millan-Gabet, R., Ségransan, D., & Traub, W. A. 2005, A&A, 437, 627

Maret, S., Caux, E., & Ceccarelli, C. 2002, Ap&SS, 281, 139

Mathis, J. S. 1990, ARA&A, 28, 37

Matzner, C. D., & McKee, C. F. 1999, ApJ, 526, L109

McClure, M. K. 2008, ArXiv e-prints

McDonald, J. M., & Clarke, C. J. 1993, MNRAS, 262, 800

McKee, C. F., & Ostriker, E. C. 2007, ARA&A, 45, 565

Megeath, S. T., Allen, L. E., Gutermuth, R. A., Pipher, J. L., Myers, P. C., Calvet, N., Hartmann, L., Muzerolle, J., & Fazio, G. G. 2004, ApJS, 154, 367

Melnick, G. J., Tolls, V., Neufeld, D. A., Yuan, Y., Sonnentrucker, P., Watson, D. M., Bergin, E. A., & Kaufman, M. J. 2008, ApJ, 683, 876

Millan-Gabet, R., Monnier, J. D., Akeson, R. L., Hartmann, L., Berger, J.-P., Tannirkulam, A., Melnikov, S., Billmeier, R., Calvet, N., D'Alessio, P., Hillenbrand, L. A., Kuchner, M., Traub, W. A., Tuthill, P. G., Beichman, C., Boden, A., Booth, A., Colavita, M., Creech-Eakman, M., Gathright, J., Hrynevych, M., Koresko, C., Le Mignant, D., Ligon, R., Mennesson, B., Neyman, C., Sargent, A., Shao, M., Swain, M., Thompson, R., Unwin, S., van Belle, G., Vasisht, G., & Wizinowich, P. 2006, ApJ, 641, 547

Miller, G. E., & Scalo, J. M. 1979, ApJS, 41, 513

Mould, J. R., Hall, D. N. B., Ridgway, S. T., Hintzen, P., & Aaronson, M. 1978, ApJ, 222, L123

Muzerolle, J., Calvet, N., Hartmann, L., & D'Alessio, P. 2003, ApJ, 597, L149

Neufeld, D. A., Green, J. D., Hollenbach, D. J., Sonnentrucker, P., Melnick, G. J., Bergin, E. A., Snell, R. L., Forrest, W. J., Watson, D. M., & Kaufman, M. J. 2006a, ApJ, 647, L33

Neufeld, D. A., Hollenbach, D. J., Kaufman, M. J., Snell, R. L., Melnick, G. J., Bergin, E. A., & Sonnentrucker, P. 2007, ApJ, 664, 890

Neufeld, D. A., Melnick, G. J., Sonnentrucker, P., Bergin, E. A., Green, J. D., Kim, K. H., Watson, D. M., Forrest, W. J., & Pipher, J. L. 2006b, ApJ, 649, 816

Osorio, M., D'Alessio, P., Muzerolle, J., Calvet, N., & Hartmann, L. 2003, ApJ, 586, 1148

Paczynski, B. 1976, in IAU Symposium, Vol. 73, Structure and Evolution of Close Binary Systems, ed. P. Eggleton, S. Mitton, & J. Whelan, 75–+

Peeters, E., Hony, S., Van Kerckhoven, C., Tielens, A. G. G. M., Allamandola, L. J., Hudgins, D. M., & Bauschlicher, C. W. 2002, A&A, 390, 1089

Pollack, J. B., Hollenbach, D., Beckwith, S., Simonelli, D. P., Roush, T., & Fong, W. 1994, ApJ, 421, 615

Pontoppidan, K. M., Boogert, A. C. A., Fraser, H. J., van Dishoeck, E. F., Blake, G. A., Lahuis, F., Öberg, K. I., Evans, II, N. J., & Salyk, C. 2008, ApJ, 678, 1005

Pottasch, S. R., Beintema, D. A., Raimond, E., Baud, B., van Duinen, R., Habing, H. J., Houck, J. R., de Jong, T., Jennings, R. E., Olnon, F. M., & Wesselius, P. R. 1984, ApJ, 278, L33

Pradhan, A. K., & Zhang, H. L. 1993, ApJ, 409, L77

Pravdo, S. H., & Tsuboi, Y. 2005, ApJ, 626, 272

Quanz, S. P., Henning, T., Bouwman, J., van Boekel, R., Juhász, A., Linz, H., Pontoppidan, K. M., & Lahuis, F. 2007, ApJ, 668, 359

Quillen, A. C., Thorndike, S. L., Cunningham, A., Frank, A., Gutermuth, R. A., Blackman, E. G., Pipher, J. L., & Ridge, N. 2005, ApJ, 632, 941

Raines, S. N. 2000, PhD thesis, AA(THE UNIVERSITY OF ROCHESTER)

Raines, S. N., Watson, D. M., Pipher, J. L., Forrest, W. J., Greenhouse, M. A., Satyapal, S., Woodward, C. E., Smith, H. A., Fischer, J., Goetz, J. A., & Frank, A. 2000, ApJ, 528, L115

Reipurth, B., Hartmann, L., Kenyon, S. J., Smette, A., & Bouchet, P. 2002, AJ, 124, 2194

Reipurth, B., & Raga, A. C. 1999, in NATO ASIC Proc. 540: The Origin of Stars and Planetary Systems, ed. C. J. Lada & N. D. Kylafis, 267–+

Rieke, G., Lee, T., & Coyne, G. 1972, PASP, 84, 37

Rieke, G. H., Young, E. T., Engelbracht, C. W., Kelly, D. M., Low, F. J., Haller, E. E., Beeman, J. W., Gordon, K. D., Stansberry, J. A., Misselt, K. A., Cadien, J., Morrison, J. E., Rivlis, G., Latter, W. B., Noriega-Crespo, A., Padgett, D. L., Stapelfeldt, K. R., Hines, D. C., Egami, E., Muzerolle, J., Alonso-Herrero, A., Blaylock, M., Dole, H., Hinz, J. L., Le Floc'h, E., Papovich, C., Pérez-González, P. G., Smith, P. S., Su, K. Y. L., Bennett, L., Frayer, D. T., Henderson, D., Lu, N., Masci, F., Pesenson, M., Rebull, L., Rho, J., Keene, J., Stolovy, S., Wachter, S., Wheaton, W., Werner, M. W., & Richards, P. L. 2004, ApJS, 154, 25

Rodríguez, L. F., Torrelles, J. M., Raga, A. C., Cantó, J., Curiel, S., & Garay, G. 2005, Revista Mexicana de Astronomia y Astrofisica, 41, 435

Roellig, T. L., Van Cleve, J. E., Sloan, G. C., Wilson, J. C., Saumon, D., Leggett, S. K., Marley, M. S., Cushing, M. C., Kirkpatrick, J. D., Mainzer, A. K., & Houck, J. R. 2004, ApJS, 154, 418

Rownd, B. K., & Young, J. S. 1999, AJ, 118, 670

Russell, H. N. 1913, The Observatory, 36, 324

Rydgren, A. E., Strom, S. E., & Strom, K. M. 1976, ApJS, 30, 307

Sargent, B., Forrest, W. J., D'Alessio, P., Li, A., Najita, J., Watson, D. M., Calvet, N., Furlan, E., Green, J. D., Kim, K. H., Sloan, G. C., Chen, C. H., Hartmann, L., & Houck, J. R. 2006, ApJ, 645, 395

Savage, B. D., & Mathis, J. S. 1979, ARA&A, 17, 73

Schutte, W. A., van der Hucht, K. A., Whittet, D. C. B., Boogert, A. C. A., Tielens, A. G. G. M., Morris, P. W., Greenberg, J. M., Williams, P. M., van Dishoeck, E. F., Chiar, J. E., & de Graauw, T. 1998, A&A, 337, 261

Shang, H., Li, Z.-Y., & Hirano, N. 2007, in Protostars and Planets V, ed. B. Reipurth, D. Jewitt, & K. Keil, 261–276

Shu, F. H. 1977, ApJ, 214, 488

Shu, F. H., Najita, J., Ostriker, E. C., & Shang, H. 1995, ApJ, 455, L155+

Shu, F. H., Najita, J. R., Shang, H., & Li, Z.-Y. 2000, Protostars and Planets IV, 789

Simon, T. 1975, PASP, 87, 317

Simon, T., Morrison, N. D., Wolff, S. C., & Morrison, D. 1972, PASP, 84, 644

Sloan, G. C., Keller, L. D., Forrest, W. J., Leibensperger, E., Sargent, B., Li, A., Najita, J., Watson, D. M., Brandl, B. R., Chen, C. H., Green, J. D., Markwick-Kemper, F., Herter, T. L., D'Alessio, P., Morris, P. W., Barry, D. J., Hall, P., Myers, P. C., & Houck, J. R. 2005, ApJ, 632, 956

Smak, J. 1964, ApJ, 139, 1095

Soker, N., & Regev, O. 2003, A&A, 406, 603

Sonnentrucker, P., González-Alfonso, E., Neufeld, D. A., Bergin, E. A., Melnick, G. J., Forrest, W. J., Pipher, J. L., & Watson, D. M. 2006, ApJ, 650, L71

Terebey, S., Shu, F. H., & Cassen, P. 1984, ApJ, 286, 529

Torbett, M. V. 1984, ApJ, 278, 318

Turner, N. J. J., Bodenheimer, P., & Bell, K. R. 1997, ApJ, 480, 754

Varsavsky, C. M. 1960, ApJ, 132, 354

Warren, S. G. 1984, Appl. Opt., 23, 1206

Watson, D. M. 1985, Phys. Scr, 11, 33

Watson, D. M., Bohac, C. J., Hull, C., Forrest, W. J., Furlan, E., Najita, J., Calvet, N., D'Alessio, P., Hartmann, L., Sargent, B., Green, J. D., Kim, K. H., & Houck, J. R. 2007, Nature, 448, 1026

Watson, D. M., Kemper, F., Calvet, N., Keller, L. D., Furlan, E., Hartmann, L., Forrest, W. J., Chen, C. H., Uchida, K. I., Green, J. D., Sargent, B., Sloan, G. C., Herter, T. L., Brandl, B. R., Houck, J. R., Najita, J., D'Alessio, P., Myers, P. C., Barry, D. J., Hall, P., & Morris, P. W. 2004, ApJS, 154, 391

Werner, M. W., Roellig, T. L., Low, F. J., Rieke, G. H., Rieke, M., Hoffmann, W. F., Young, E., Houck, J. R., Brandl, B., Fazio, G. G., Hora, J. L., Gehrz, R. D., Helou, G., Soifer, B. T., Stauffer, J., Keene, J., Eisenhardt, P., Gallagher, D., Gautier, T. N., Irace, W., Lawrence, C. R., Simmons, L., Van Cleve, J. E., Jura, M., Wright, E. L., & Cruikshank, D. P. 2004, ApJS, 154, 1

Wiscombe, W. J. 1979

Zasowski, G., Kemper, F., Watson, D. M., Furlan, E., Bohac, C. J., Hull, C., & Green, J. D. 2009, ApJ, 694, 459

Zhu, Z., Hartmann, L., Calvet, N., Hernandez, J., Tannirkulam, A.-K., & D'Alessio, P. 2008, ApJ, 684, 1281

A   Glossary of Terms

A.1   Units

1 astronomical unit (AU) = average distance between Earth and the Sun = 1.5 × 10^{13} cm

1 solar mass ($M_\odot$) = 2.0 × 10^{33} grams

1 solar luminosity ($L_\odot$) = 3.3 × 10^{33} erg/s

1 parsec (pc) = 3.26 light years (ly) = 3.1 × 10^{18} cm

1 jansky (Jy) = 10^{-23} erg/s/cm^2/Hz (flux density)

magnitude (mag) = a dimensionless measurement of the apparent brightness of a source. The magnitude scale is logarithmic (base 2.5) in flux, ie. a change of 5 magnitudes corresponds to a factor of 100 in luminosity. The system is calibrated with respect to measurements of the prototypical A0 star, Vega (α Lyrae).

A.2   Jargon

A.2.1   Wavelength Regimes

SED = Spectral Energy Distribution, flux density plotted as a function of wavelength

UV = ultraviolet ($\lambda \lesssim 0.3$ μm)

IR = infrared ($\lambda \gtrsim 0.7$ μm)

near-IR = near-infrared, from the longest optical wavelengths to a few μm. The transmission through the atmosphere is considerable at these wavelengths, observed from the ground.

mid-IR = mid-infrared, wavelengths from a few microns to $\sim 50~\mu$m. There are very few atmospheric transmission windows at these wavelengths and space-based observing is more important.

far-IR = far-infrared, wavelengths from ~ 50 to a few hundred μm; this regime will soon be covered by the Herschel Space Observatory

sub-mm = sub-millimeter wavelengths from ~ 0.2 to 1 mm, where microwave begins

J,H,K$_s$ – atmospheric transmission windows in the near-IR

J $= 1.25~\mu$m

H $= 1.65~\mu$m

K$_s = 2.2~\mu$m

Hα = H-Alpha = Balmer Alpha $= 0.656~\mu$m transition n $= 3 \rightarrow 2$

A.2.2 Observatory-Related Acronyms

SST – Spitzer Space Telescope, which utilizes three instruments:

IRAC = InfraRed Array Camera

IRS = InfraRed Spectrograph

MIPS = Multiband Imaging Photometer for Spitzer

IRS contains four separate modules, named by wavelength and spectral resolution:

SL = Short-Low

LL = Long-Low

SH = Short-High

LH = Long-High

SSC = Spitzer Science Center

AOR / AORID = Numbering system for observation logs of *Spitzer* data. each AOR represents a set of observations made in a single observing mode, but may include multiple pointings (indexed by ExpID), and multiple exposures (indexed by DCE) per single pointing.

BIB = Blocked Impurity-Band detector

SMART = Spectroscopic Modeling, Analysis, and Reduction Tool

SLCF = Slit Loss Correction Function

BCD = Basic Calibrated Data

"droop" data = An intermediate data product; BCD data without the corrections for flatfielding and stray light from the dispersion dimension of the array

IRAS = InfraRed Astronomical Satellite

ISO = Infrared Space Observatory

2MASS = 2-Micron All-Sky Survey

A.2.3 Acronyms for Astrophysical Objects and Phenomena

PAH = Polycyclic Aromatic Hydrocarbons

HH = Herbig-Haro object

GGD = Gyulbudaghian, Glushkov, and Denisyuk; a catalogue of molecular clouds named after the authors

YSO = Young Stellar Object

YSO classification scheme: originally derived from the optical/near-IR SED

Class 0 = No significant emission from the source at $\lambda \sim 20$ μm; heavily embedded protostar plus circumstellar envelope emission

Class I = The circumstellar envelope is thinner and the slope of the SED (rising to longer wavelengths) is less steep than for Class 0 sources

FS = Flat Spectrum Sources = Those with considerable long wavelength excess but also substantial short wavelength excess so that the power spectrum appears "flat", ie. varying little in wavelength

Class II = No significant contribution to the SED from the circumstellar envelope; at optical/near-IR wavelengths the young star emerges to dominate the SED, while at mid-IR wavelengths the circumstellar accretion disk dominates

Class III = No significant contribution to the SED from the disk at wavelengths below ~ 20 μm; the emission is dominated by the central star, and the optically

thick accretion disk is no longer present, although there can be optically thin emission from dust. The gas has typically dissipated by this point

CTTS = Classical T Tauri Star (one containing an infrared excess); sometimes contrasted with WTTS (Weak-Line T Tauri Star) which lack strong H_α lines, usually interpreted as a lower accretion rate.

FU Ori object = named after the archetypal source, FU Orionis; these objects exhibit large flares at optical and infrared wavelengths that have an e-folding time of ~ 100 yr; they are thought to be the signature of large punctuated bursts of accretion onto a young star

ISM = InterStellar Medium, dust and gaseous material located outside of stellar systems and star forming regions within a galaxy

J-type = Jump-type shock (density and temperature change discontinuously at the shock boundary)

C-type = Continuous-type shock (density and temperature change continuously at the shock boundary)

A.2.4 Notation

PCA = Principal Component Analysis, a statistical technique for studying correlations in multi-dimensional datasets. The principal component is the axis of greatest variance in the dataset; in a 2-D case this would be the "line of best fit"

[] notation = indicates that a particular spectral line represents a forbidden atomic/ionic transition; that is, a transition that is nominally forbidden by the selection rules but has a certain probability of occurring spontaneously in a given time, at a much lower rate than collisional de-excitation. For example, [Si II] represents a forbidden transition of singly ionized silicon

R(J) notation – A series of lines in molecular spectroscopy that correspond to a unit change of +1 in the rotational quantum number J (where J represents the lower state)

S(J) notation – A series of lines that correspond to purely rotational modes in a molecule for transitions of $\Delta J = -2$